UNIVERSITY OF OKLAHOMA

GRADUATE COLLEGE

CORRELATION OF BIOTURBATED FACIES, CHEMOSTRATIGRAPHY, TOTAL ORGANIC CARBON, AND SEQUENCE STRATIGRAPHY IN THE WOODFORD SHALE OF SOUTH CENTRAL OKLAHOMA

A THESIS

SUBMITTED TO THE GRADUATE FACULTY

in partial fulfillment of the requirements for the

Degree of

MASTER OF SCIENCE

By

SABRINA MAYNARD
Norman, Oklahoma
2016

CORRELATION OF BIOTURBATED FACIES, CHEMOSTRATIGRAPHY, TOTAL ORGANIC CARBON, AND SEQUENCE STRATIGRAPHY IN THE WOODFORD SHALE OF SOUTH CENTRAL OKLAHOMA

A THESIS APPROVED FOR THE
CONOCOPHILLIPS SCHOOL OF GEOLOGY AND GEOPHYSICS

BY

_____
Dr. Roger Slatt, Chair

_____
Dr. Douglas Elmore

_____
Mr. Douglas Jordan

© Copyright by SABRINA MAYNARD 2016
All Rights Reserved.

For my parents Mark and Shirley

For my son, William

ACKNOWLEDGEMENTS

"Civilization exists by geological consent, subject to change without notice."
-Will Durant

I want to first thank my parents, Mark and Shirley Stevens, they have been my pillars of support through my whole life. Never have they waivered in fervent belief that I could accomplish anything that I wanted to. They have always allowed me to walk my own path and encouraged each and every challenge I have ever taken on.

I want to thank my Mom who gave up countless evenings to babysit when I decided to go back to school as the single mother of a three month old. She was always there, no matter how late my classes ran or how late I needed quiet time to study. My Dad who was my sounding board in times of frustration, sacrificed and cheered me on through this whole process.

I would also like to thank my husband, Taylor, who came into this process at the tail end and stepped up to take the household burdens off my shoulders even when all four of our young boys were at home. Who helped me stay positive through countless sleepless nights and never complained about doing more than his fair share to keep our home running smoothly. I cannot wait for the next chapter in our lives.

I also wish to thank the members of my committee. My committee chair, Dr. Roger Slatt, who took on a part-time graduate student, who worked full time and disappeared for weeks at a time for military training. Dr. Slatt was always there, willing to answer questions and expose me to as much information as I could get my hands on with never-ending support and guidance. I would like to thank Doug Jordan for his guidance in the world of core descriptions and for taking on the extra work load involved in guiding a student through research. Last but not least of my committee members, Dr.

Douglas Elmore for accepting to be on my committee and providing an always enthusiastic outlook to the world of academia.

I would like to also thank Mark Orgren, my very first boss at Chesapeake who encouraged and fought for me to go back to school. His passion of all things geological drove desire to know more and even from the start he encouraged that pursuit of knowledge beyond my job title; without him going to bat for me to take courses during working hours I do not know how I would have ever accomplished this dream of mine.

Finally, Cori Smith, for all of your support, advice, coffee breaks, and for being the one to go first; for understanding better than anyone the late nights, the stress, and the panic of trying to complete this process and work full time.

TABLE OF CONTENTS

ACKNOWLEDGEMENTS…….iv

LIST OF TABLES……..viii

LIST OF FIGURES……..ix

ABSTRACT……xii

1. INTRODUCTION…….1

1.1 OBJECTIVES……..3

1.2 GEOLOGICAL CONTEXT……4

1.2.1 Regional Geology…….4

1.2.2 Study Area……7

2. METHODS……8

2.1 DATA AVAILABLE…….…….…....9

2.2 X-RAY FLOURESCENCE…….…….…....9

2.3 X-RAY DIFFRACTION…….……..10

2.4 TOTAL ORGANIC CARBON.…….……10

3. RESULTS AND DISCUSSION……..…….…….....11

3.1 CORE DESCRIPTIONS…….…….....11

3.1.1 Lithofacies……..…….…….……11

3.1.2 Bioturbation……19

3.2 MINERALOGY AND TOTAL ORGANIC CARBON…….……..….20

3.3 SEQUENCE STRATIGRAPHY……..…….21

3.4 CHEMOSTRATIGRAPHY...……..…….....24

3.5 BOTTOM WATER CONDITIONS...…….…….....29

4. CORRELATIONS……...34

4.1 CHEMOSTRATIGRAPHY…….…….43

4.1.1 Core D……..……...43

4.1.2 Core E……..…...49

4.2 BOTTOM WATER CONDITIONS…….……...…..54

4.2.1 Core D……..……...……55

4.2.2 Core E……...……...…...58

5. CONCLUSION……61

REFERENCES……63

APPENDIX A: CORE A CORE DESCRIPTION……..68

APPENDIX B: CORE B CORE DESCRIPTION……81

APPENDIX C: CORE C CORE DESCRIPTION……90

APPENDIX D: CORE D CORE DESCRIPTION…….100

APPENDIX E: CORE D XRF CHART……...……..107

APPENDIX F: CORE E CORE DESCRIPTION……...……...108

APPENDIX G: CORE E XRF CHART……...……..119

LIST OF TABLES

Table 1. A list of the principal elements used for correlation and their primary stratigraphic proxy……...24

LIST OF FIGURES

Figure 1. Major Geological Provinces of Oklahoma……..…5

Figure 2. Stratigraphic relationship of the Woodford Shale with overlying Sycamore and underlying Hunton Group…….……..…6

Figure 3. Woodford Shale type log subdivided into three informal members……7

Figure 4. Location map of 5 well cores examined in this thesis along with fault data of the area……...…7

Figure 5. Workflow of integrated reservoir characterization…….…....8

Figure 6. Core A lithology, bioturbation and XRD data……...…….……...13

Figure 7. Core B lithology, bioturbation and XRD……..….....14

Figure 8. Core C lithology, bioturbation, and XRD…….…….15

Figure 9. Core D lithology, bioturbation, and XRD……..17

Figure 10. Core E lithology, bioturbation, and XRD……...…….18

Figure 11. Cross section of all 5 cores from NW to SE……..….....23

Figure 12. Chemostratigraphy for core D…….....27

Figure 13. Chemostratigraphy for core E…….28

Figure 14. Bottom water geochemical properties for core D…….....32

Figure 15. Bottom water geochemical properties for core E…….33

Figure 16. Core D with the 12 zones applied to the lithology and geochemical proxies…….36

Figure 17. Core E with the 12 zones applied with the lithology and geochemical proxies……37

Figure 18. Comparison between XRF raw element curves (blue-green) K, U, and Th, and core gamma-ray calculated (purple) K, U, and Th. Core gamma-ray is shown in red……..……...38

Figure 19. The 12 zones displayed with core A lithology and core gamma-ray calculated elemental curves…….....39

Figure 20. Zone data for core B with lithology and core gamma-ray calculated elemental curves……...40

Figure 21. Zone data for core C with lithology and core gamma-ray calculated elemental curves……...41

Figure 22. Chemostratigraphic correlation of all 5 cores for the 12 stratigraphic zones originally identified in core D and core E…….42

Figure 23. Zone one of core D…….....43

Figure 24. Zone two of core D..……..…….....43

Figure 25. Zone three of core D……..44

Figure 26. Zone four of core D……....44

Figure 27. Zone five of core D……45

Figure 28. Zone six of core D……..……46

Figure 29. Zone seven of core D……...……46

Figure 30. Zone eight of core D……..47

Figure 31. Zone nine of core D……...….....47

Figure 32. Zone ten of core D……..……48

Figure 33. Zone eleven of core D…….48

Figure 34. Zone twelve of core D……..……...49

Figure 35. Zone one of core E…….49

Figure 36. Zone two of core E……..50

Figure 37. Zone three of core E……..……..50

Figure 38. Zone four of core E……..……51

Figure 39. Zone five of core E……..……51

Figure 40. Zone six of core E……..……..52

Figure 41. Zone seven of core E……..…….52

Figure 42. Zone eight of core E……..……..53

Figure 43. Zone nine of core E……..……...53

Figure 44. Zone ten of core E……..…….53

Figure 45. Zone eleven of core E……..……54

Figure 46. Zone twelve of core E……..54

Figure 47. Bottom water conditions for core D with zones indicated……...57

Figure 48. Bottom water conditions for core E with zone indicators……..60

ABSTRACT

Bioturbation creates a physical change in the primary rock structure and mineralogy. It is evidence of past life in the sediments and can assist in determining the depositional environment. Organisms once lived and fed in the strata, consuming organic matter and leaving traces that were filled with material different from the surrounding sediment. Bioturbation is an important factor in reservoir characterization as it has been shown to affect porosity and permeability, be a direct indicator of bottom water oxygen conditions, and with a high enough occurrence, have a direct correlation to total organic carbon content of the sediment. The importance of mudstones (shales) has been recognized for over a century, but they still remain largely understudied.

Technological advances in handheld X-Ray Fluorescence (HHXRF) have been instrumental in demonstrating the utility of chemostratigraphic data to create higher order sequence stratigraphic interpretations. This study seeks to identify the correlation between chemostratigraphy, bioturbation, total organic carbon, and sequence stratigraphy of the Woodford Shale of south-central Oklahoma through the utilization of HHXRF and X-Ray Diffraction (XRD) technologies.

Ichnofossils are identified through detailed core descriptions which are then correlated to the elemental and mineralogical data of the host strata obtained through HHXRF and XRD technologies, respectively. Although individual elements can give valuable information, multiple proxies are used to give the best overall correlation despite exceptions to the standards that are present. Molybdenum and Vanadium are used in conjunction with other proxies to correlate bottom water anoxia because their presence is directly affected by the level of basin restriction that exists – the more restricted the basin

the less trace metal supply being put into the water column which could lead to misinterpretation of bottom water conditions. This correlation will allow for more confident bioturbation identification of the reservoir, and thus aid in the identification of changing levels of bottom water anoxia during reservoir characterization as well as provide quantitative support for the presence of bioturbation in what is typically considered a homogenous deep water black shale. These associations are then tied to wells lacking HHXRF data by correlating with core gamma-ray logs and calculated elemental curves for potassium, uranium, and thorium, thus expanding the higher order sequence stratigraphy to wells lacking chemostratigraphic data.

1. INTRODUCTION

Bioturbation has been studied extensively in conventional reservoirs in the past, and recently researchers have started examining the effects of bioturbation on unconventional reservoirs. Bioturbation is the biogenetic disruption of sediment deposition by burrowing and feeding organisms (Qi, 2012). In 2010 a study was done of the Bakken formation in southeastern Saskatchewan to examine the ichnological stratigraphy; it was noted that, "bioturbation played a key control on the reservoir quality of the rock" (Angulo-Saldina, 2010). A study on the lateral variability in shallow marine ichnofabrics concluded that "ichnofabric analysis is an important tool for reservoir characterization" (McIlroy, 2007). A study published in 2015 for the Unconventional Resources Technology Conference (URTC) found that the amount of bioturbation in the Woodford Shale is more extensive than previously believed, and that the bioturbation is prevalent throughout much of the Woodford Shale (Zou and Slatt, 2015)

The presence of bioturbation in mudstones can be difficult to detect because of the fine grain texture and the dark color. Close examination is required. Pemberton (2015) discusses cryptic bioturbation, which he defines as rocks that appear to be homogenous in texture. This is an important concept when examining the bioturbation features of the Woodford Shale in south-central Oklahoma.

Bioturbation has been shown to be an important factor in reservoir characterization. Qi (2012) concluded that bioturbation was inversely related to porosity, permeability, and oil saturation of the Donghe Sandstone in the Tarim Basin, China. Another recent study examined the impact of bioturbation on reservoir quality of sandstones of the Baram Delta, Sarawak, Malaysia and concluded that an increase in

bioturbation showed a local decrease in porosity and permeability because the sediment fill of the burrows is less well sorted; sediment packing of the burrows incorporates fine grained materials from the host sediment which locally effects permeability (Ben-Awuah and Padmanabhan, 2014). Another study noted that bioturbation can alter both the amount of organic matter and its distribution within the sediment layer through the secretion of mucus and subsequent attachment of organic matter in the burrow wall. (Zorn, 2009). Furthermore, bioturbation is an indicator of relative bottom water oxygen levels which is supported quantitatively through elemental proxies collected through handheld x-ray fluorescence (HHXRF) data.

The Woodford Shale has in the past been considered a homogenous black shale with three main divisions. However, recent studies have shown that it is possible to divide the Woodford Shale into several higher order divisions with the inclusion of chemostratigraphic data collected with HHXRF technologies (Tréanton, 2014; and Turner, 2016). The idea of applying proxies for depositional conditions is not new, however, the use of raw elemental curves as proxies for those conditions is a relatively new concept (Rodrigues, 2007; Harris et al., 2013; McCreight, 2014; Tréanton, 2014; Nance and Rowe, 2015; Turner et al., 2015; Turner, 2016).

The aim of this thesis is to first, advance the understanding of the Woodford Shale through the correlation of traditional sequence stratigraphy, bioturbation, Total Organic Carbon (TOC) content, and chemostratigraphy; and second, to show the viability of utilizing chemostratigraphic data as a tool in reservoir characterization.

1.1 OBJECTIVES

This study seeks to find if there is a correlation between Total Organic Carbon (TOC) content, chemostratigraphy, sequence stratigraphy, and bioturbation within the Woodford Shale of south-central Oklahoma. The specific objectives of this study are:

1. Describe and interpret the sedimentary facies of the Woodford Shale Formation in south-central Oklahoma from five different conventional cores
2. Correlate bioturbation identified in cores with chemostratigraphic profiles of the same well.
3. Address the question: Can chemostratigraphic profiles be used to create higher order sequence stratigraphic interpretations in adjacent wells where only wireline log data are available?
4. Use chemostratigraphic correlations and identified bioturbation to identify changes in bottom water conditions throughout the deposition of the Woodford Shale.

Shale formations have, until recently, been thought of primarily as source rocks and little is still known about their complexities. More and more studies are being completed on shale formations and the vast differences between them are being identified as they have moved from source rock to reservoir rock. Bioturbation has proven to be an important feature in reservoir characterization of conventional reservoirs. While identification of ichnofossils is difficult in shales, especially in black shale, it can be an important factor in constructing a more complete picture of the reservoir. In unconventional reservoirs, just as in conventional reservoirs, a thorough understanding of the vertical and lateral facies variations, as well as deciphering the depositional

environment is necessary to fully understand the reservoir's properties and how they will effect well performance.

While a great deal of work has been done on the Woodford Shale at the University of Oklahoma, from large scale seismic to small scale geochemistry (Portas, 2009; Miceli-Romero, 2010; Badra, 2011; Gupta et al., 2011; Sierra, 2011; Althoff, 2012; Amorocho, 2012; Chain, 2012; Killian, 2012; Mayorga, 2012; Molinares, 2013; Serna-Bernal, 2013; Tréanton, 2014; Slatt et al., 2015; Turner et al., 2015; Zou and Slatt, 2015; Turner, 2016), this thesis seeks to further those efforts and provide a better understanding of the fluctuations in bottom water conditions while providing a way to apply information obtained from core and outcrop to areas where little more than well logs are available for study. Several recent studies (Tréanton, 2014; Slatt et al., 2015; Turner et al., 2015; Zou and Slatt, 2015; Turner, 2016) have shown the significance of correlating chemostratigraphic profiles created by the use of XRF technology. By showing a correlation between mineralogical signatures of the elemental components, TOC, and bioturbation of cores in the Woodford Shale, the same patterns and signatures can be tied to wells lacking core for a more detailed understanding of the vertical and lateral facies variation within the formation.

1.2 GEOLOGICAL CONTEXT

1.2.1 Regional Geology

The Woodford Shale is late Devonian and early Mississippian in age and is one of many Devonian black shales (Krystyniak, 2005). The Woodford Shale covers much of the state of Oklahoma and is structurally contained within several basins: the Arkoma

Basin, the Anadarko Basin, the Ardmore Basin, the Marietta Basin, and the Cherokee Platform. Figure 1 shows the major geological provinces of Oklahoma.

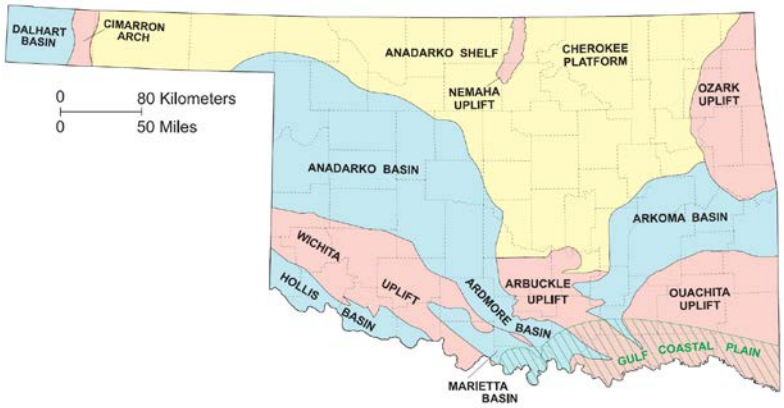

Figure 1. Major Geological Provinces of Oklahoma with color coding based on the dominate structure of the basin: red indicates an uplift structure, blue indicates a basinal structure, and yellow indicates shelf/platform structures. (http://www.ogs.ou.edu/MapsBasid/Provinces.jpg).

The Anadarko basin is located in west-southwestern Oklahoma and into Texas, New Mexico, and Kansas and is aerially the largest of the basins. Only the southeast corner of the Anadarko basin is examined in this study. The Ardmore basin is located in south-central Oklahoma and is bordered to the north by the Arbuckle Mountains and to the south by the Marietta Basin. The Cherokee Platform is located between the Arkoma Basin and the Anadarko Basin in central Oklahoma, and just east of the Nemaha uplift. The Arkoma Basin, located in the east-central part of Oklahoma and western Arkansas is not examined in this study. Figure 2 shows the stratigraphic relationships of the Woodford Shale and other formations in south-central Oklahoma. The Woodford Shale is bound laterally at the base by an unconformity which overlays the Lower Devonian Hunton Group (Sullivan, 1985).

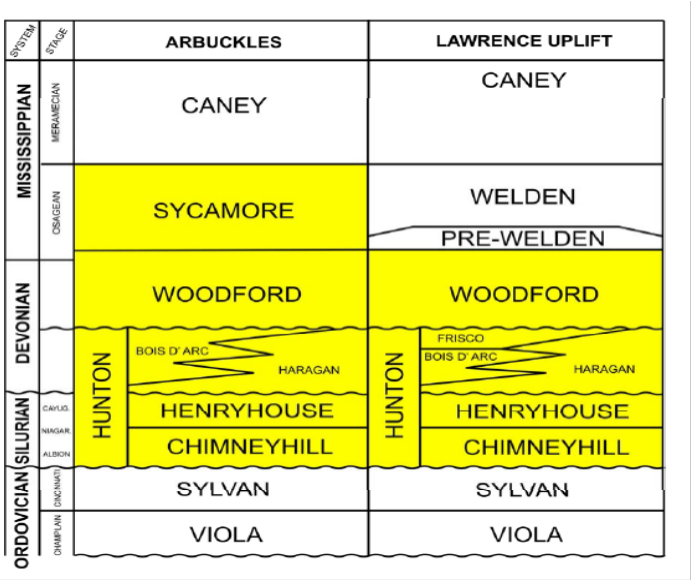

Figure 2. Stratigraphic relationship of the Woodford Shale with overlying Sycamore and underlying Hunton Group (Krystyniak, 2005).

Traditionally, the Woodford Shale has been divided into lower, middle and upper members; however, more recent studies have shown a more complex sequence stratigraphy (McCullough, 2014; Zou and Slatt, 2015). The lowermost portion of the Woodford is generally characterized by a higher total organic carbon, a lightening in the color of the mudstone and relatively few chert beds. The middle portion of the Woodford is generally characterized by alternating chert and mudstone beds with the number of chert beds decreasing as depth increases. The upper portion of the Woodford Shale is, in general, siliceous mudstone interbedded with chert. Locally abundant chert, phosphate nodules, and pyrite nodules (and framoids) are common throughout. Figure 3 summarizes these three informal divisions.

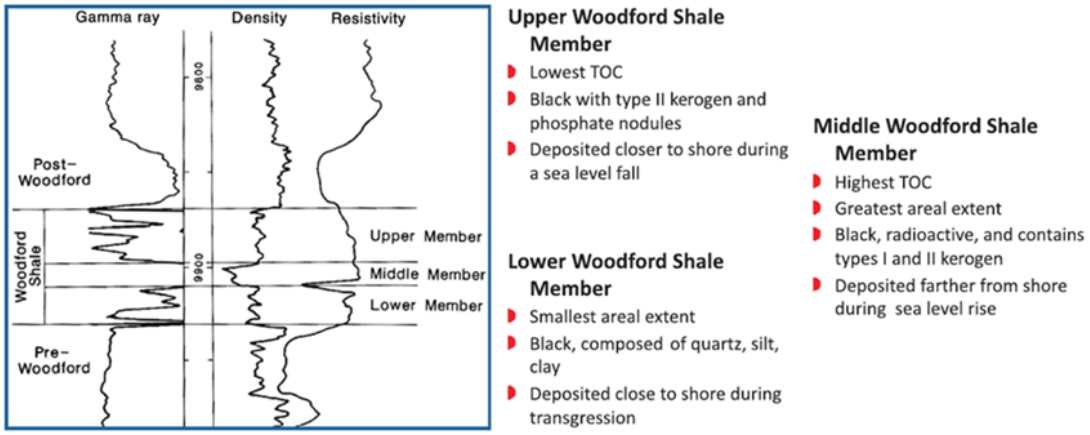

Figure 3. Woodford Shale type log subdivided into three informal members (Hester et al., 1988; in Tréanton, 2014).

1.2.2 Study Area

The cores examined in this thesis are all located in Oklahoma: Core A and B are located in Johnston County; core C is located in Marshall County; core D is located in McClain County; and core E is located in Bryan County. The cores are situated primarily within the Ardmore Basin, however, core D is located in the southeastern portion of the Anadarko Basin. Figure 4 shows the general location of the examined cores.

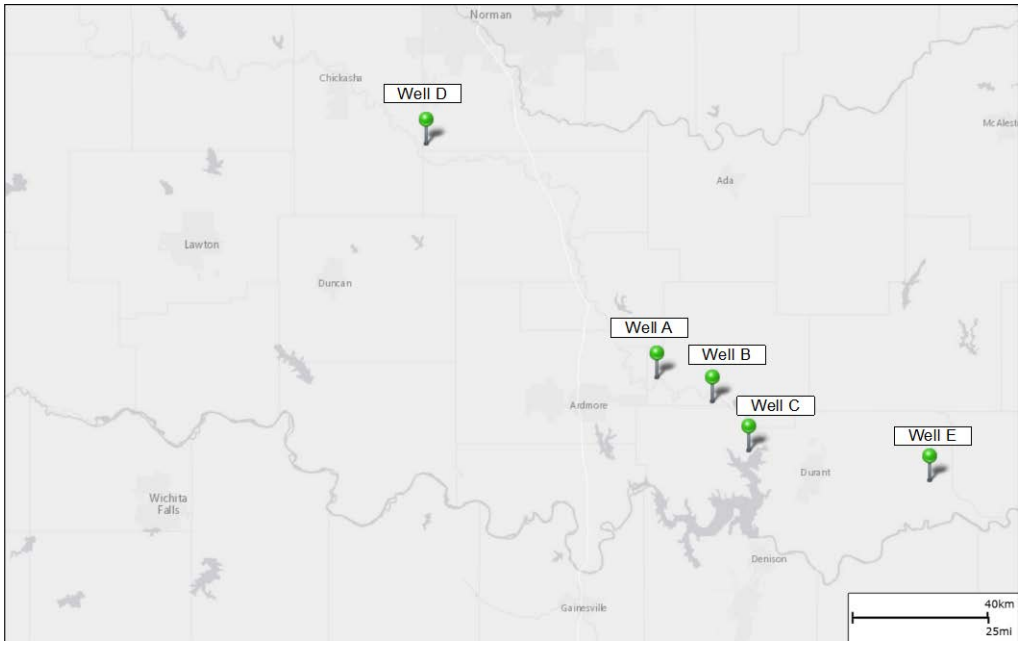

Figure 4. Location map of 5 well cores examined.

2. METHODS

The workflow for reservoir characterization proposed by Slatt et al. (2012), shown in Figure 5, was used as a guideline throughout the work of this thesis. Detailed core descriptions were completed with a focus on lithology and the presence or lack of bioturbation in order to determine rock composition and lithofacies. X-ray fluorescence (XRF) was completed at a four-inch resolution scale in core D and core E in order to reconstruct the chemostratigraphic and bottom water conditions at the time of deposition. Core gamma-ray logs were used for correlation between cores, regardless of the availability of chemostratigraphic data. Gamma-ray data were collected from the cores, therefore, core to log depth correction was not necessary in this study.

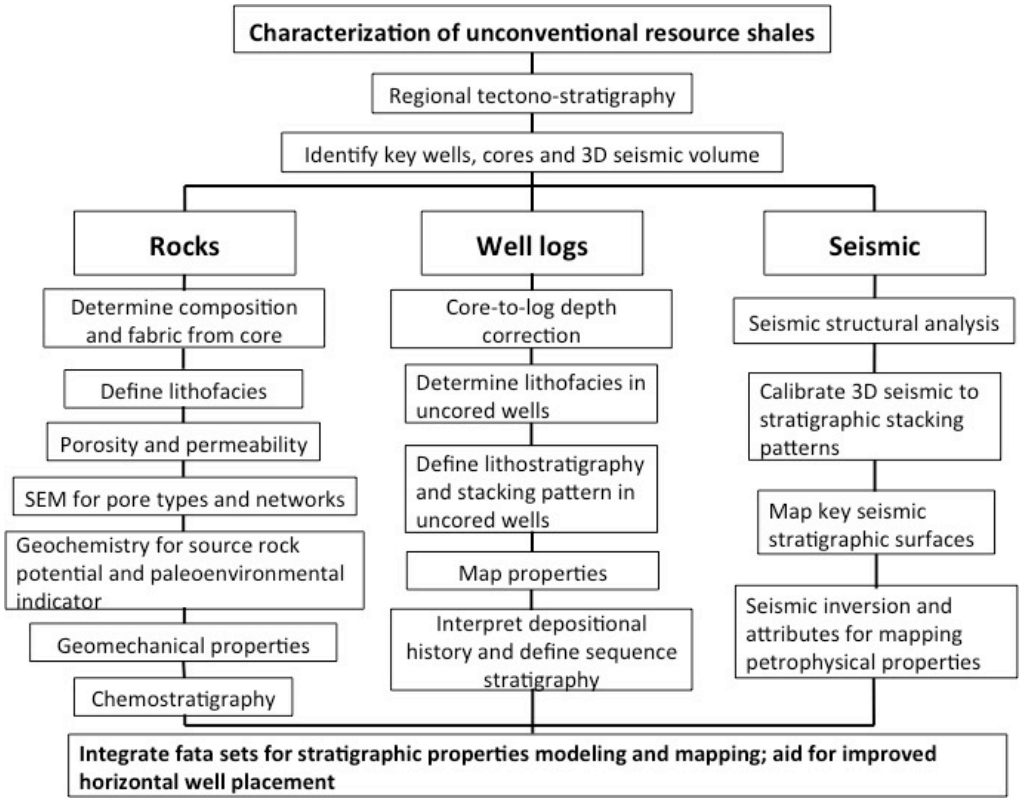

Figure 5. Workflow of integrated reservoir characterization (Slatt, 2016).

2.1 DATA AVAILABLE

All data were provided by Chesapeake Energy and included a total of five conventional cores. There were a total of 1,318 feet of Woodford core described for this thesis that stretched across south-central Oklahoma (Figure 4). Each core also had an assortment of data available for use, however, data used in this thesis included XRD data at a 2-foot resolution, TOC data, and core gamma-ray logs. XRF data was collected at a 4-inch resolution specifically for this thesis using the equipment and facilities provided by Chesapeake Energy.

2.2 X-RAY FLOURESCENCE

X-Ray fluorescence was performed using the Bruker HH-XRF SOP. Each sample location was washed to remove drilling mud remnants on the surface because elements in the mud can interfere with XRF readings. A good indicator of poorly cleaned samples is a peak in Barium (Ba); if this occurred the sample was re-cleaned and the test was run again. Samples were read directly off the core face by placing the core face down on the instrument, which is attached to a metal stand and box fabricated by Chesapeake to prevent unnecessary radiation exposure, with the beam pointing upward. Careful precaution was taken to sample the most homogenous point in the depth of reference. Samples were taken every two or four inches depending on lithologic variation between sample points. Full 2-inch resolution was not obtained due to timing constraints. Samples were analyzed for both major and trace elements. Major element analysis was undertaken at 15 kV, and 55 µA, under vacuum and a count time of 60 seconds. Trace element analysis was undertaken at 40 kV, 14 µA, under vacuum, with an Al-Ti-Cu filter, and a

count time of 120 seconds. Calibrations established for mudrocks in Rowe et al. (2012) were used in the Bruker excel macro for data processing.

2.3 X-RAY DIFFRACTION

X-Ray diffraction (XRD) data was collected using the D4 Endeavor X-Ray Diffraction System for all five cores. The XRD data is quantified using the full-pattern fitting method because it takes into account instrument effects, identifies missing phases and quantifies amorphous phases (Chipera & Bish, 2002). Samples are collected from 2-inch sections spaced approximately 2 feet apart. Homogenous powders are then created providing an effectively infinite number of crystallites for improved counting statistics, to help ensure crystallites are randomly oriented, and ensuring that all crystallographic faces are presented to the beam.

2.4 TOTAL ORGANIC CARBON

Total organic carbon (TOC) was calculated by the Chesapeake's RTC laboratory where careful sample preparation is done to ensure the most accurate results. Each sample is prepared in a clean and cooked crucible and then digested with two washings of 500uL of 5N HCl and a final wash with distilled water. The sample is allowed to dry thoroughly between each washing. Once the digestion is complete the samples are topped with cooper and Lecocell II accelerants. A lid is placed on each crucible and the sample is analyzed using the LECO C230 system.

3. RESULTS AND DISCUSSION

3.1 CORE DESCRIPTIONS

Core A is located in Johnston County, Oklahoma and includes the entire Woodford Shale from base to top, totaling 344 feet. A detailed core description is located in Appendix A. Core B is located in Johnston County, Oklahoma and includes the top and base of the Woodford Shale, but is missing 60 feet of core starting at 6,109 feet for a of total 244 feet—not including the missing section. A detailed description is available in Appendix B. Core C is located in Marshall County, Oklahoma and includes the entire Woodford Shale from base to top, totaling 278 feet. A detailed core description of core C is available in Appendix C. Core D is located in McClain County, Oklahoma and includes the entire Woodford Shale from base to top, totaling 192 feet. A detailed core description is available in Appendix D. Core E is located in Bryan County, Oklahoma. It does not include the entirety of the Woodford Shale, but according to well logs includes the majority of the interval and totals 180 feet. A detailed core description is available in Appendix E. Each core contains intervals, clearly marked in core descriptions, that are either missing core or the core is poorly preserved and is in no condition to accurately describe.

3.1.1 Lithofacies

There are four main lithofacies identified in each of the cores. A dark brown siliceous mudstone (FM1) is prominent and could be further broken down into laminated and massive facies but is grouped for the purpose of this study. FM2 is a dark blue to black chert. This facies often contains fractures, many of which were conchoidal in nature – syneresis cracks, and sharp borders are present at the base and top of these beds.

Disseminated pyrite is also common in FM2. FM3 is a greenish-gray mudstone that is frequently found to be bioturbated. The green color is likely due to partial reduction of the iron coatings of the grains (Myrow, 1990). FM4 is a gray silty mudstone facies that is generally associated with bioturbation. This lighter color indicates both a partial reduction in the iron coating of the grains as well as a lower TOC (Myrow, 1990). While pyrite is not being included in the lithofacies, it is prominent in many sections of the five cores with beds reaching up to 1-inch in thickness. Lithology is noted every two inches, but is upscaled here for imaging and correlation purposes to 6-inch intervals.

Core A (Figure 6) has several sections of core toward the base that are poorly preserved, however, the lowermost portion – from the base up to 8,800 feet – consists of alternating beds of siliceous brown mudstone (FM1) and greenish-gray mudstone (FM3) with local beds of gray silty mudstone (FM4) and chert (FM2). Pyrite is present in laminations and very thin beds with few being thicker than 1". The lower-middle portion of core A – from 8,800 feet to 8,700 feet – has fewer rubble sections and is predominantly alternating beds of FM1 and FM2. Pyrite laminations are common in this portion of the core and several occur in beds up to 1" thick. There are some local beds of grey mudstone (FM4) present, but no FM3 beds are present in this portion of the core. The upper-middle portion of core A – from 8,700 feet to 8,627.5 feet – consists mostly of FM1 with local beds of FM2 and FM3. Pyrite is present in this portion as very thin laminations and burrow fill. The upper section of core A consists of alternating beds of FM1 and FM2 with the FM2 beds thickening upsetion. Pyrite is present in the form of laminations and burrow fill, and a thicker bed of pyrite exists at 8,595.5 feet. A section of FM3 and FM4 is present at 8,534'.

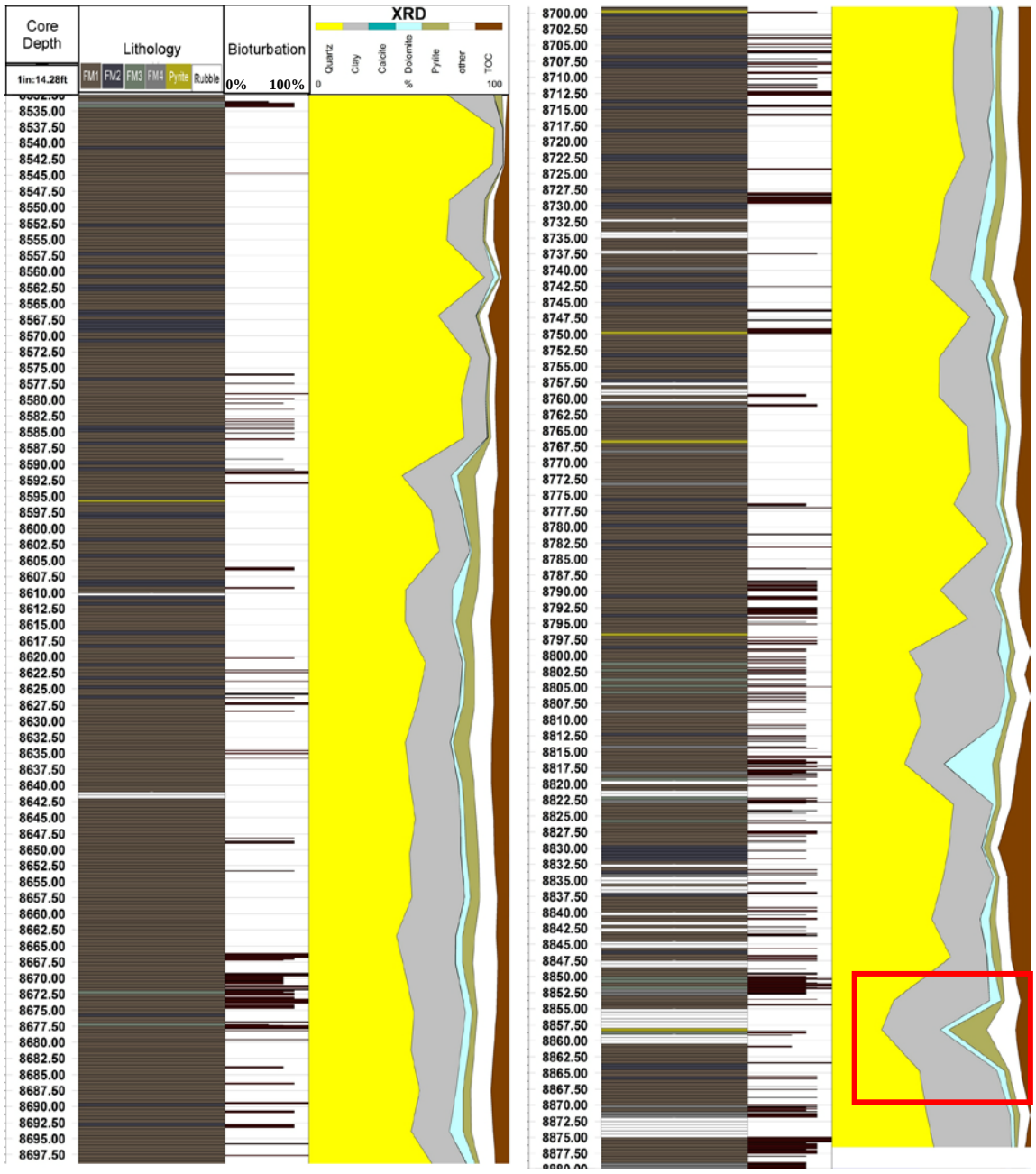

Figure 6. Core A lithology, bioturbation and XRD data. Red box indicates section of lower TOC discussed in section 3.2.

Core B (Figure 7) is well preserved but is missing a 60-foot section in the middle from 6,109 feet to 6,169 feet. Core B does not contain any beds of pyrite that are up to 1-inch although pyrite laminations and burrow fills are present. The lower portion of core B – from the base to 6,207.5 feet – consists primarily of siliceous mudstone (FM1) with

chert (FM2) beds being the next dominant type of lithology. Local beds of greenish-gray mudstone (FM3) and gray silty mudstone (FM4) are present. The middle portion of core B – 6,207.5 feet to 6,042 feet – consists of alternating beds of FM1 and FM2. The frequency and thickness of FM2 beds decrease upsection here. The upper portion of core B is primarily FM2 interbedded with FM1. There is a large bed of FM4 present from 6,031 feet to 6,026 feet.

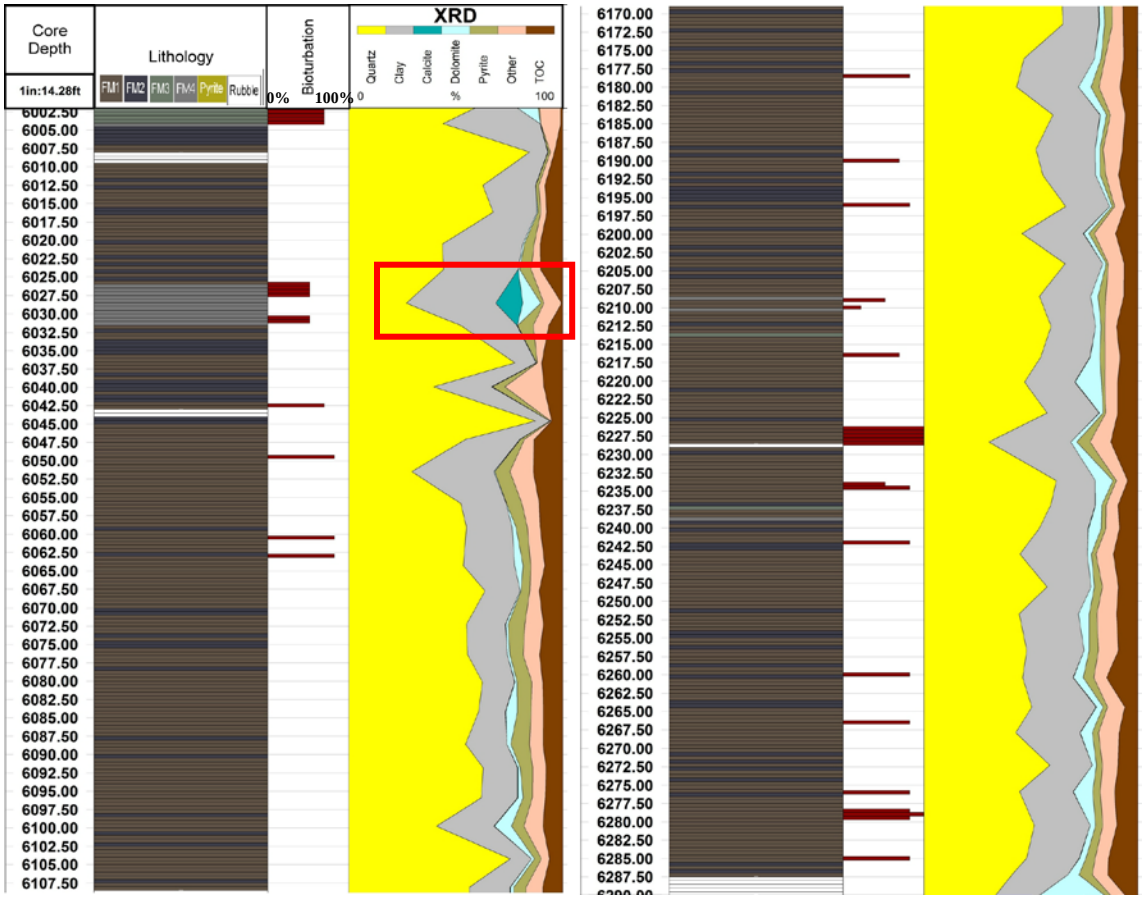

Figure 7. Core B lithology, bioturbation and XRD. The missing section of the core from 6109'-6169' has been removed for display purposes. Red box indicates the calcite zone discussed in section 3.2.

Core C (Figure 8) is fairly well preserved with only a moderate amount of rubble or missing core sections. Pyrite is present in the form of laminations and burrow fill for the majority of the core. Core C does not have the Hunton unconformity present at the

base of the core due to a missing core section. The lower most portion of core C – from the base to 6,785 feet – is predominantly siliceous mudstone (FM1) locally interbedded with chert (FM2) and a single bed of greenish-gray mudstone (FM3) at 6,808 feet. The middle portion of core C – from 6,785 feet to 6,637.5 feet – is primarily FM1 with FM2 interbedded and increasing upsection. There are local beds of gray silty mudstone (FM4) and pyrite laminations throughout and a pyrite bed at 6,702 feet. The upper portion of core C consists primarily of interbedded FM2 with FM1. The very top of Core C is a thick, 5-foot, bed of FM3 gradationally fading into a 4-foot bed of grey silty FM4.

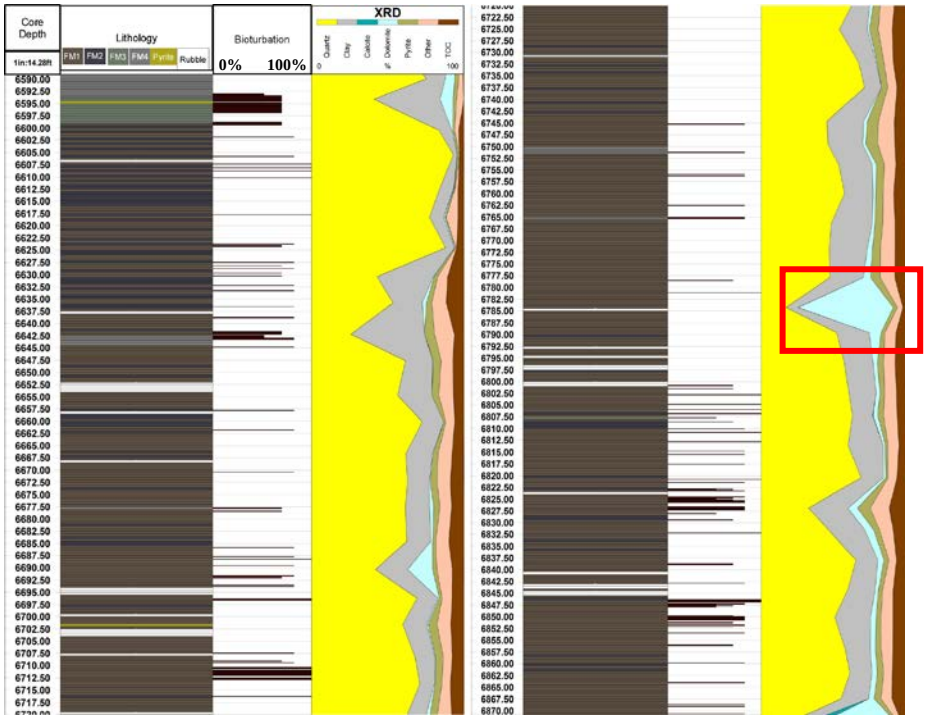

Figure 8. Core C lithology, bioturbation, and XRD. The red box indicates the dolomitic zone discussed in section 3.2.

Core D (Figure 9) is moderately well preserved with rubble sections or missing core sections throughout. The lower portion of the core – from the base to 9,982.50 feet – is primarily siliceous mudstone (FM1) with local bedding of chert (FM2), greenish-gray mudstone (FM3), gray silty mudstone (FM4), and pyrite. Pyrite beds occur at 10,023

feet and 9,992.50 feet; pyrite laminations are common throughout the lower section of the core. Greenish-grey mudstone (FM3) beds are very common in the lower 10 feet of the core, however, for display purposes the lithology is upscaled to be 6-inch depth step and many of them cannot be seen in Figure 9. The middle portion of core D – 9,982.5 feet to 9917.50 feet – is primarily FM1 with local beds of FM2 increasing upsection. The upper portion of core D consists of FM1 interbedded with FM2. The amount of pyrite decreases upsection, although there is a thin pyrite bed located at 9,901 feet. There is a 4.5 foot bed of FM4 located in the upper portion of the core from 9,875.5 feet to 9,871 foot. Core D is capped by a 2-foot section of greenish-gray mudstone (FM3).

Core E (Figure 10) is vastly different in the lithological makeup. Neither the base or the top of the Woodford Shale is present in this core, however, well logs indicate that the majority of the Woodford is present. Chert (FM2) beds are heavily fractured throughout and are the primary lithology in this core with siliceous mudstone (FM1) interbedded. Pyrite is much more common in this core than in any of the other four cores examined in this study with thin beds and laminations common throughout core E. Local thin beds of greenish-gray mudstone (FM3) and gray silty mudstone (FM4) exist but are not seen in Figure 10. They can be seen in the detailed core description located in Appendix E.

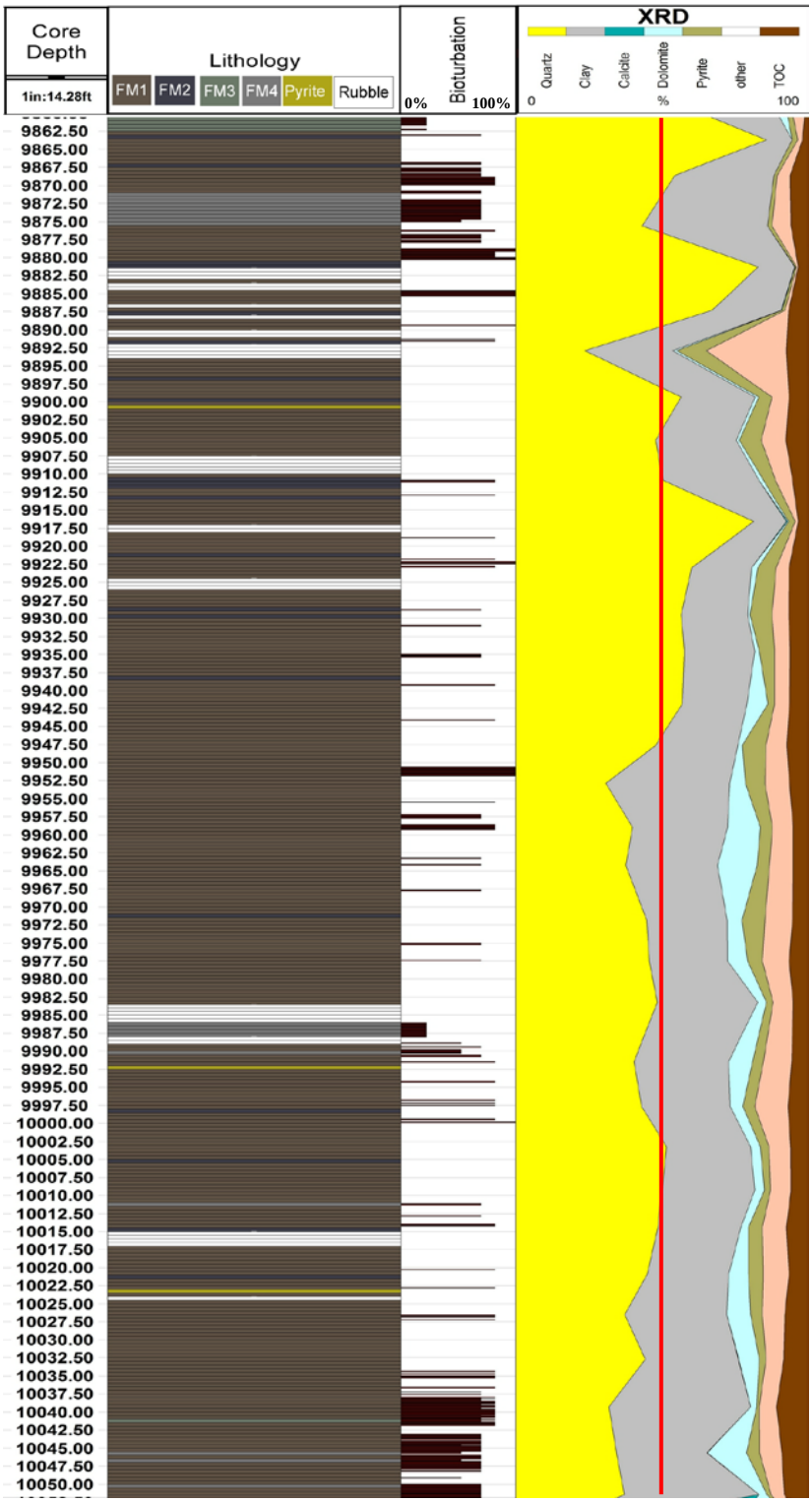

Figure 9. Core D lithology, bioturbation, and XRD. The red line indicates the 50% point and is discussed in section 3.2.

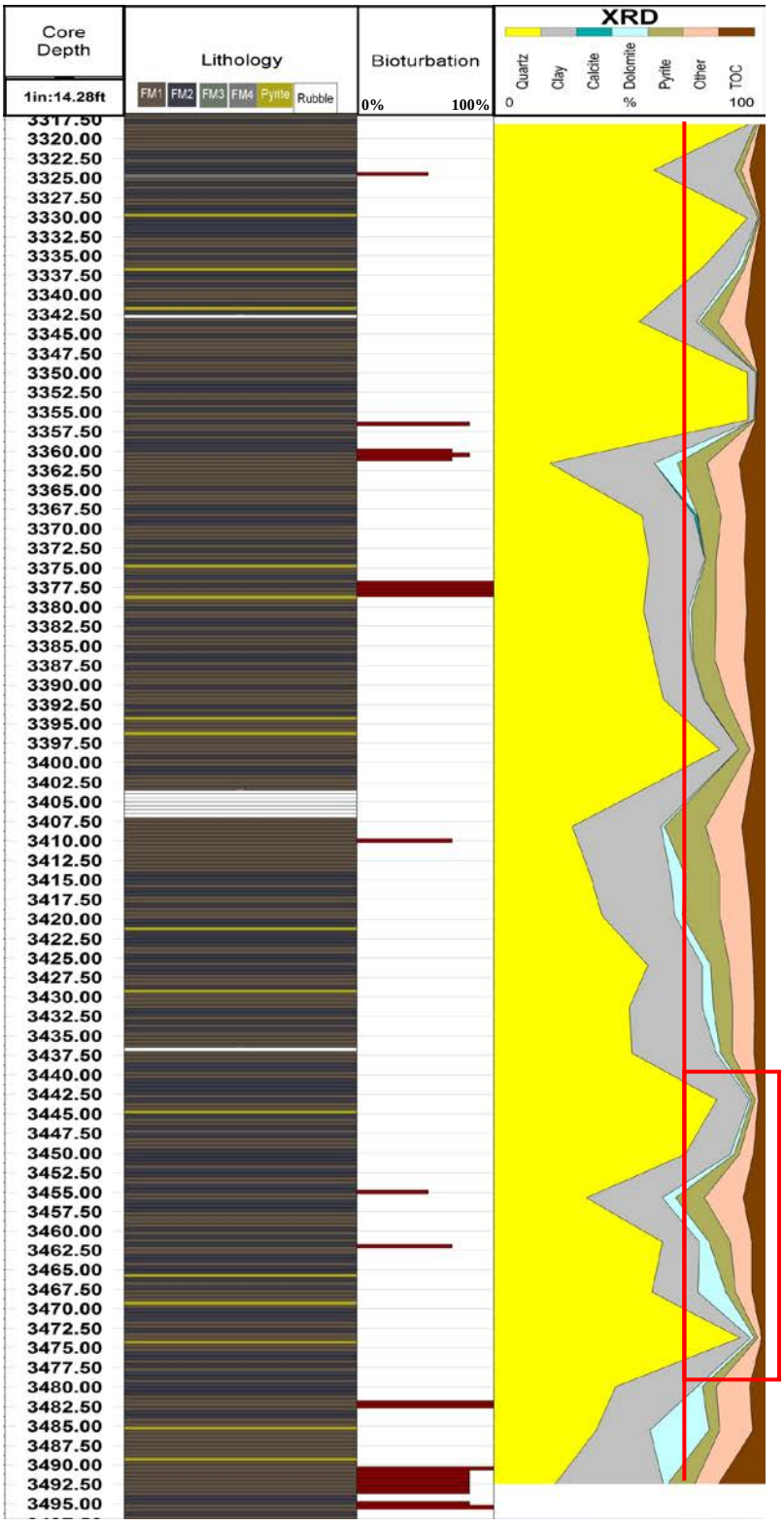

Figure 10. Core E lithology, bioturbation, and XRD. The red line indicates the 70% line and the red box highlights quartz peaks that are discussed in section 3.2.

3.1.2 Bioturbation

Each core was carefully examined for the presence of trace fossils. Most of the trace fossils present are in the form of horizontal burrows. Little of the identified bioturbation is intensive enough to totally disrupt the fabric of the rock. *Planolites* burrows are frequently identified within the Woodford Shale. They are identified by their horizontal, unbranched structure and fall into the lower end of their average length range of 1.25-17.5 cm (Jordan, 1985). They are often siltstone-filled and locally pyrite filled. *Chondrites* are also identified in all five cores. These burrows are typically horizontal and branching; they are often clay-filled, although locally filled with pyrite in areas with pervasive pyrite. *Chondrites* are difficult to see without first wetting the surface of the core and shining light at different angles to illuminate the slight change in coloration. *Paleophycus* are also identified; these often have a dark center with a lighter rim and are horizontal in nature. Much of the bioturbation occurs along the bedding planes. It is possible that more bioturbation exists, but is not possible to confidently identify from the core face. Zou and Slatt (2015) used 3D micro CT scanning to examine the bioturbation of the Woodford shale; their results are similar to those described here.

Core A is heavily bioturbated at the base, and bioturbation decreases upsection. In the phosphate nodular region of the upper portion of the core – 8,575 feet to 8,535 feet – very little bioturbation is present. All greenish-gray mudstone (FM3) facies of core A are bioturbated and most of the gray silty mudstone (FM4) facies are bioturbated (Figure 6). Core B has significantly less bioturbation that could be identified from the core face. There is more bioturbation in the lower section of the core and it decreases upsection (Figure 7). Bioturbation is identified throughout core C with the least amount identified

in the lower-middle section of the core – from 6,792.5 feet to 6,720 feet (Figure 8). Core D is significantly bioturbated in both the lower-most section of the core and in the uppermost section of the core. Bioturbation is common in the middle section of the core within the siliceous mudstone (FM1), greenish-gray mudstone (FM3), and gray silty mudstone (FM4) facies (Figure 9). Core E has the least amount of bioturbation of all five cores. This is to be expected since it primarily consists of chert (FM2) facies in which no bioturbation is identified in any of the cores (Figure 10).

3.2 MINERALOGY AND TOTAL ORGANIC CARBON

Although mineral data and TOC data were collected separately, they are examined together in this study. Mineral data collected with XRD technology shows the same general trends in all five cores. Total organic carbon (TOC) data shows a decreasing trend in TOC upsection in the cores which was supported by the Mo and V indications of bottom water oxygen conditions (will be discussed later). Quartz shows a general increase from the base to the top of each core.

Some notable areas in each core do occur. Core A shows a significant decrease in TOC in the lower portion (8,789.78 feet – 8,810.38 feet) of the Woodford Shale (Figure 6), which correlates with heavy bioturbation which could explain why the TOC is decreased. Core B shows a calcitic zone in the upper portion (6,023.98 feet – 6,031.50 feet) of the core (Figure 7) which is not noted in any other core. This calcite zone is associated with a bed of gray silty mudstone (FM4). Examination of the XRD data points shows that this is the only data point taken directly from an FM4 facies which could explain why core B is the only core with a calcite zone in XRD. Core C shows a strong presence of dolomite in the lower middle portion (6,778 feet – 6,790 feet) of the core

(Figure 8) which is not present in any other core to that quantity. This anomaly may be due to sampling points as well, although this is harder to confirm and more tests would need to be done on core C to determine a reason for the dolomite peak in the lower portion of this core. Core D shows no more than 50% quartz in the lower half (9,947.58 feet and below) of the core (Figure 9) while the other four cores show quartz volumes in the lower portion to be between 50% and 70%. This could be due to the location of core D; cores A-C and core E are located in the Ardmore Basin while core D is located in the southeastern portion of the Anadarko basin. However, core E showed quartz peaks great than 70% in the lower portions (3,431.34 feet – 3,485.48 feet) of the core (Figure 10) which are not present in any of the other cores. This could be attributed to the higher amount of chert in core E compared to the other four cores.

3.3 SEQUENCE STRATIGRAPHY

The gamma-ray (GR) profile was obtained from all five cores and is used to examine the sequence-stratigraphic framework of the core which is correlated to the chemostratigraphic framework (discussed in a subsequent section). In all five cores, a regional maximum flooding surface (MFS) is identified in the upper portion of the core: a regional transgressive system tract is present downsection from the regional MFS, and a highstand system tract is located upsection from the regional MFS. Figure 11 shows the sequence stratigraphy for all five cores with the cross section datum on the regional MFS. Core D shows cycles of transgression and regression with the regional maximum flooding surface noted at 9,950 feet. In the upper portion of core D there is a single area of constant GR where neither transgression nor regression is apparent. Core A shows cycles of transgression and regression with the regional maximum flooding surface noted

at 8,588 feet. Multiple areas of constant GR are present in core A both upsection and down section of the regional MFS. Core B shows cycles of transgression and regression with the regional MFS located at 6,050 feet. Core B has two areas of constant GR located upsection from the regional MFS and one section of constant GR down section of the regional MFS. Core C consists of cyclic transgression and regression with the regional MFS observed at 6,645 feet. There is one section of constant GR observed upsection of the regional MFS in core C, and two sections of constant GR down section of the regional MFS. Core E shows cycles of transgression and regression throughout with the regional maximum flooding surface located at 3,359 feet. Core E has only two sections of constant GR observed; one is upsection and one is down section of the regional MFS.

The Frasnian-Famennien (FF) boundary sits just about the regional MFS and is identified by the light blue line in Figure 11. Traditionally this boundary is based upon conodont biostratigraphy (Johnson et al., 1985), however, Turner (2016) showed that the boundary can be inferred from relative shoreline trajectories. For this study I have used interpreted shoreline trajectories from gamma-ray and chemostratigraphic data to project the FF boundary.

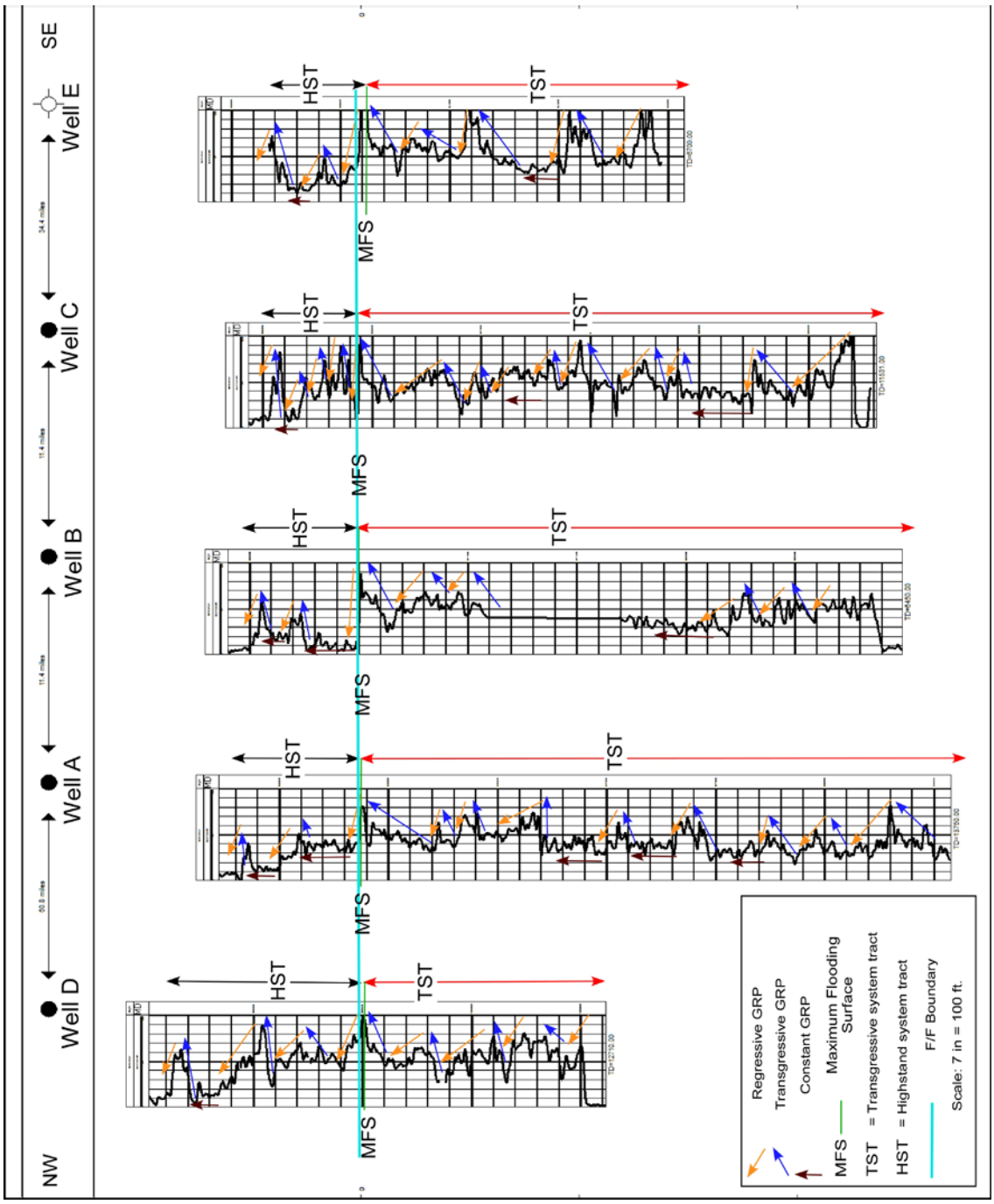

Figure 11. Cross section of all 5 cores from NW to SE showing the regional maximum flooding surface (notated by a green line) along with transgressive, regressive and constant gamma-ray profile (GRP) indications. Transgressive system tracts and highstand system tracts are also notated. The Frasnian-Famennien boundary is represented by the light blue line just above the regional maximum flooding surface.

3.4 CHEMOSTRATIGRAPHY

Fifteen different geochemical proxies are examined in this study for core D and core E. The periodic table is followed for element abbreviations. Both the raw curves and calculated curves from the raw curves are examined. Raw element curves include Ti (titanium), Zr (zirconium), Ca (calcium), Sr (strontium), P (phosphorous), K (potassium), Al (aluminum), Fe (iron), S (sulfur), Ni (nickel), Mo (molybdenum), and V (vanadium). The Si/Al ratio is used in place of raw Si curves to help to identify biogenic Si. Titanium, Zr, Ca, Sr, K, Al, and the Si/Al ratio are used for chemostratigraphic correlations in core D (Figure 12) and core E (Figure 13). Molybdenum and V are used in conjunction with TOC, bioturbation profiles, and other calculated geochemical proxies to interpret bottom water conditions and will be examined later. Plots of XRF data for core D and core E are available in Appendix D and Appendix E, respectively. A list of principle elements and their geochemical proxies can be found in Table 1.

Element	Proxy	Reference
Titanium (Ti)	Continental source and dust fraction	Sageman and Lyons 2004
Zirconium (Zr)	Continental source	Bhatia and Crook 1986
Silicon:Aluminum ratio (Si/Al)	Quartz (biogenic and detrital)	Pearce and Jarvis 1992; Pearce et al. 1999; Sageman and Lyons 2004
Calcium (Ca)	Carbonate source and phosphate	Banner 1995; Tribovillard et al. 2006
Strontium (Sr)	Carbonate source and phosphate	Banner 1995; Tribovillard et al. 2006
Phosphorous (P)	Phosphate accumulation	Tribovillard et al. 2006
Aluminum (Al)	Clay and feldspar	Pearce and Jarvis 1992; Tribovillard et al. 2006
Potassium (K)	Clay and feldspar	Tribovillard et al. 2006
Molybdenum (Mo)	Bottom water euxinia, redox sensitive	Tribovillard et al. 2006; Algeo and Rowe 2012
Vanadium (V)	Bottom water anoxia, redox sensitive	Tribovillard et al. 2006

Table 1. A list of the principal elements used for correlation and their primary stratigraphic proxy (from Turner, 2016).

Titanium, Zr, K, and Al are all detrital elemental proxies and are therefore the strongest proxies for transgression and regression (O'Neal, 2015). Decreases in these detrital proxies would be indicative of a transgressive cycles because it indicates the detrital sediment source is moving away from the distal basin, while increases in these proxies correlate to regressive cycles because it indicates the detrital sediment source is moving toward the distal basin (Turner, 2016). Local shifts in sedimentation correlate with local shifts in the detrital proxies. Titanium and Zr, K, and Al are indicators that the sediment was deposited from the continent, however, K and Al are also associated with clays (Pearce and Jarvis, 1992; Pearce et al., 1999).

High Si/Al ratio and low continental proxies indicate biogenic quartz, and can indicate a flooding surface or algal bloom. Since Si is associated with many different minerals the raw Si curve gives little to no useful information on its own. Areas where there is a strong increase in Si/Al without a corresponding increase in Ti, Zr, or K indicate either a hiatal surface or and algal bloom, preferences to which can be made based on the amount of time the Si/Al ratio is peaked. Longer episodes would likely indicate a hiatal surface of non-deposition while short episodes would indicate an algal bloom (Turner, 2016).

Calcium and Sr are indicators of carbonate deposits (Banner, 1995). In the Woodford Shale Ca is associated with calcite, aragonite, and dolomite; Sr has the ability to substitute into aragonite in place of Ca. While it is possible that Ca and Sr can be transported during diagenesis, when paired with other mineral proxies they provide useful information (Tribovillard et al., 2006). In both core D and core E, Ca and Sr show an inverse relationship to detrital proxy curves of Ti, Zr, K, and Al, indicating carbonate

deposits which would be common during regressive cycles. There are also areas in both core D and core E where Ca and Sr show positive convergence with detrital proxies, these locations also correspond with areas of bioturbation. Although this is not the chemostratigraphic response for all areas of bioturbation, bioturbation is present when this chemostratigraphic response is present.

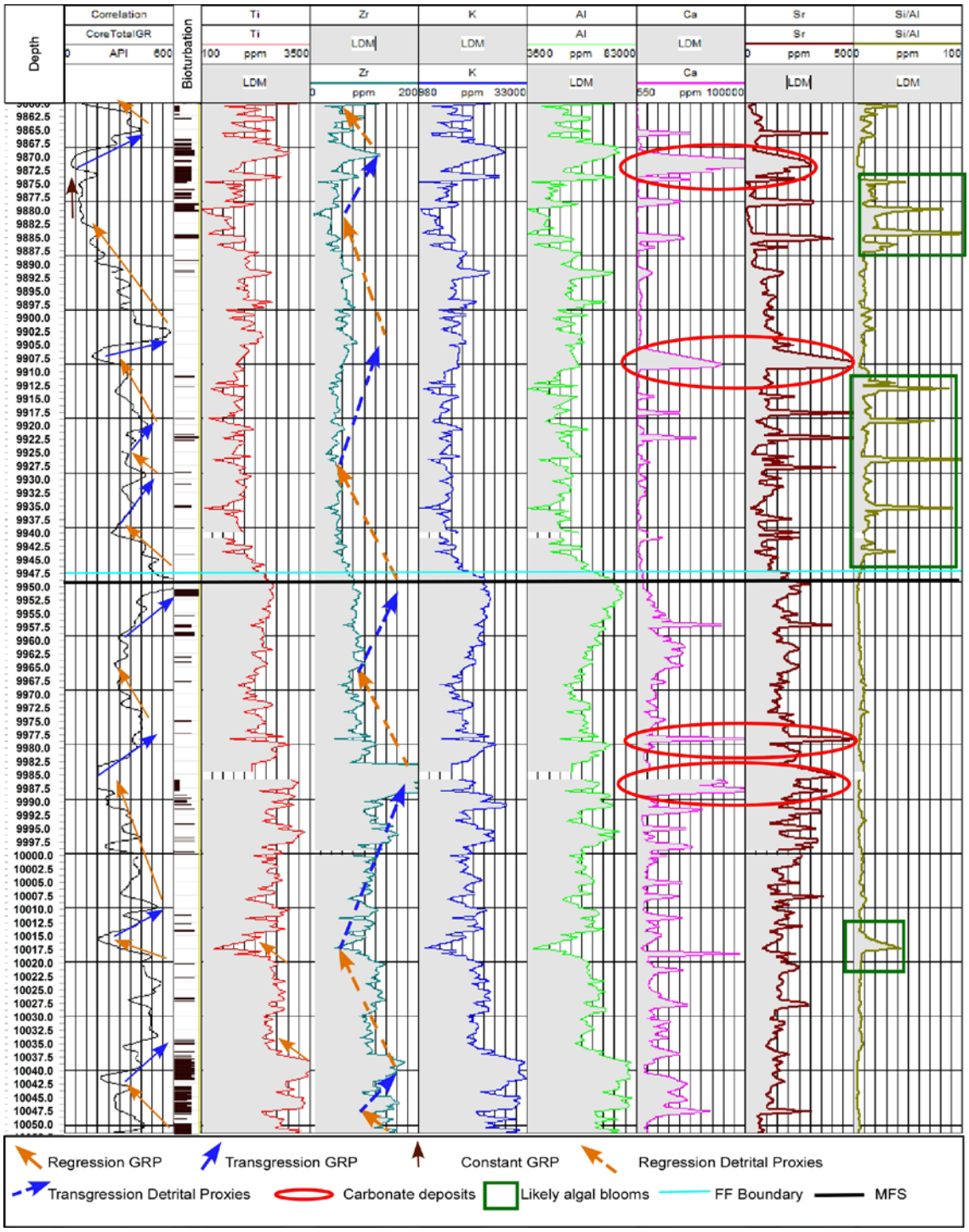

Figure 12. Chemostratigraphy for core D. Red circles are placed around peaks in Ca and Sr as indications of Carbonate deposits which correlate with gamma-ray interpreted regressive cycles. Si/Al peaks are indicated as likely algal blooms because there is not a corresponding increase in detrital proxies. The maximum flooding surface (MFS) is indicated by a solid black line and the FF boundary is indicated by a light blue line.

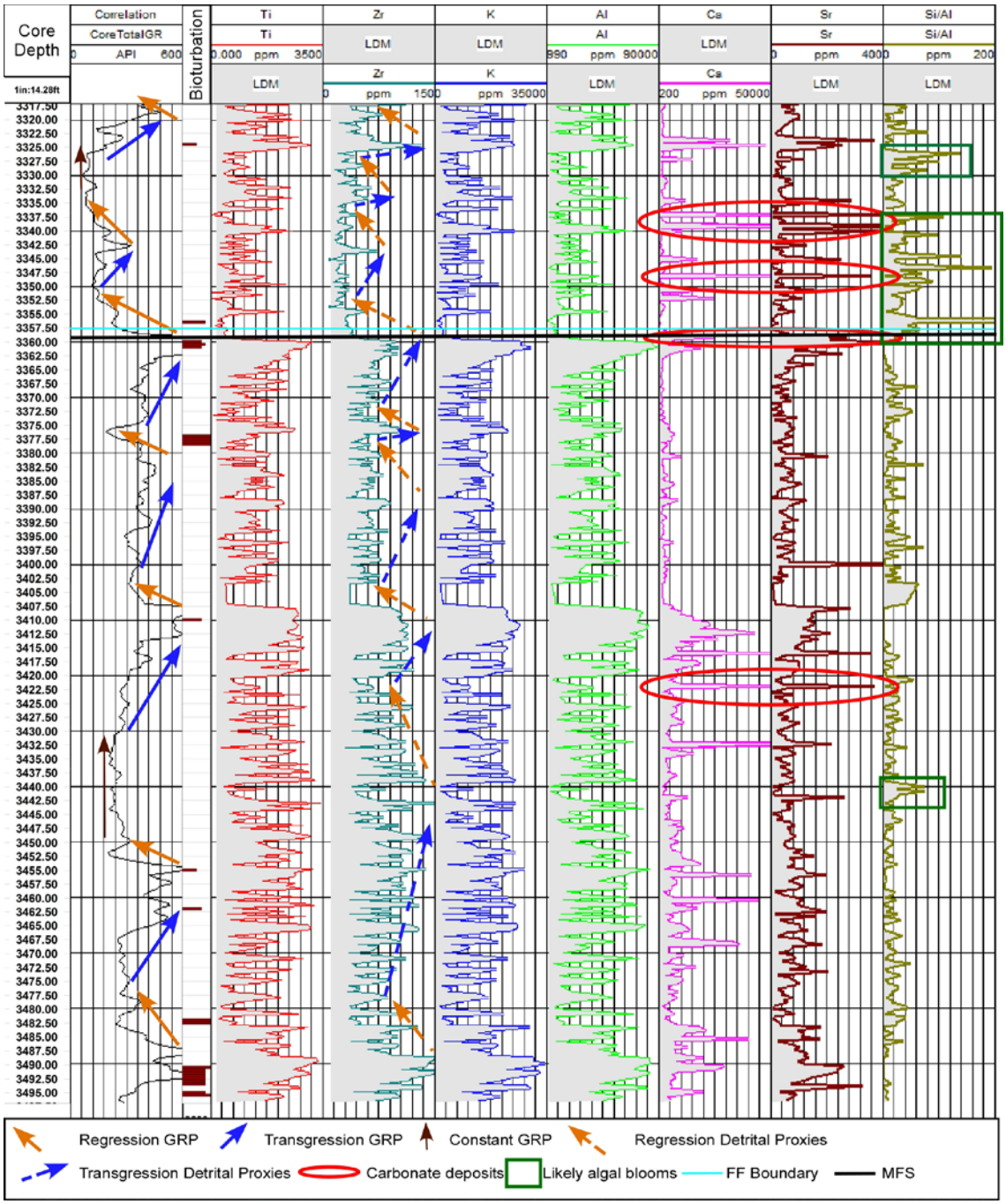

Figure 13. Chemostratigraphy for core E. Red circles are placed around peaks in Ca and Sr as indications of Carbonate deposits which correlate with gamma-ray interpreted regressive cycles. Si/Al peaks are indicated as likely algal blooms because there is not a corresponding increase in detrital proxies. The maximum flooding surface (MFS) is indicated by a solid black line and the FF boundary is indicated by a light blue line.

3.5 BOTTOM WATER CONDITIONS

Bottom water oxygen conditions can be evaluated from data obtained from XRF, TOC, and core descriptions. Elemental proxies that contributed to interpreted bottom water conditions include Mo, V, Ni, P, and some elemental ratios such as U/Th, V/Cr, and V/(V+Ni) (Novek, 2015); however, Zhou et al. (2011) explains that all elements but Mo can be unreliable and easily influenced by outside factors such as depositional changes and diagenetic changes, and for this reason U/Th, V/Cr, and V/(V+Ni) are not used in this study for bottom water condition interpretations. However, Algeo and Maynard (2004) suggest that V is also a viable proxy for indicating reducing environments. Tribovillard et al. (2006) explain that used together, Mo and V, can give further insight into a separation of not just oxic to anoxic; Vanadium is often locked down in suboxic to anoxic while Mo is sequestered more in anoxic conditions. There are exceptions to every case; one important consideration when interpreting Mo and V is that they are directly related to basin restriction – the more restricted a basin the less trace metal supply being put into the water column, thus giving depleted values despite the bottom water conditions. Another important consideration from Tribovillard et al. (2006) is that phosphate material can form chemical bonds with trace metals leading to a higher reading despite bottom water conditions.

Molybdenum and V were not the only proxies used in understanding the bottom water conditions: degree of pyritization (DOP), bioturbation, TOC – and its geochemical proxy Ni (nickel) – were also used. The degree of pyritization (DOP) is also a valuable tool in determining bottom water conditions (Raiswell et al., 1988). Collecting DOP data requires determining the amount of HCl soluble iron there is, however, Howe (2016)

explained that the Fe/S ratio can be used as a proxy for the DOP with the understanding that these would be under ideal conditions; all of the iron and sulfur is used first to form pyrite until one or the other was no longer available. Bioturbation can provide relative information on bottom water conditions, that when combined with geochemical proxies, strengthens the overall understanding because the presence of bioturbation requires there to be some amount of oxygen present in the sediment layer during deposition (O'Neal, 2010). When examining the relationships between pyrite, bioturbation, TOC, and geochemical proxies of core D and core E we see certain indicators which give information on the general bottom water conditions.

Nickel is used as a proxy for TOC in this study because it is enriched in organic molecules and shows a positive covariance with TOC. Since Nickel was measured using XRF in core D and core E at 4-inch intervals it creates a higher resolution correlation for bottom water condition evaluations with Mo and V (O'Neal, 2010). When studying bioturbation in core D and core E those areas of highest bioturbation are generally identified in areas of low Mo, V, TOC, and pyrite. However, bioturbation is present in areas of decreasing oxygen as indicated by bottom water condition proxies. There is not a precise cutoff between oxic and anoxic for the more reliable proxies – Mo and V – and therefore, there could be areas where the water is suboxic where makers of *Chondrites*, which require very little dissolved oxygen to exist, are responsible for most of the visible bioturbation. When compared to cycles of transgression and regression from the gamma-ray profile the bottom water appears to generally increase in oxygenation through periods of regression and decrease in oxygenation through periods of transgression in both core D (Figure 14) and core E (Figure 15). There are areas in both cores which show increased

V in areas of decreased Mo, however, these same areas had an increase in P indicating that the increase in V could be due to the presence of P and not because oxygen levels are decreasing (Tribovillard et al., 2006, Turner, 2016). These areas are indicate by red circles in figure 14 and figure 15.

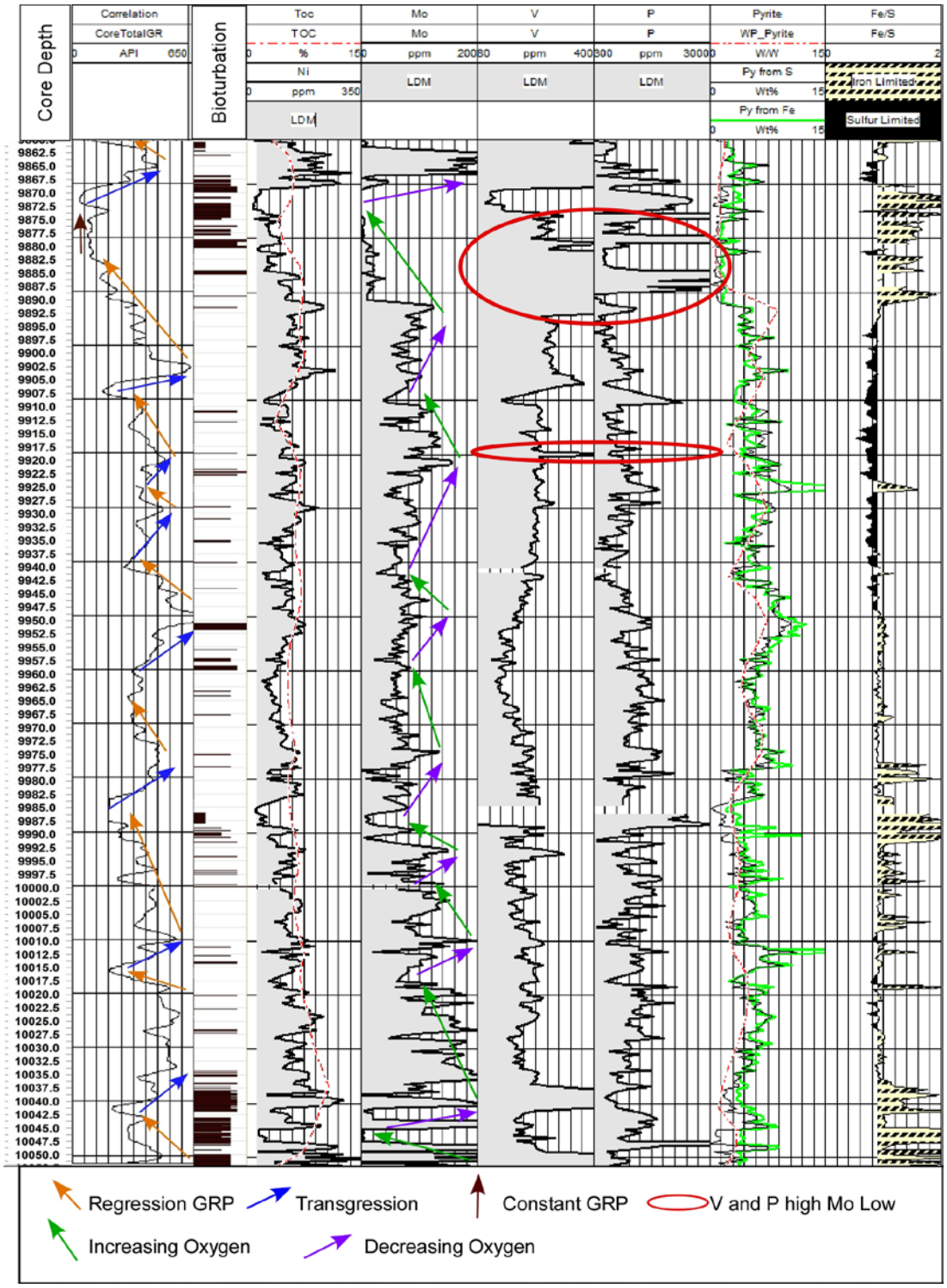

Figure 14. Bottom water geochemical properties for core D with green and purples arrows indicating increasing and decreasing oxygen levels, respectively, showing a positive correlation with regressive and transgressive cycles in the GRP. Red circles indicate areas of high V and P with low Mo.

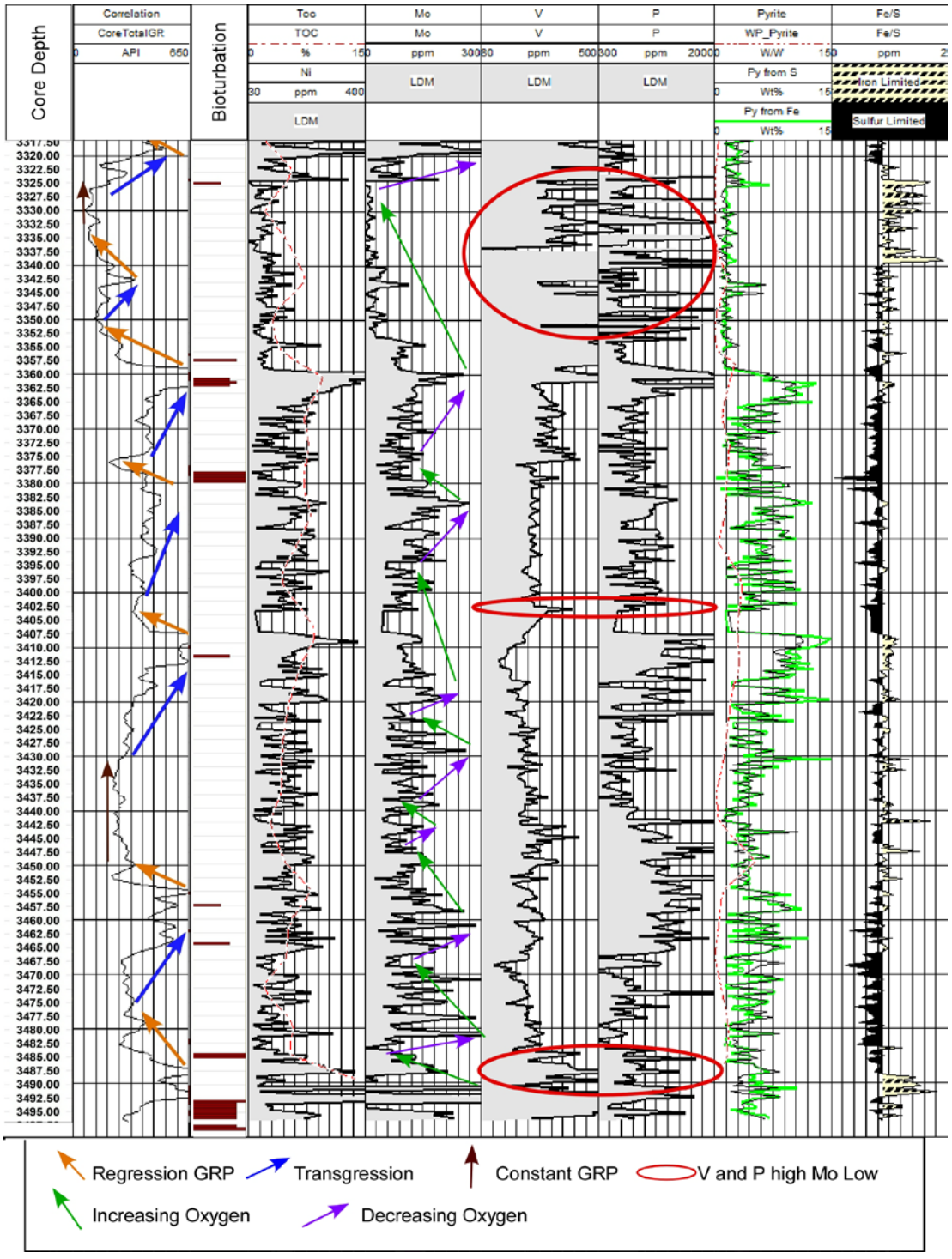

Figure 15. Bottom water geochemical properties for core E with green and purples arrows indicating increasing and decreasing oxygen levels, respectively, showing a positive correlation with regressive and transgressive cycles in the GRP. Red circles indicate areas of high V and P with low Mo.

4. CORRELATIONS

XRF data collected on core D and core E is used to correlate stratigraphic zones between the two cores. Without the elemental fluctuations it would not have been possible to identify as many zones as was done. Too many shale beds gave little variation in the gamma ray logs alone to make confident predictions (Tréanton, 2014). However, once the elements were incorporated, more confident correlations could be made. The use of chemostratigraphic correlations is a relatively new idea which has shown great success (Pearce et al., 1999; Tréanton, 2014; O'Neal, 2015; Turner et al., 2015; and Zou and Slatt, 2015; Turner, 2016).

While a useful tool, XRF data is not a perfect replication of the elemental breakdown in the sample (Loubser and Verryn, 2008). First, it should be noted that while a 4 inch resolution leaves little room for variations between readings that does not mean that laminae cannot be missed. To keep readings at a specific depth step, some thinner beds differing from the surrounding mudstone may have been missed – even when a two inch resolution was used. Secondly, HH-XRF equipment performs spot analysis; multiple scans at the same depth could yield different results. Although great care was taken to ensure the most homogenous point in the zone was measured, there is still room for error. Lastly, improper cleaning can leave traces of elements on the surface that are not actually present in the rock. In this study an elevated Barium reading would indicate that the sample still has drilling mud present and was not properly cleaned. Even with all of these cautions against the XRF data, it is still a valuable technique as demonstrated in this and previously mentioned studies because even if the number is not exact the overall trends in the data are what correlations are made from.

Based on the chemostratigraphy twelve different stratigraphic zones were correlated in core D (Figure 16) and core E (Figure 17). No XRF was run on core A, B, or C. However, U (uranium), Th (thorium), and K (potassium) data is available from core gamma-ray calculations. The data calculated from the core gamma-ray logs, while not an exact match, follows the same trend as the XRF acquired U, Th, and K of core D (Figure 18) and E. Therefore, the overall trends of these three elements are able to be used for general correlation purposes. All twelve zones are correlated in core A (Figure 19), core C (Figure 21), core D (Figure 16) and core E (Figure 17). The 60-foot missing section in core B (Figure 20) makes the identification of the top of zone 4 and the base of zone 6 impossible to discern although the trends match with the other cores and zone data has been assigned to all available thickness. The total thickness of zone one and zone twelve in core E are not available due to lack of core. The total thickness of zone four, zone five, and zone six in core B cannot be identified. Each zone has variations in thickness in each core and varying numbers of transgressive and regressive cycles. However, the overall trend of the data is the same in each core. The full cross sections of all 5 cores with zones can be seen in figure 22.

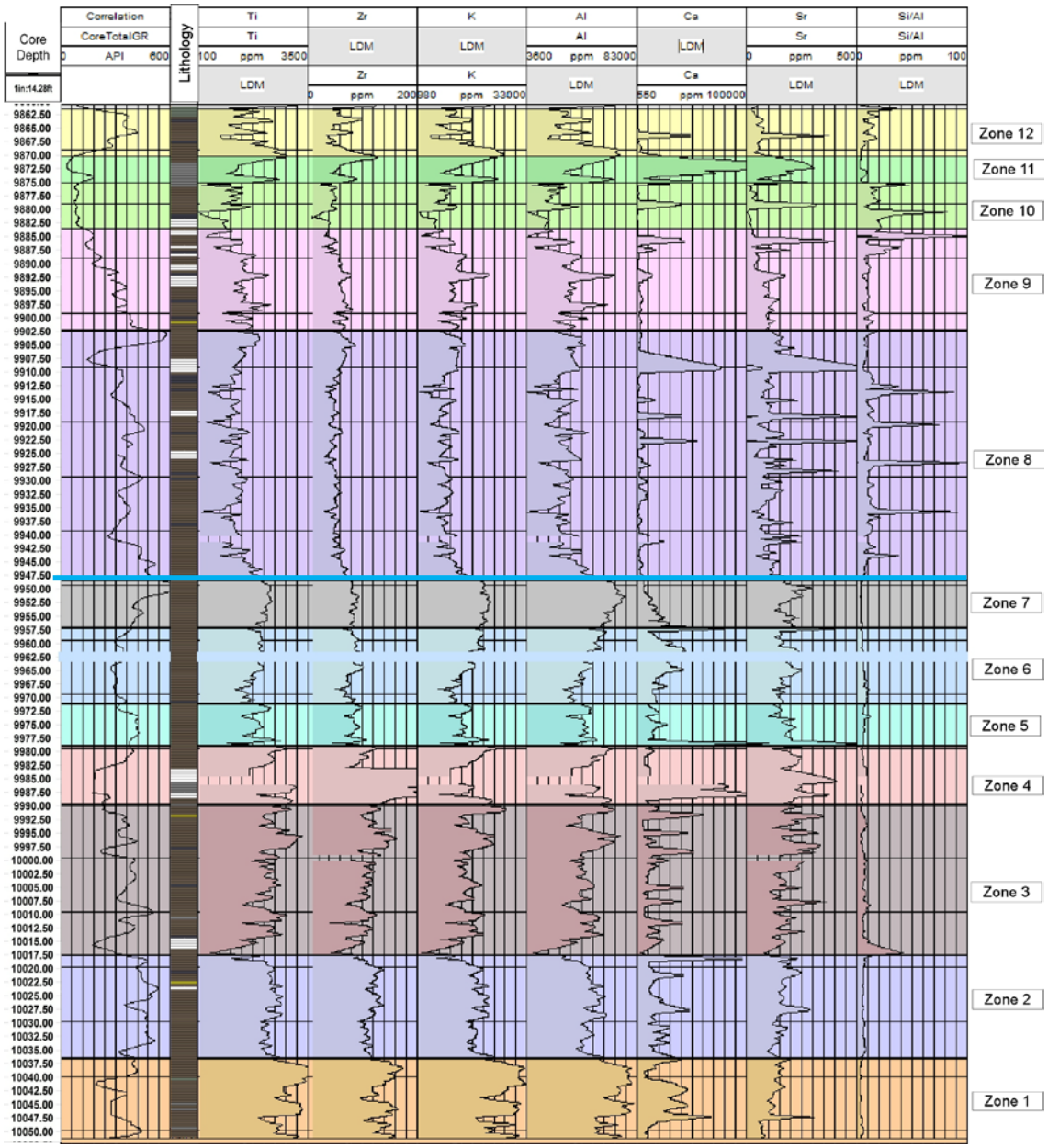

Figure 16. Core D with the 12 zones applied to the lithology and geochemical proxies. The blue line is indicative of the interpreted FF boundary.

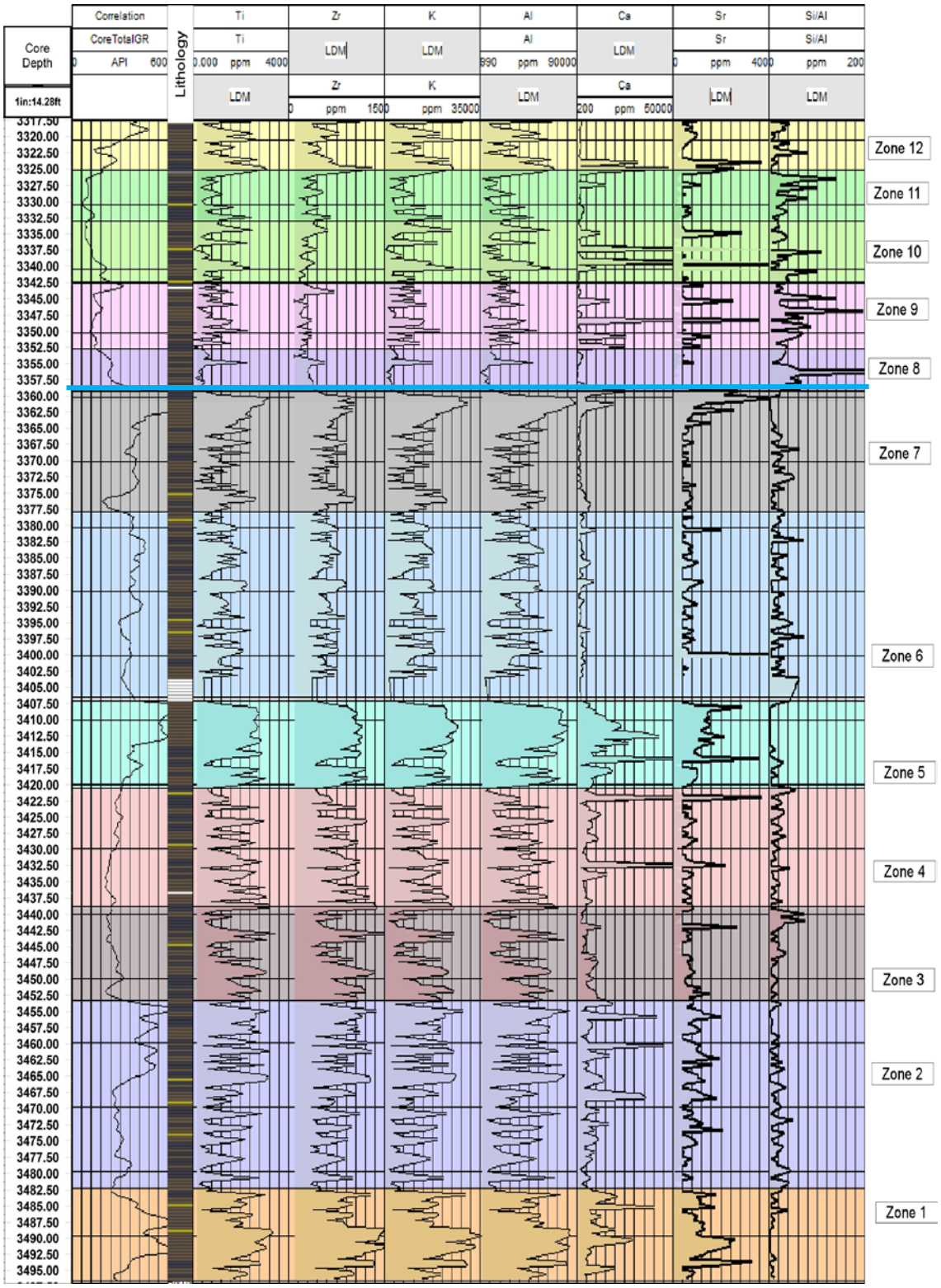

Figure 17. Core E with the 12 applied with the lithology and geochemical proxies. The blue line is indicative of the interpreted FF boundary.

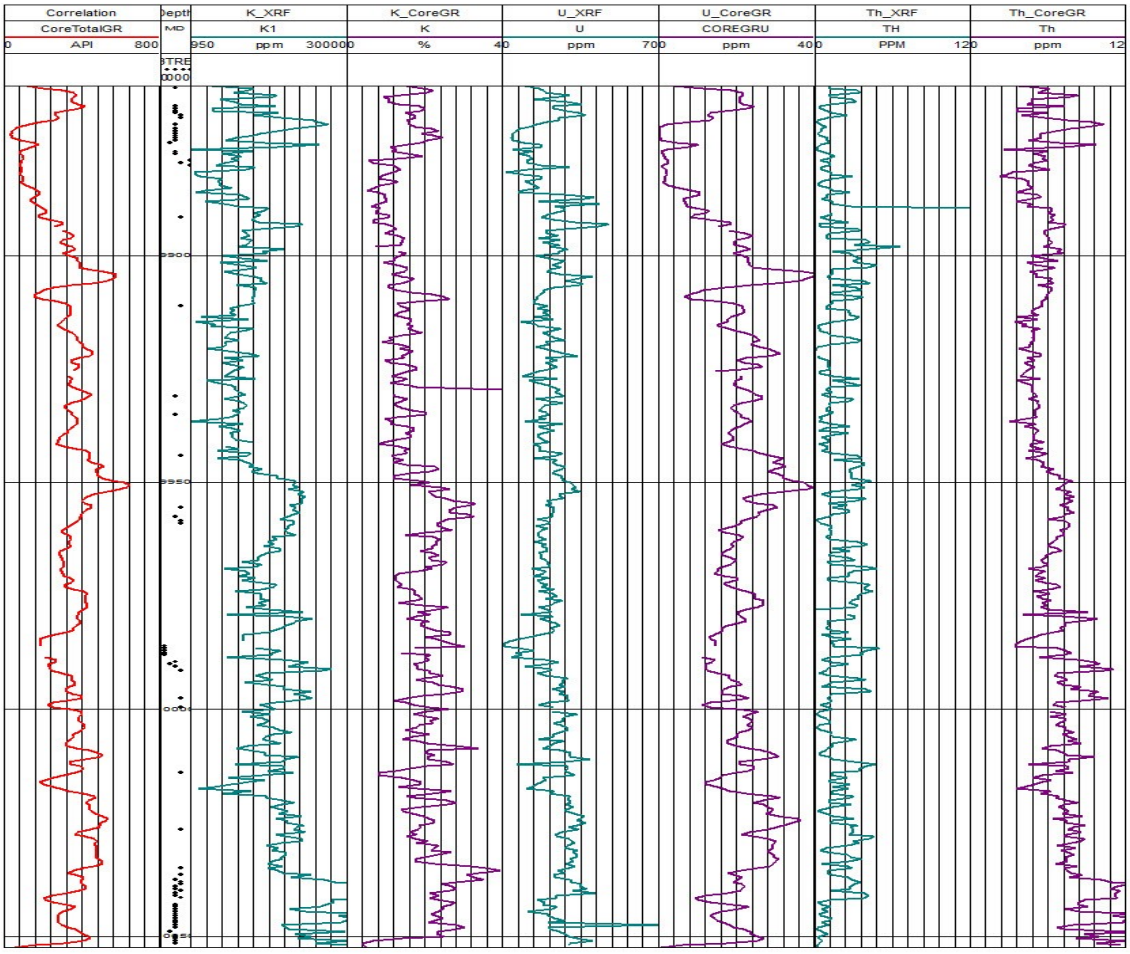

Figure 18. Comparison in core D between XRF raw element curves (blue-green) K, U, and Th, and core gamma-ray calculated (purple) K, U, and Th. Core gamma-ray is shown in red. This shows the validity of using the core calculated curves (purple) to create correlations with the XRF curves (blue-green) when XRF data is unavailable.

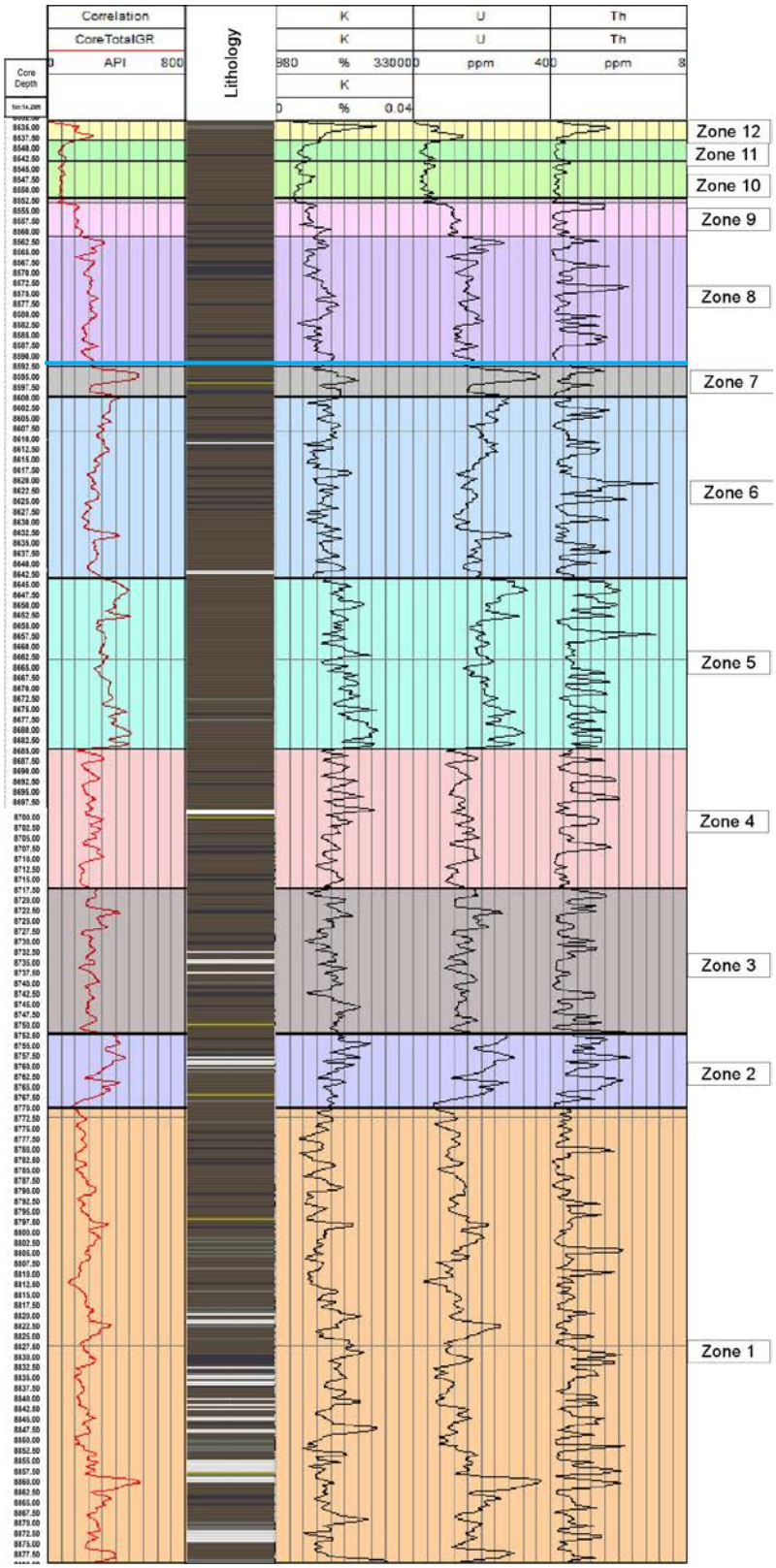

Figure 19. The 12 zones displayed with core A lithology and core gamma-ray calculated elemental curves. The blue line is indicative of the interpreted FF boundary.

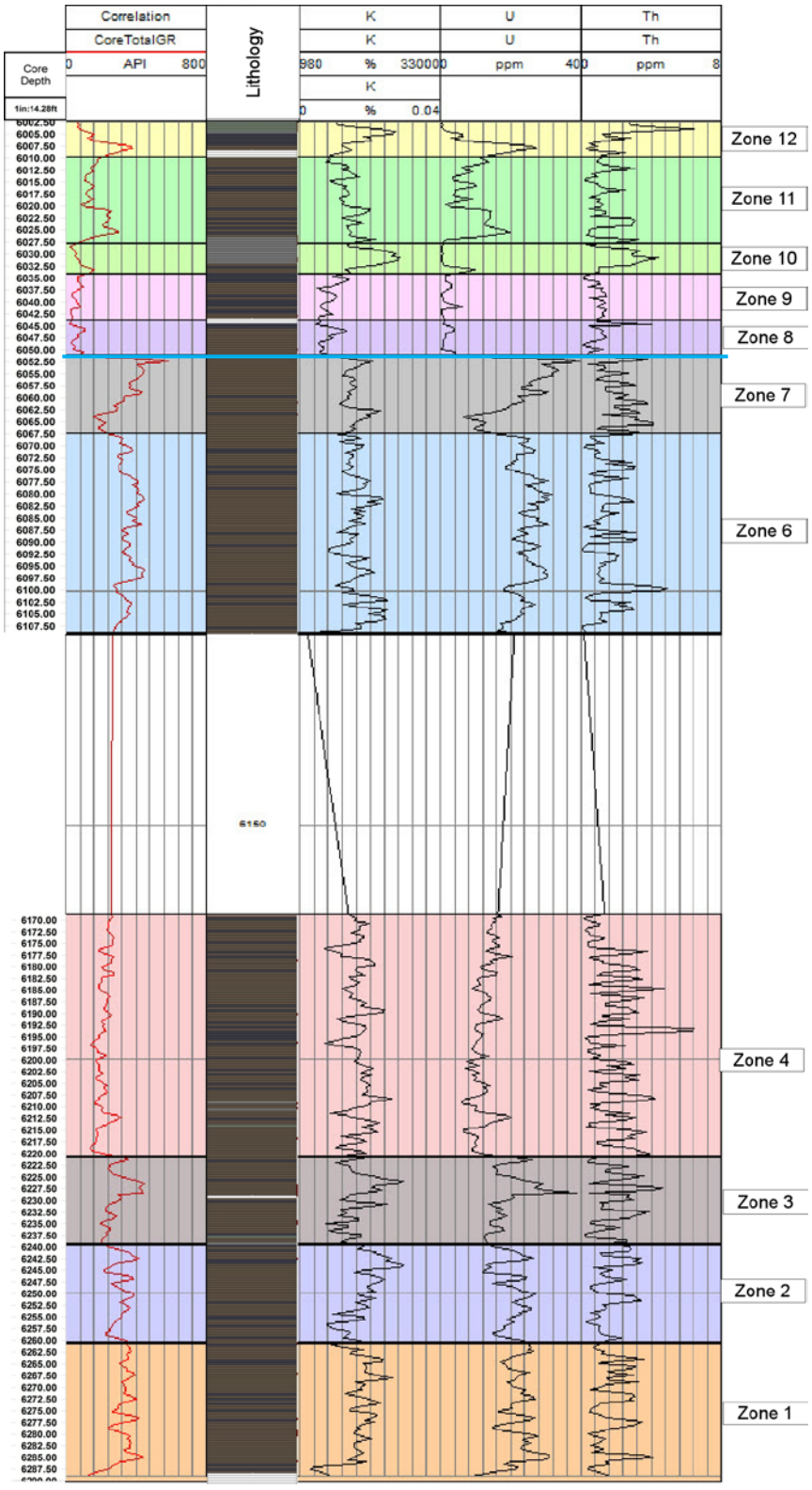

Figure 20. Zone data for core B with lithology and core gamma-ray calculated elemental curves. Note that Zone 5 was not identified in core B due to the 60-foot missing section of core. The blue line is indicative of the interpreted FF boundary.

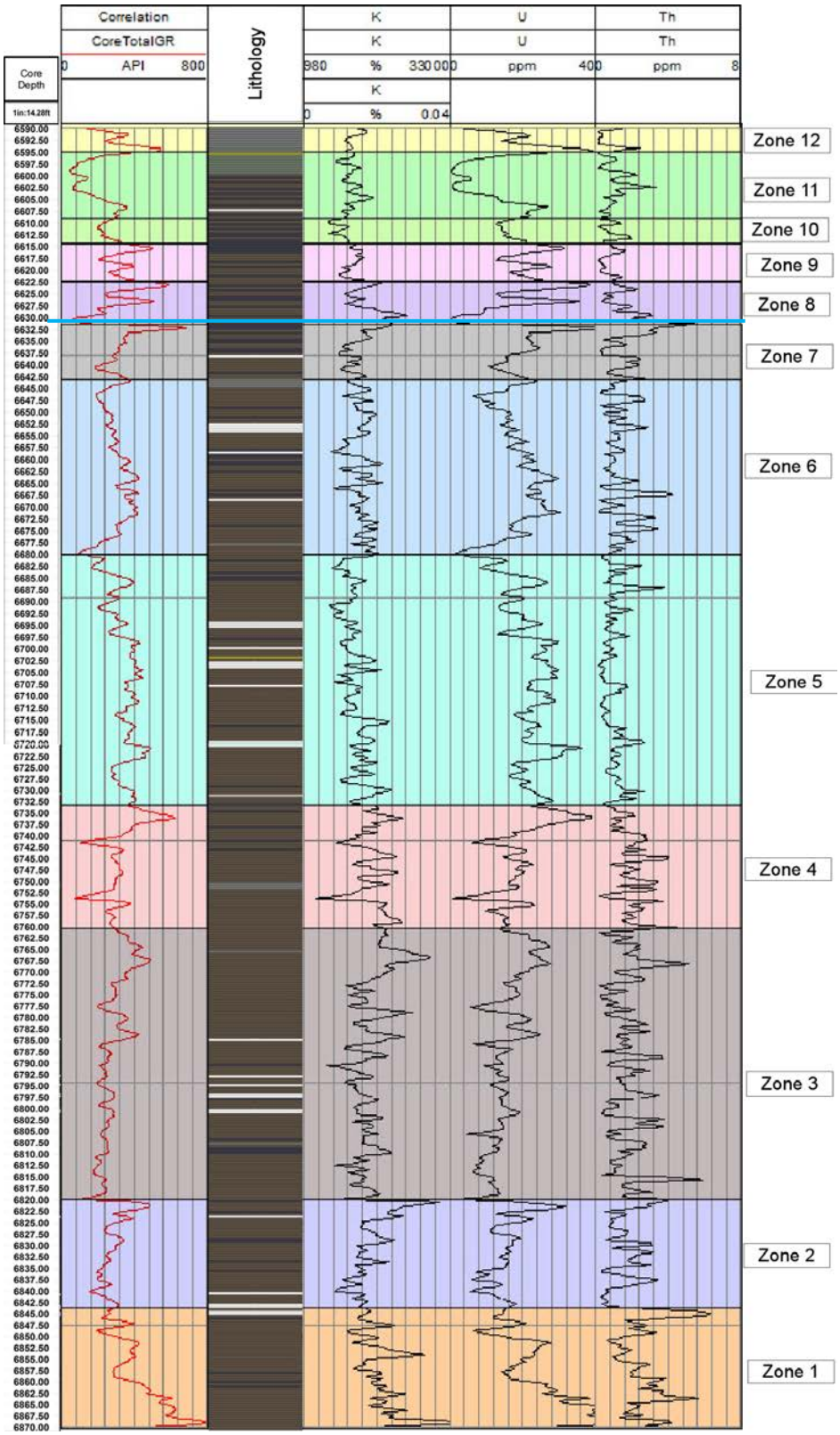

Figure 21. Zone data for core C with lithology and core gamma-ray calculated elemental curves. The blue line is indicative of the interpreted FF boundary.

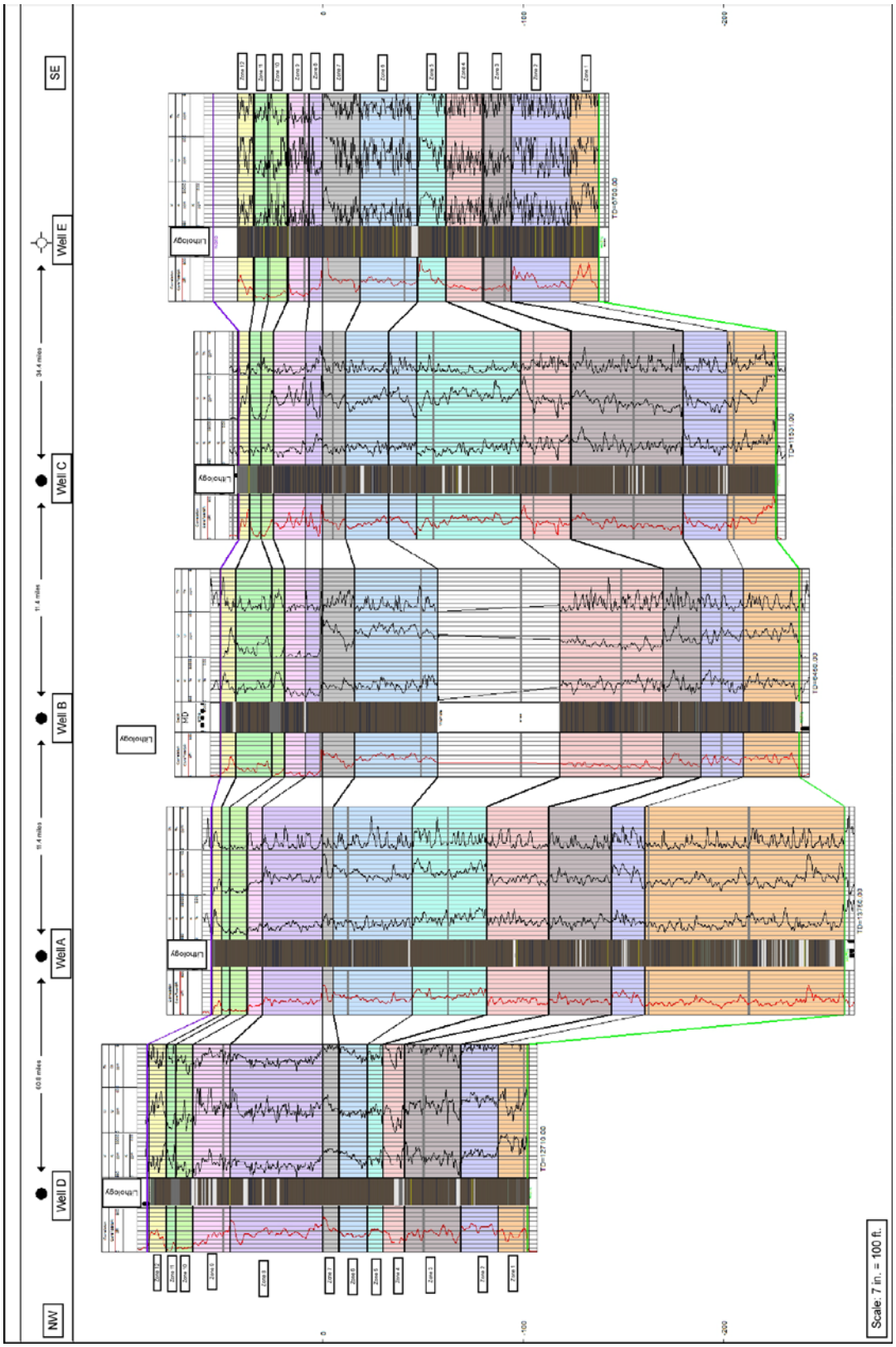

Figure 22. Chemostratigraphic correlation of all 5 cores for the 12 stratigraphic zones originally identified in core D and core E. Section is hung on the maximum flooding surface (MFS) which correlates to the top of zone seven.

4.1 CHEMOSTRATIGRAPHY

4.1.1 Core D

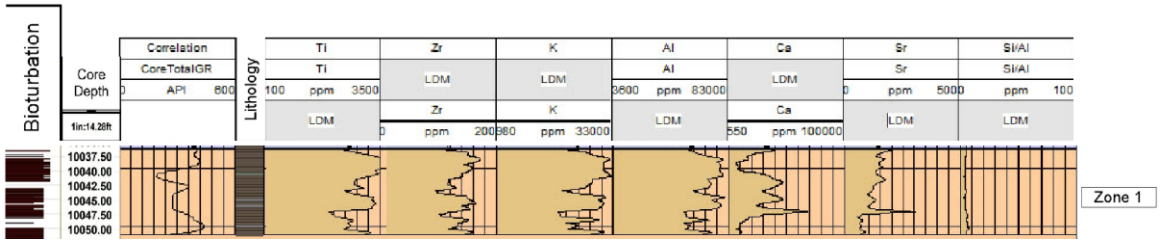

Figure 23. Zone one of core D

Zone one (Figure 23) displays an increase in detrital geochemical proxies, Ti, Zr, K, and Al, as well as high areas of carbonate geochemical proxies which can be explained by the increased bioturbation in this zone. The lithology shows alternating beds of FM1 and FM2 with local beds of FM3 and FM4. The Si/Al ratio in this zone is low. The lower order sequence stratigraphy of this zone is regression with local shifts in sedimentation present in both the chemostratigraphy as well as the gamma-ray profile (GRP).

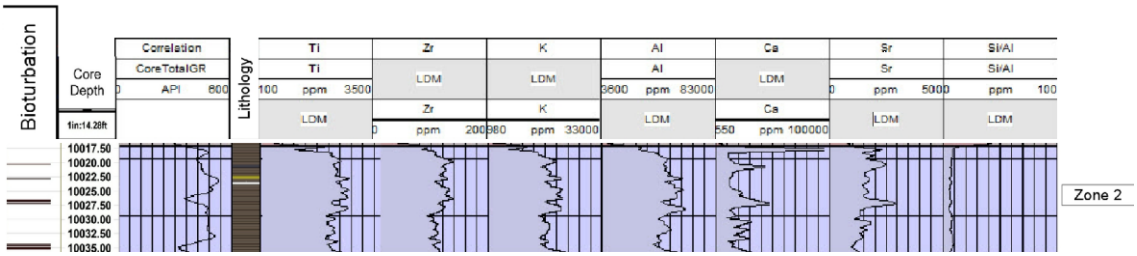

Figure 24. Zone two of core D.

Zone two (Figure 24) displays a lower order sequence stratigraphy of constant GRP with two higher order cycles of regression and transgression from the base upsection. The primary lithology of zone two is FM1 interbedded with FM2, and there is a thick pyrite bed located at 10,022.50 feet. The detrital geochemical proxies are decreased from zone one with cycles of increase and decrease that show positive covariance with local shifts in sedimentation in correlation with the GRP. The occasional peaks in carbonate geochemical proxies, Ca and Sr, correlate with the bioturbation noted

at 10,027.50 feet and 10,020.00 feet and with declines in the detrital geochemical proxies. The section does not display any peaks in the Si/Al ratio.

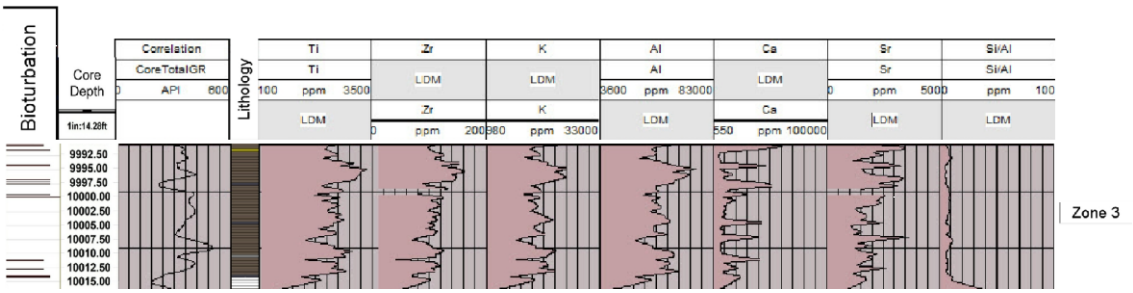

Figure 25. Zone three of core D.

Zone three (Figure 25) shows a transgressive sequence at the base with a regression starting at 10,008.50 feet and continuing to the top of the section. The primary lithology of zone three is FM1 interbedded with FM2 with a bed of FM4 located toward the base of the zone. There is a thicker pyrite bed located at the top of the section. The detrital elemental proxies show a steep decline at the base and overall increase upsection with higher order cycles correlating with the local changes of the GRP which are indicative of local changes in sedimentation. The carbonate geochemical proxies show local peaks throughout the section that correlate with dips in the detrital elemental proxies. A peak in the Si/Al curve at the base indicates a possible algal bloom and correlates with a local flooding surface and a chert bed.

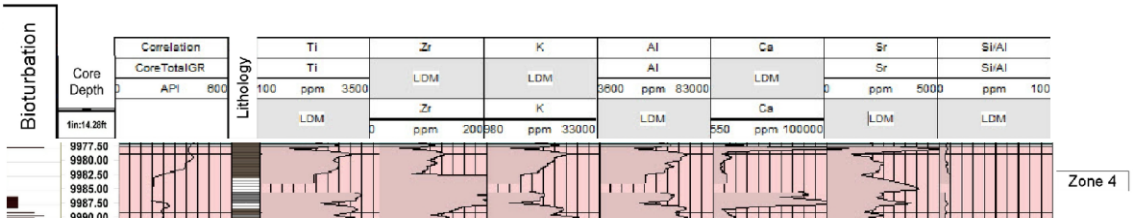

Figure 26. Zone four of core D

Zone four (Figure 26) displays no peaks in the Si/Al curve and has poorly preserved core throughout the section. This section is primarily FM4 at the base and FM 1 at the top. The GRP indicates a regression continued from zone 3 followed by a

transgression. The detrital geochemical proxies increase and decrease in zone four correlate with the GRP cycles of changes in sedimentatio. The carbonate proxies increase and decrease opposite of detrital proxies. Calcium and Sr show negative covariance with each other at 9,980 feet where the Sr shows and increase and Ca stays low. This is likely due to Sr replacement of Ca in aragonite at this location. The heaviest bioturbation in this zone occurs in the FM4 facies near the base of the zone and correlates with increases in the carbonate geochemical proxies.

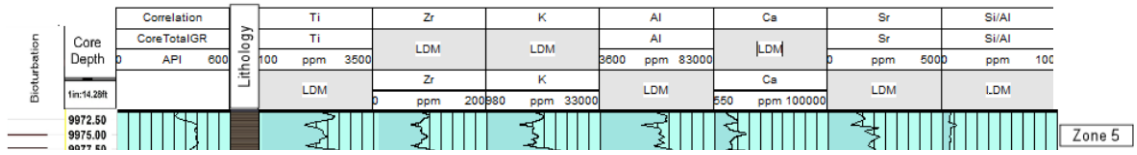

Figure 27. Zone five of core D

Zone five (Figure 27) is a condensed section. The zone is capped by a regressive GRP. The primary lithology of zone five is FM1 with only local beds of FM2. Detrital proxies are generally constant through the zone with increases and decreases likely corresponding to sedimentation events. Peaks in carbonate depositional proxies have a positive correlation with noted bioturbation in zone five. There are no significant Si/Al peaks in zone five of core D.

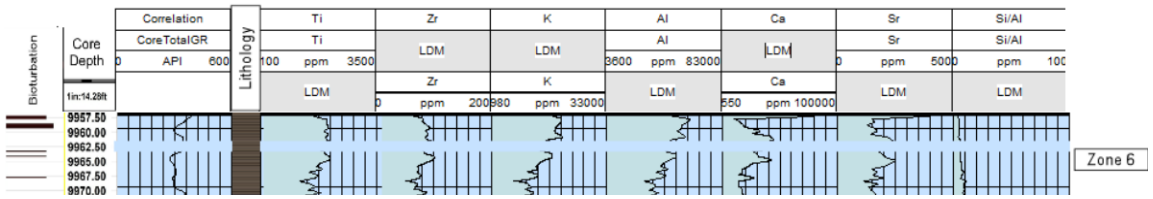

Figure 28. Zone six of core D.

Zone six (Figure 28) is a transgressive zone in the GRP that has positive correlation with the detrital elemental proxies. The detrital elemental proxies increase upward in this zone. Changes in carbonate geochemical proxies correlate with noted bioturbation. The transgressive cycle indicates a rise in sea level, however, the detrital proxies and the lithology indicate that the dominant sediment is clay since the K and Al are higher and, at times, show an inverse relationship to Ti and Zr. Zone six is primarily made up of FM1 with local beds of FM2. Zone six shows no peaks in the Si/Al curve.

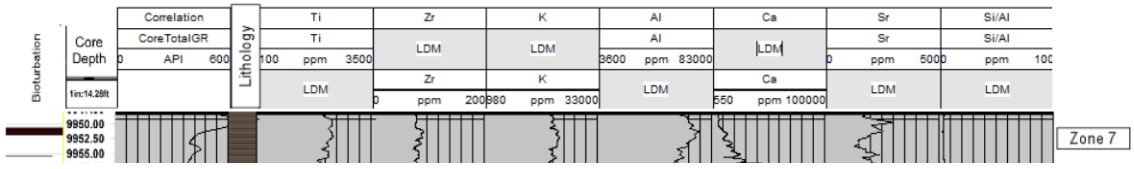

Figure 29. Zone seven of core D.

Zone seven (Figure 29) is a single transgression with the top of the section being the regional maximum flooding surface previously mentioned. The entire zone is FM1 with bioturbation noted at the top of the zone which correlates with a gradual dip in detrital proxies and a spike is Sr. The detrital geochemical proxies are steadily increasing though the section until they dip at the very top while the Ca decrease through the zone. There are no Si/Al peaks in zone seven.

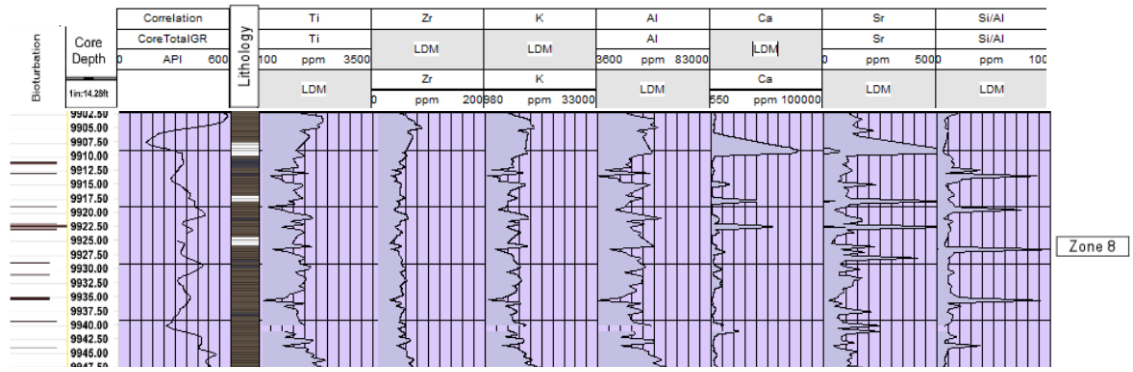

Figure 30. Zone eight of core D.

Zone eight (Figure 30) is a gradual regressive zone that shows high variation in sedimentation and an interpreted transgression at the top of the zone in the GRP that has a poor positive correlation with the detrital elemental proxies. The detrital elemental proxies are lower in this zone than they have been in any of the previous zones, but show areas of sharp decrease that correlate with sharp increases in carbonate geochemical proxies and noted bioturbation. The detrital proxies and the lithology indicate that the dominant sediment is clay since the K and Al are higher and, at times, show an inverse relationship to Ti and Zr. Zone six is primarily made up of FM1 with local beds of FM2. Zone eight shows several peaks in the Si/Al curve that correlate with chemostratigraphic flooding surfaces and are likely algal blooms.

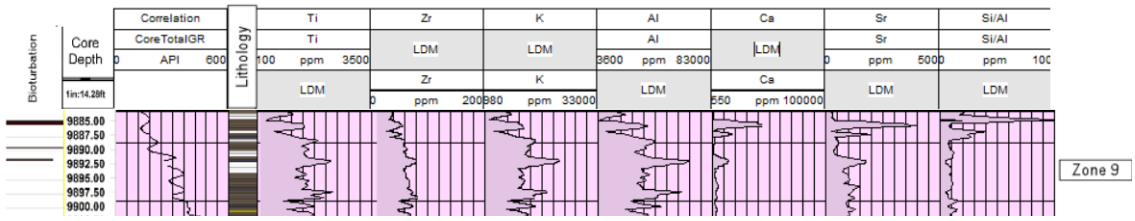

Figure 31. Zone nine of core D.

Zone nine (Figure 31) is a regression from the interpreted transgression at the top of zone eight and has a steady decrease in detrital with an increase upsection of carbonate proxies. The zone is topped by an increase in the Si/Al curve indicating an algal bloom. Bioturbation correlates with the peaks in carbonate proxies approximately halfway up the

zone. Zone nine is primarily FM1 with local beds of FM2 and many sections of poorly preserved core.

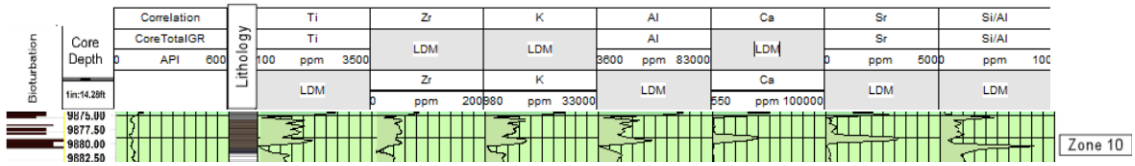

Figure 32. Zone ten of core D.

Zone ten (Figure 32) is characterized by a constant gamma-ray profile and gradual increase in detrital geochemical proxies. The peak in carbonate proxies in the middle of the zone correlates with identified bioturbation. The Si/Al curve is increased through the section with a spike in the middle of the section that correlates with a chert bed (FM2), and at the top of the section that correlates with a chemostratigraphic flooding surface and is interpreted to be an algal bloom. Zone ten is primarily made up of FM1 laminated to interbedded with FM2. A bed of FM4 caps zone ten.

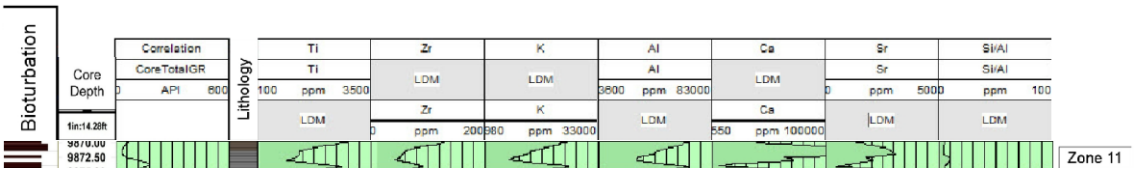

Figure 33. Zone eleven of core D.

Zone eleven (Figure 33) shows and interpreted regression at the base followed upward by an interpreted transgression in the GRP. The detrital geochemical proxies also show a brief increase at the base followed by a decrease. The detrital proxies begin to increase near the top of the zone. The carbonate element proxies increase through the section and correlate with noted bioturbation. There is no significant Si/Al peak in zone eleven. Gray silty mudstone (FM4) is the primary lithology of zone eleven, but it is capped by FM1.

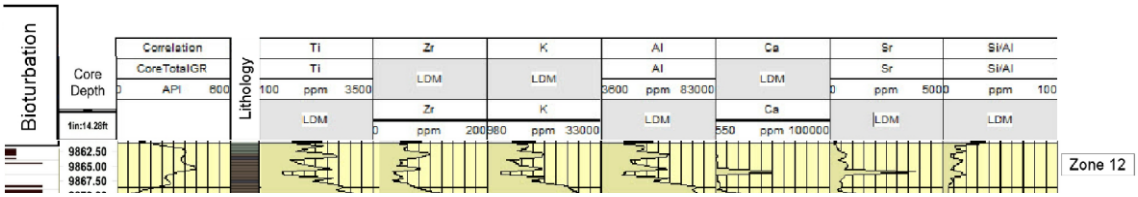

Figure 34. Zone twelve of core D.

Zone twelve (Figure 34) is characterized by a transgression with slightly elevated Si/Al curve but no significant peaks. There is a peak in Ca and Sr where there is a drop in detrital elemental proxies that indicate an influx of carbonate material, there was no noted bioturbation at this point. Zone twelve is FM1 interbedded with FM2 at the base and capped by FM3.

4.1.2 Core E

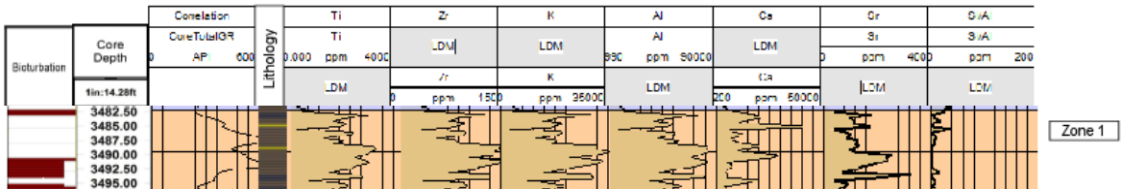

Figure 35. Zone one of core E.

Zone one (Figure 35) is characterized by a regressive GRP and is predominantly interbedded FM2 with FM1 which is reflected by the continuous peaks and troughs of the geochemical proxies through the section. Near the base of the zone where there is a higher portion of FM1 the detrital proxies are higher and peaks in carbonate proxies correlate with noted bioturbation in the zone. Si/Al peaks correlate with radiolarian in the chert beds (FM2).

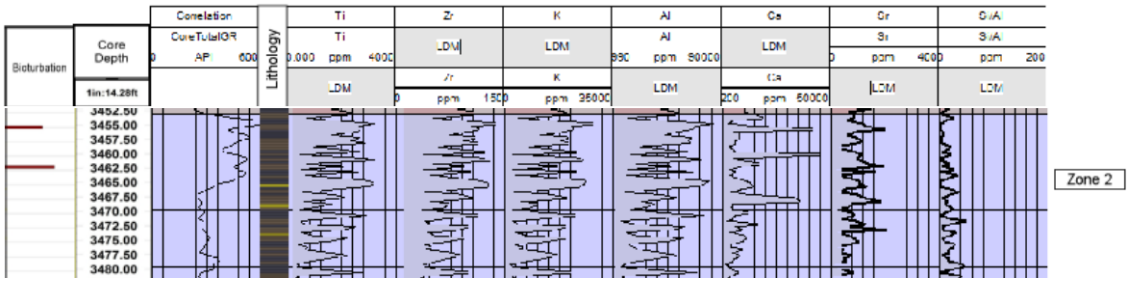

Figure 36. Zone two of core E.

Zone two (Figure 36) shows a transgressive GRP and very little bioturbation is noted, however the bioturbation that is noted correlates with peaks in the carbonate geochemical proxies, Ca and Sr. The detrital elemental proxies gradually decrease through zone two but still show sharp shifts from high to low that correlate with FM1 and FM2 facies, respectively. Si/Al correlate with thicker beds of chert (FM2).

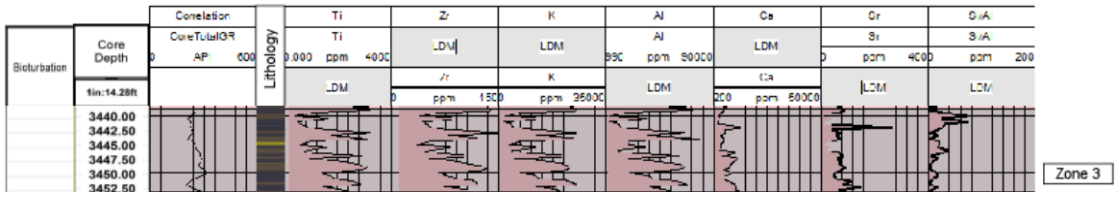

Figure 37. Zone three of core E.

Zone three (Figure 37) is characterized by a regression followed by a constant gamma-ray profile. The detrital proxies gradually decrease through the zone but continue to shift sharply in conjunction with changes in lithology. Zone three of core E is primarily FM2 with FM1 interbedded. The peak in the Si/Al curve correlated to a thicker bed of chert and is associated with an algal bloom.

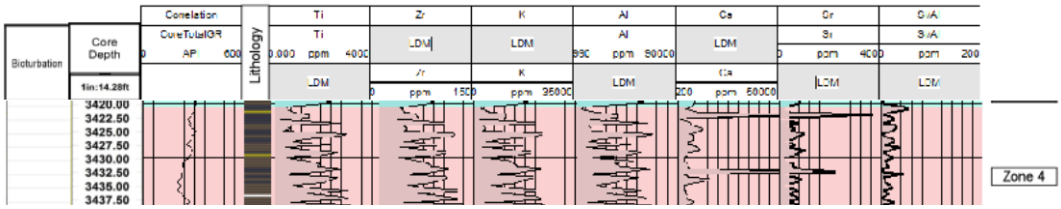

Figure 38. Zone four of core E.

Zone four (Figure 38) is characterized by a transgression and continues to show sharp shifts in detrital geochemical proxies that correlate with changes in lithology from FM1 (higher detrital proxies) to FM2 (lower detrital proxies). The Si/Al curves peak at the top of zone 4 correlates with a dip in detrital elemental proxies and with the FM2 that caps the zone. No bioturbation is noted in zone four of core E.

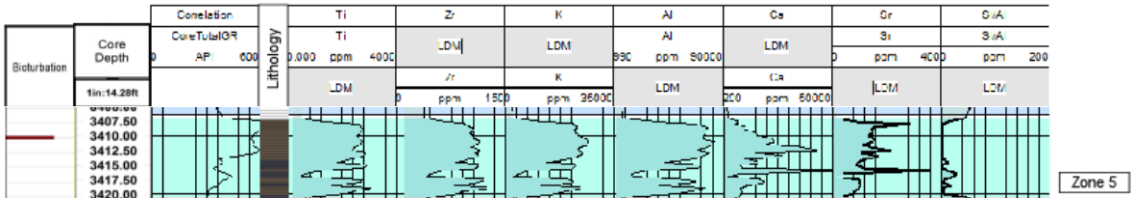

Figure 39. Zone five of core E.

Zone five (Figure 39) displays a transgressive GRP and has some of the highest amounts of the detrital geochemical proxies in the core. The dip in detrital element proxies correlates with a peak in carbonate element proxies and a siliceous mudstone (FM1) bed, however, there is no observed bioturbation here. There is some bioturbation noted near the top of the zone that correlates with increased carbonate proxies as well. There are no significant Si/Al peaks in zone five.

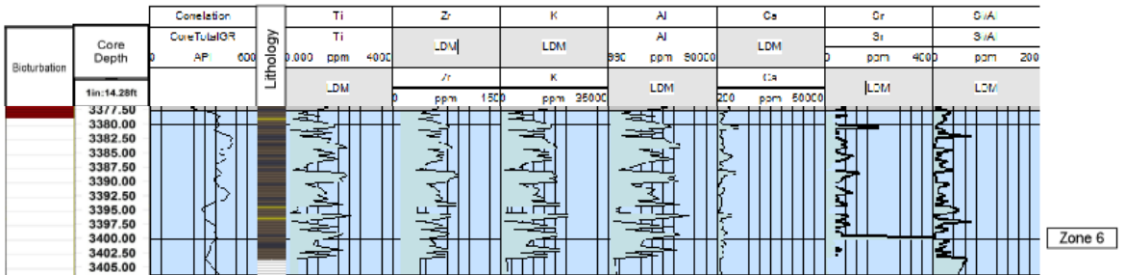

Figure 40. Zone six of core E.

Zone six (Figure 40) is a regressive GRP at the base followed by a transgressive GRP to the top of the zone. The overall amount of detrital elemental proxies is lower than lower in the section in the core but continues to display sharp shifts from low to high that correlates with shifts in lithology from FM2 to FM1, respectively. There are no significant peaks in carbonate geochemical proxies or in the Si/Al curve in zone six.

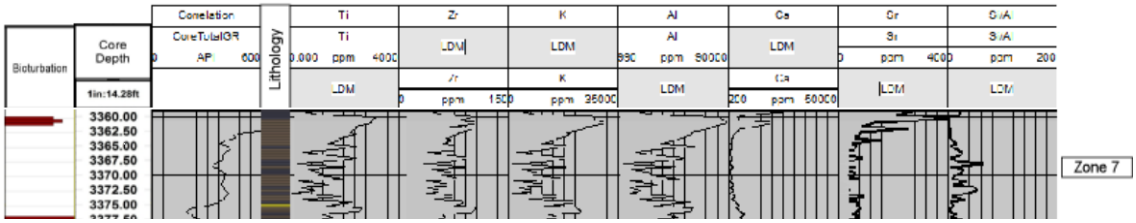

Figure 41. Zone seven of core E.

Zone seven (Figure 41) is capped by the regional maximum flooding surface. This zone exhibits a brief regression at the base followed by a transgression to the top of the zone. The detrital element proxies increase upsection. Zone seven decreases in FM2 upsection and is predominantly FM1. The calcium and strontium peaks correlate with identified bioturbation at the top of the zone. There are no significant Si/Al peaks, but the small peaks that are present correlate with the chert facies.

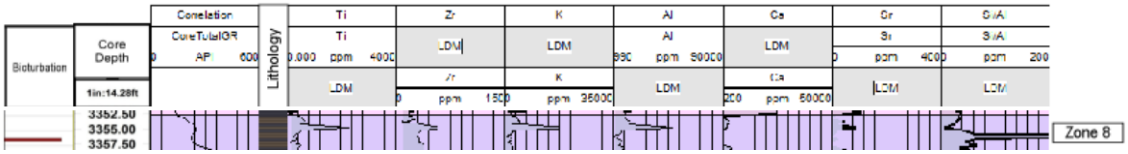

Figure 42. Zone eight of core E.

Zone eight (Figure 42) is characterized by a regression and all elemental proxies are suppressed at the base of the core except for the Si/Al curve which is elevated. There is a small peak in detrital proxies and a dip in the Si/Al curve that is associated with identified bioturbation near the top of zone eight. This zone is predominantly FM2 with FM1 interbedded.

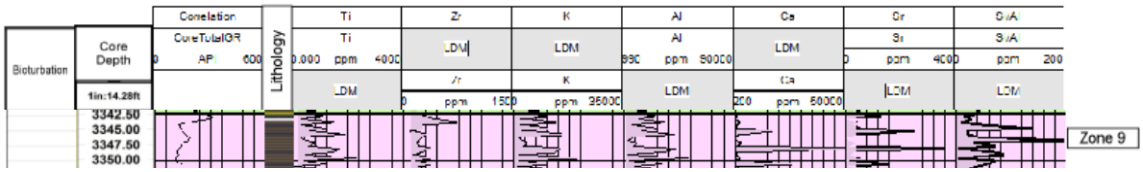

Figure 43. Zone nine of core E.

Zone nine (Figure 43) shows a small transgression with an increase in detrital geochemical proxies upsection, and peaks in the carbonate proxies through the zone. The Si/Al curve is elevated through the zone with peaks that correlate with FM2 facies and lows that correlate with peaks in the carbonate elemental proxies. This zone appears to be predominantly algal deposits which correlations to the predominant chert facies of this zone.

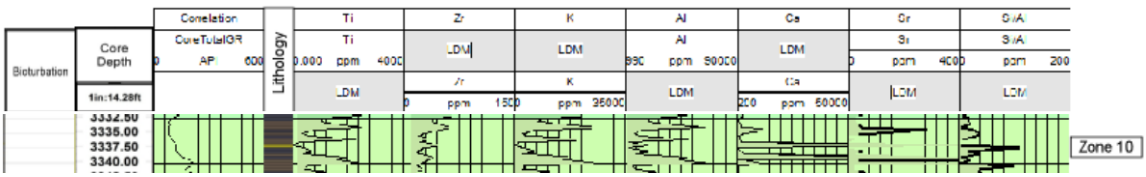

Figure 44. Zone ten of core E.

Zone ten (Figure 44) is characterized by a regressive GRP and a decrease in detrital element proxies. There is no noted bioturbation in zone ten of core E. This zone

is FM1 interbedded with FM2. The detrital elemental proxies show a sharp decrease at beds of FM2 that also correlates with peaks in the carbonate geochemical proxies and peaks in the Si/Al curve indicating radiolarian chert.

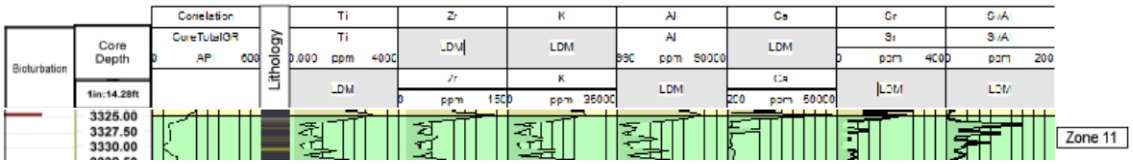

Figure 45. Zone eleven of core E.

Zone eleven (Figure 45) is a section of constant gamma-ray profile with detrital proxies decreasing upsetion and the Si/Al curve increasing upsection. These changes in geochemical proxies correlate to the changes in lithology upsection. There is no noted bioturbation in zone eleven of core E.

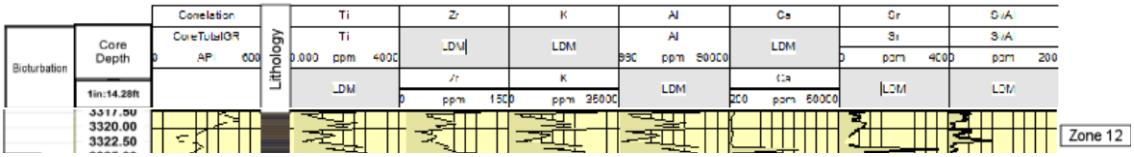

Figure 46. Zone twelve of core E.

Zone twelve (Figure 46) is characterized by a transgressive GRP with FM1 facies increasing upsection and a bed of FM4 at the base of the zone that correlates with high detrital proxies and an area of bioturbation near the base of zone twelve correlates with a peak in Ca and Sr. The Si/Al curve continues to correlate with FM2 beds.

4.2 BOTTOM WATER CONDITIONS

Molybdenum, V, Fe/S, bioturbation, TOC – and its geochemical proxy Ni (nickel) – were all used to interpret the bottom water conditions for core D and core E. Zones identified from chemostratigraphic correlations are used in the interpretation of bottom water condition as placement markers for simplicity purposes.

4.2.1 Core D

Zone one displays bioturbation, increasing TOC, cycles of peaks and troughs in Mo and V with a strong P peak near the base and a slight increase in P in the middle. This slight increase in P in the middle of zone one could explain the peak in Mo that is not present in V. This peak in Mo could also be due to the more suboxic bottom water conditions as Mo is locked down at higher levels of oxygen than V. Pyrite production is low through zone one. The overall bottom water conditions would indicate a change from suboxic at the base to a small section of anoxic and back to suboxic bottom water conditions to the top of the zone.

Zone two and three show little bioturbation with increased TOC decreasing towards the top of zone three. Molybdenum decreases upsection while V is low throughout both zones. There is a dip in P at the base of zone three that correlates with a dip in Mo indicating that P might be impacting Mo concentrations, however the lower value of pyrite at this location suggest a possible influx of oxygen here. Zone two and three indicate alternations between suboxic and anoxic bottom water conditions as V is very low but Mo can sometimes peak; Mo is locked down in suboxic conditions.

Zone four has increased bioturbation, decreased TOC, decrease Mo and V despite the presence of a P peak; zone 4 indicates oxic bottom water conditions at the base and suboxic bottom water conditions upsection. Zone five and zone six show relatively little bioturbation with a corresponding change, although slight, in TOC where bioturbation is noted. There is little change in Mo, V, or P in these zones. Zone five and six show a continuation of the suboxic conditions from zone four.

Zone seven shows a sharp decrease followed by an increase in TOC; this decrease corresponds to bioturbation. There is an upward increase in Mo and V. Zone seven indicates suboxic bottom water conditions moving into anoxic bottom water conditions upsection.

Zone eight shows an increase in TOC while Mo, V, and P stay relatively low and the pyrite production is also increased. Zone eight shows a continuation of the anoxic conditions from the top of zone seven and then moves into interpreted suboxic conditions with a corresponding decrease in TOC. There is what appears to be an influx of oxygen toward to the top of the zone. Zone eight is capped by a zone of interpreted anoxic bottom water conditions.

Zone nine has some indicated bioturbation, shows a slight decrease in TOC, and very low Mo at the top. However, the V readings are very high at the top which could be due to the high amount of P at the top of the zone. Molybdenum, bioturbation and low pyrite production in the upper portion of zone nine would indicate increasing oxygen. The interpreted anoxia from zone eight continues up into zone nine. Approximately halfway up the zone oxygen increases and bottom water conditions are interpreted as suboxic, which is continued through zone ten as Mo and TOC continue to decrease while bioturbation increases and pyrite stays low.

Zone eleven shows almost no Mo, Ni, V, or Pyrite. The bioturbation is high in zone eleven and it is interpreted to have had oxic bottom water conditions at the time of deposition.

Zone twelve has some noted bioturbation at the base and the very top with increase TOC. Zone twelve has a sharp increase in Mo and V with a decrease in P; this

indicates that zone twelve had suboxic to anoxic bottom water conditions. Figure 47 shows bottom water indicators for Core D.

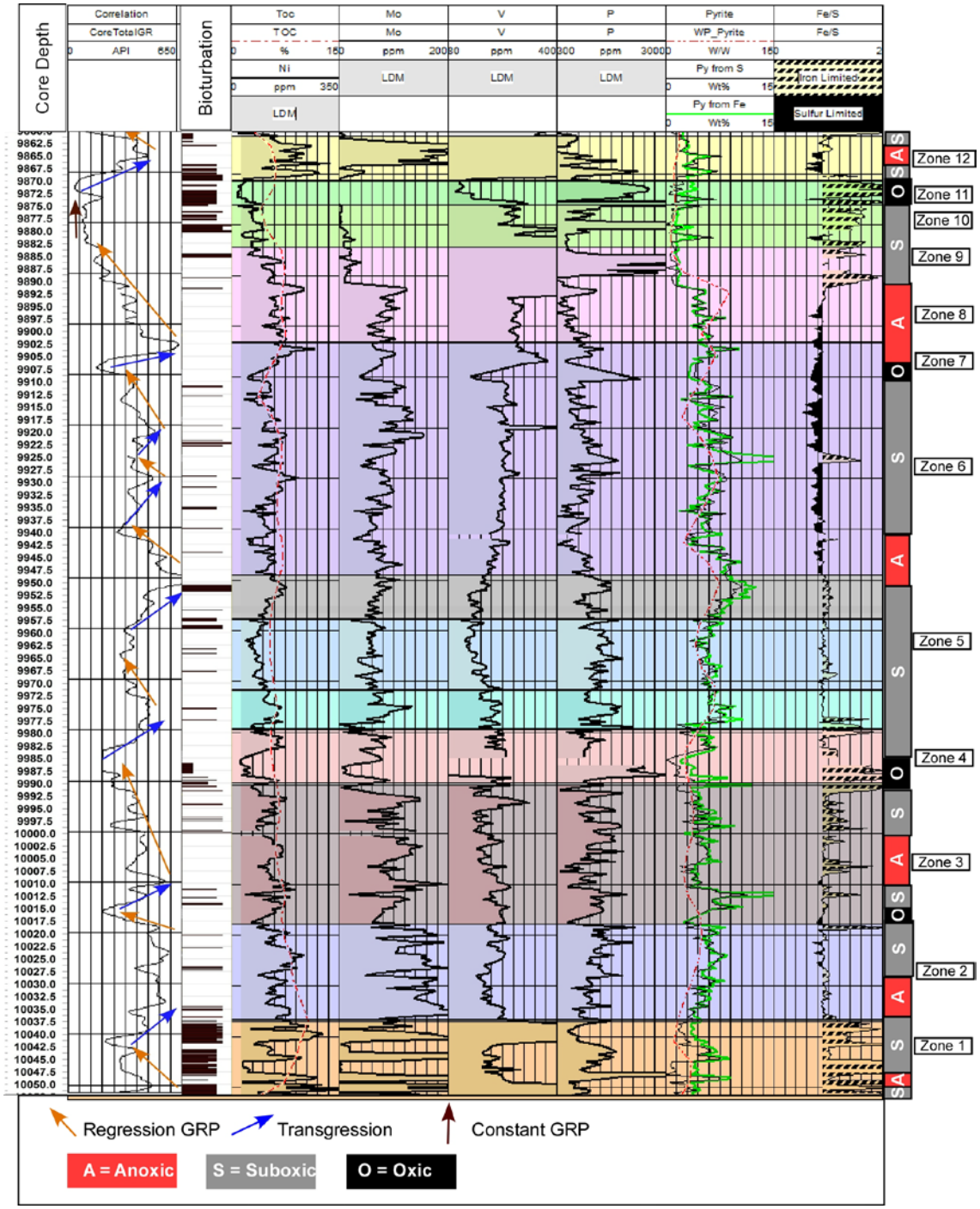

Figure 47. Bottom water conditions for core D with zones indicated.

4.2.2 Core E

Zone one shows bioturbation with cycles of peaks and troughs in both Mo and V with relatively low P, TOC, and pyrite; zone one is interpreted to have had suboxic at the base oxic bottom water conditions at the top at the time of deposition.

Zone two indicates a return to suboxic bottom water conditions from zone one with continued low V, low pyrite values and high Mo values without corresponding peaks in P. The low TOC could be attributed to a lack of organic matter input during this time.

Zone three indicates that bottom water conditions were likely anoxic with an influx of oxic bottom waters at the top with decreasing Mo values and low V values and a peak in pyrite near the base of the zone. Zone three also shows a decrease in TOC that likely has less to do with bottom water oxygen conditions and more to do with a lack of organic material input during deposition.

Zone four shows a continued low TOC, moderate Mo values and low V values indicating suboxic bottom water conditions. Zone five shows an increase in TOC with some bioturbation near the top. There is a sharp drop in Mo near the base that corresponds with a dip of equal magnitude in P indicating that the presence of P is likely retaining Mo although V values are low and indicating suboxic conditions continue from zone four.

Zone six shows a drop in TOC followed by a gradual increase in TOC. Molybdenum gradually increases through this zone while V stays constant and low with relatively stable P values. Pyrite production in zone six is also low indicating suboxic bottom water conditions.

Zone seven resembles zone 6 except for the peak in P at the very top corresponding to a decrease in TOC and bioturbation; zone 7 likely had suboxic bottom water conditions.

Zone eight and zone nine show decreasing Mo with cyclic V that corresponds to cyclic increases in P locally. Since V is high in intervals where P is not high and Mo is low, zone eight likely had suboxic bottom water conditions.

Zone ten shows a decrease in TOC, very low Mo, low V, and relatively low P with some higher peaks. The higher P peaks could possibly be what is keeping the V reading higher than Mo; this zone has indicated suboxic bottom water conditions. The low pyrite in zone ten and eleven likely has more to do with it being deposited in an iron limited environment and less to do with the bottom water conditions.

Zone eleven continues with low Mo, low pyrite, and low TOC. Elevations in V are tied to peaks in P. Zone eleven has interpreted oxic to suboxic bottom water conditions indicated.

Zone twelve shows decreasing TOC, high Mo and V with low P indicating a shift from suboxic to anoxic bottom water conditions. Figure 48 shows bottom water indicators for core E.

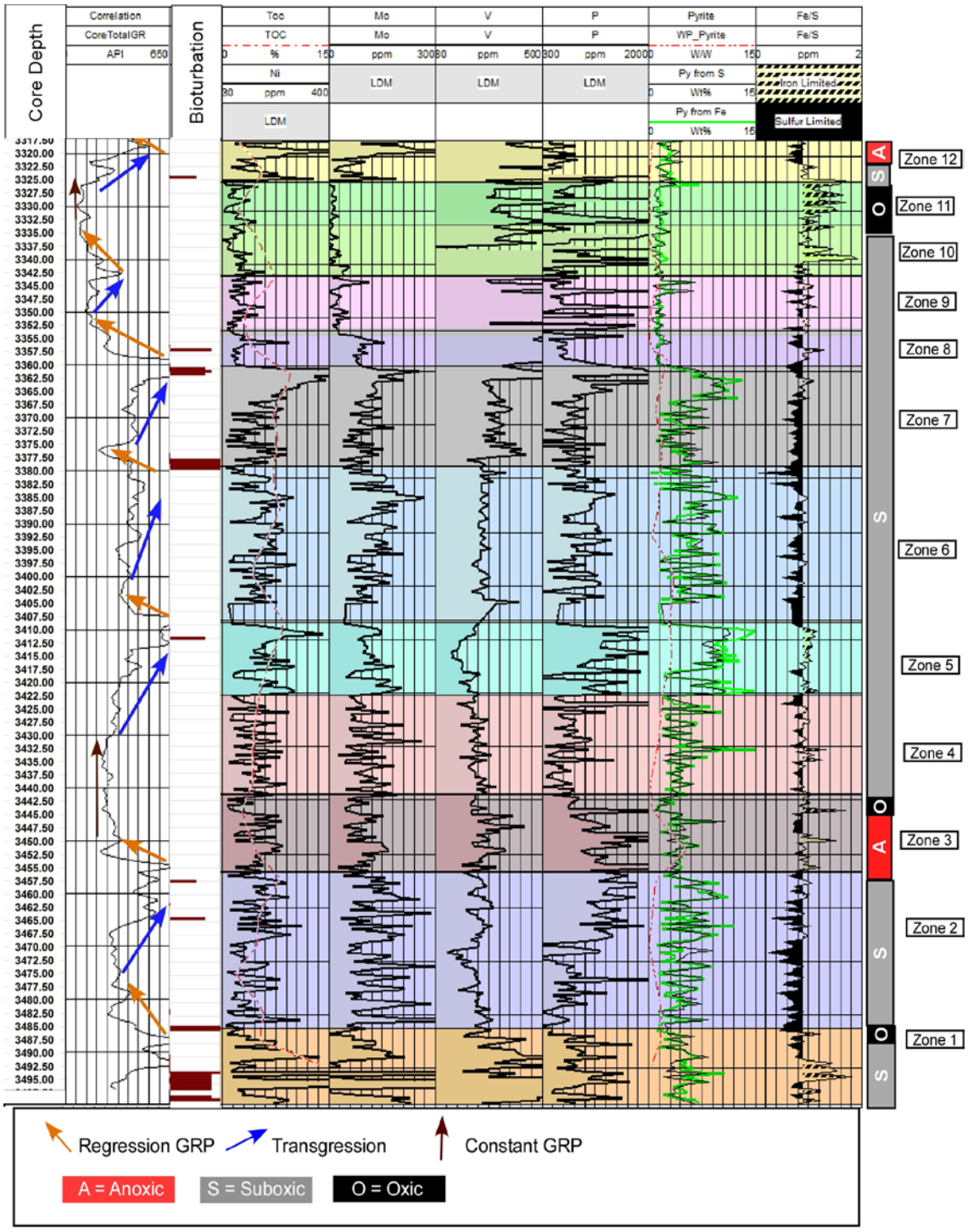

Figure 48. Bottom water conditions for core E with zone indicators.

5. CONCLUSION

The Woodford Shale formation is much more than a simple homogenous black shale that can be simply divided into three members. The Woodford Shale serves as both a source rock for multiple Mid-Continent gas and oil plays, but also as a reservoir rock. Thus, it is vitally important that we work to better understand this formation; this can be done through comprehensive reservoir characterization including, but not limited to, core descriptions, thin section analysis, petrophysical calculations, mineralogical data, and chemostratigraphic data.

The correlation to TOC was not what the expected results would be, a decrease in TOC was expected in areas of bioturbation. This could be due to the lack of abundance in bioturbation. Pervasive bioturbation toward the lower portion of core A correlates to the sharp decline in the TOC of core A (Figure 6) that is not present in the other cores. Although the bioturbation correlated with dips in Mo, V, and U in each core, it was not easily correlated from core to core. However, since bioturbation is localized and not pervasive in the depositional environment, correlation of the bioturbation in cores separated by great distance is not to be expected.

Chemostratigraphic correlations have enabled the identification of twelve different stratigraphic zones within the Woodford Shale. This thesis validates previous works (Tréanton, 2014; and Turner, 2016) showing the usefulness of chemostratigraphic data in providing a higher resolution understanding of the elemental changes within the Woodford Shale through the use of data collected from HH-XRF technology.

Through the use of gamma ray logs from core, and calculated elements – K, U, and Th – from those gamma-ray logs, the twelve zones identified with XRF data in core

D and core E were able to be correlated in cores A-C even though XRF data was not available for those cores (Figure 22). Coincidentally, spectral gamma-ray logs would give the same elemental curves that were calculated in the lab from the measured core gamma-ray – K, U, and Th – for cores A-C. This indicates a high potential for such correlations to extend throughout the basin with limited core and XRF data available.

Elemental data collected with HH-XRF technology can also provide important information on bottom water conditions at the time of deposition which is an important factor for industry when it comes to core placement. Both core D and core E showed a general anoxic environment but each core also showed possible zones of oxic bottom water conditions at the time of deposition based on the Mo and V curves coupled with the P curves.

REFERENCES

Algeo, T. J., and J. B. Maynard, 2004, Can marine anoxic events draw down the trace element inventory of seawater?: Geology, v. 32, p. 1057-1060.

Algeo, T. J., and Rowe H., 2012, Paleoceanographic applications of trace-metal concentration data: Chemical Geology, p. 6-18.

Althoff, C. D., 2012, Characterization of depositional megacycles in the Woodford trough of central Oklahoma: M.S. thesis, University of Oklahoma, Norman, Oklahoma, 170 p.

Angulo-Saldina, S., 2010, An integrated sedimentological, ichnological and sequence stratigraphic study in the Devonian-Carboniferous Bakken Formation of subsurface southeastern Saskatchewan: Doctoral thesis, The University of Saskatchewan (Canada), Ann Arbor, 150 p.

Amorocho, J. D., 2012, Sequence stratigraphy and seismic interpretation of the upper Devonian – lower Mississippian Woodford Shale in the Cherokee Platform: A characterization approach for unconventional resources: M.S. thesis, University of Oklahoma, Norman, Oklahoma, 109 p.

Badra, H., 2011, Field characterization and analog modeling of natural fractures in the Woodford Shale, southeast Oklahoma: M.S. thesis, University of Oklahoma, Norman, Oklahoma, 156 p.

Banner, J. L., 1995, Application of the trace element and isotope geochemistry of strontium and studies of carbonate diagenesis: Sedimentology, v. 42, p. 805-824.

Ben-Awuah, J., and Padmanabhan, E., 2014. Impact of bioturbation on reservoir quality: A case study of biogenically reduced permeability of reservoir sandstones of the Baram Delta, Sarawak, Malaysia. Journal of Applied Sciences, v. 14, p. 3312-3317

Bhatia, M. R., and Crook, K. A. W., 1986. Trace element characteristics of graywackes and tectonic setting discrimination of sedimentary basins: Contributions to Mineralogy and Petrology, v. 92, p. 181-193.

Chain, R. A., 2012, Stratigraphy and composition of the Woodford Shale in depositionally updip and downdip wells, Anadarko Basin, Oklahoma: M.S. thesis, University of Oklahoma, Norman, Oklahoma, 137 p.

Chipera, Steve J., and David L. Bish, 2002, FULLPAT: a full-pattern quantitative analysis program for X-ray powder diffraction using measured and calculated patterns. Journal of Applied Crystallography, v. 35.6, p. 744-749.

Gingras, M. K., G. S. Pemberton, and M. Smith, 2015, Bioturbation: reworking sediments for better or worse: Oilfield Review Winter 2014/2015, v. 26, p. 46-58.

Gupta, N., Sarkar, S., and Marfurt, K. J., 2011, Seismic characterization of the Woodford Shale in the Anadarko basin: SEG Technical Program Expanded Abstracts, v. 30, p. 1083-1087.

Hester, N. T., Sahl, H., and Schmoker, J., 1988, Cross sections based on gamma-ray density, and resistivity logs showing the stratigraphic units of the Woodford Shale, Anadarko basin, Oklahoma: United State Geological Survey Miscellaneous Field Studies Map 2054, p. 2 plates.

Johnson, J. G., Klapper, G., and Sandberg, C. A., 1985, Devonian eustatic fluctuations in Euramerica: Geological Society of America Bulletin, v. 96, p. 609-619.

Jordan, D. W., 1985, Trace fossils and depositional environments of Upper Devonian black shales, east-central Kentucky, U.S.A.: The Society of Economic Paleontologists and Mineralogists, sp. 35, p. 279-298.

Killian, B. J., 2012, Sequence stratigraphy of the Woodford Shale, Anadarko basin, Oklahoma: Implications on regional Woodford target correlation: M.S. thesis, University of Oklahoma, Norman, Oklahoma, 102 p.

Krystyniak, A. M., 2005, Outcrop-based gamma-ray characterization of the Woodford Shale of south-central Oklahoma: M.S. thesis, Oklahoma State University, Ann Arbor, 160-160 p. p.

Lambert, M. W., Lithology and geochemistry of shale members within the Devonian-Mississippian, Chattanooga (Woodford) Shale, Midcontinent, USA: Doctoral thesis, 238 p.

Loubser, M., and Verryn, S., 2008, Combining XRF and XRD analyses and sample preparation to solve mineralogical problems: South African Journal of Geology, v. 11, p. 229-238.

Mayorga, L. C., 2012, An integrated approach to characterize the middle member of the Woodford Shale at the McAlister Cemetary Quarry, Oklahoma, USA: B.S. Thesis, University of Oklahoma, Norman, Oklahoma, 21 p.

McIlroy, D., 2007, Lateral variability in shallow marine ichnofabrics: implications for the ichnofabric analysis method: Journal of the Geological Society, v. 164, p. 359-369.

Miceli-Romero, A. A., 2010, Geochemical characterization of the Woodford Shale, central and southeastern Oklahoma: M.S. thesis, University of Oklahoma, Norman, Oklahoma, 133 p.

Molinares, C., 2013, Stratigraphy and palynomorphs composition of the Woodford Shale in Wyche Farm Shale pit, Pontotoc County, Oklahoma: M.S. thesis, University of Oklahoma, Norman, Oklahoma, 90 p.

Myrow, P. M., 1990, A new graph for understanding colors of mudrocks and shales: Journal of Geological Education, v. 38, p. 16-20

Novek, J. M., 2015, Paleoredox geochemistry and bioturbation levels of exceptionally preserved early Cambrian Indian Springs biota, Poleta formation, Nevada, USA: M.S. thesis, University of Wisconsin-Milwaukee, 94 p.

O'Neal, D. L., 2015, Chemostratigraphic and depositional characterization of the Niobrara formation, Cemex Quarry, Lyons, Co: Master's thesis, Colorado School of Mines, Golden, 119 p.

Pearce, T. J., Besly, B. M., Wray, D. S., and Wright, D. K., 1999, Chemostratigraphy: a method to improve interwell correlation in barren sequences – a case study using onshore Duckmantian/Stephanian sequences (Wes Midlans, U.K.): Sedimentary Geology, v. 124, p. 197-220.

Pearce, T. J., Jarvis, I., 1992, Applications of geochemical data to modelling sediment dispersal patterns in distal turbidites: Late Quaternary of the Madeira Abyssal Plain: Journal of Sedimentary Petrology, v. 62, p. 1112-1129.

Portas, R., 2009, Characterization and origin of fracture patterns in the Woodford Shale in southeastern Oklahoma for application to exploration and development: M.S. thesis, University of Oklahoma, Norman, Oklahoma, 113 p.

Qi, Y., M. Wang, W. Zheng, and D. Li, 2012, Calcite cements in burrows and their influence on reservoir property of the Donghe sandstone, Tarim Basin, China: Journal of Earth Science, v. 23, p. 129-141.

Raiswell, R., Buckley, F., Berner, R. A., Anderson, T. F., 1988, Degree of pyritization of iron as a paleoenvironmental indicator of bottom-water oxygenation: Journal of Sedimentary Research, v. 58, p. 812-819.

Rowe, H., Hughes N., Robinson, K., 2012, The quantification and application of handheld energy-dispersive x-ray fluorescence (ED-XRF) in mudrock chemostratigraphy and geochemistry: Chemical Geology, p. 122-131.

Sageman, B. B., and Lyons, T. W., 2004, Geochemistry of fine-grained sediments and sedimentary rocks: *In*: Mackenzie, F., 2004, Sediments, diagenesis, and sedimentary rocks, Treatise on Geochemistry, vol. 7, p. 115-158.

Serna-Bernal, A., 2013, Geological characterization of the Woodford Shale McAlister Cemetery Quarry, Criner Hills, Ardmore Basin, Oklahoma: M.S. thesis, University of Oklahoma, Norman, Oklahoma, 141 p.

Sierra, R., 2011, Integrated geomechanics and geological characterization of the Devonian-Mississippian Woodford Shale: M.S. thesis, University of Oklahoma, Norman, Oklahoma, 110 p.

Simpson, M., 2015, A structural re-evaluation of the Ardmore Basin: AAPG Datapages, Search and Discovery Article #10795, 19 p.

Slatt, R. M., Philps, P. R., Abousleiman, Y., Singh P., Perez, R., Portas, R., Marfurt, K.J,, Madrid-Arroyo, S., O'Brien, N., Eslinger, E. V., and Baruch, E. T., 2012, Pore-to-regional-scale integrated characterization workflow for unconventional gas shales, *in* J. A. Breyer, ed., Shale reservoirs—Giant resources for the 21st century, AAPG Memoir 97, p. 127-150.

Sullivan, K., 1985, Organic facies variation of the Woodford Shale in western Oklahoma: Shale Shaker, v. 35, p. 76-89.

Tréanton, J., 2014, Outcrop-derived chemostratigraphy of the Woodford Shale, Murry County, Oklahoma: Masters thesis, University of Oklahoma, Norman, 100 p.

Tribovillard, N., Algeo, T. J., Lyons, T., and Riboullean, A., 2006, Trace metals as paleoredox and paleoproductivity proxies: an update: Chemical Geology, v. 232, p. 12-32.

Turner, B. W., Tréanton, J. A., Slatt, R. M., 2015, The use of chemostratigraphy to refine ambiguous sequence stratigraphic correlation in marine shales: an example from the Woodford Shale, Oklahoma: AAPG Datapages, Search and Discovery Article #51181, 17 p.

Turner, B. W., 2016, Utilization of chemostratigraphic proxies for generating and refining sequence stratigraphic frameworks in mudrocks and shales: Doctoral thesis, University of Oklahoma, Norman, 153 p.

Zhou, L., Su, J., Huang, J., Yan, J., Xie, X., Gao, S., Dai M., and Tonger, 2011, A new paleoenvironmental index for anoxic events—Mo isotopes in black shales from Upper Yangtze marine sediments: Earth Sciences, v. 54, 7, p. 1024-1033.

Zorn, M. E., 2009, The influence of bioturbation on physical and biogeochemical sediment properties: Effects on early diagenesis: Doctoral thesis, University of Alberta (Canada), Ann Arbor, p. 211.

Zou, F., Slatt, R., 2015, Relationships between bioturbation, microfacies and chemostratigraphy and their implication to the sequence stratigraphic framework of the Woodford Shale in Anadarko Basin, Oklahoma, USA, doi: 10.15530/urtec-2015-2153831.

APPENDIX A: CORE A CORE DESCRIPTION

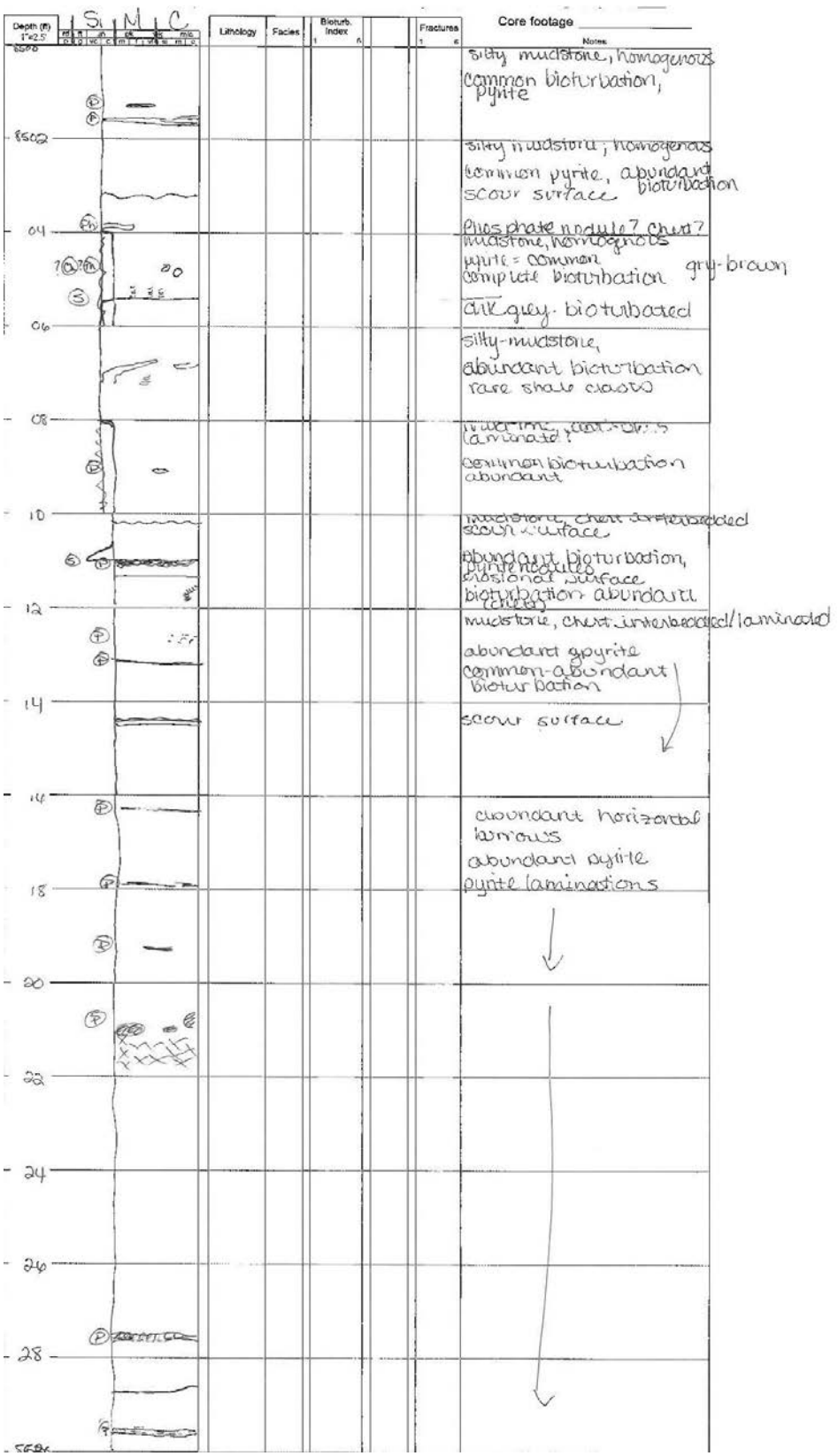

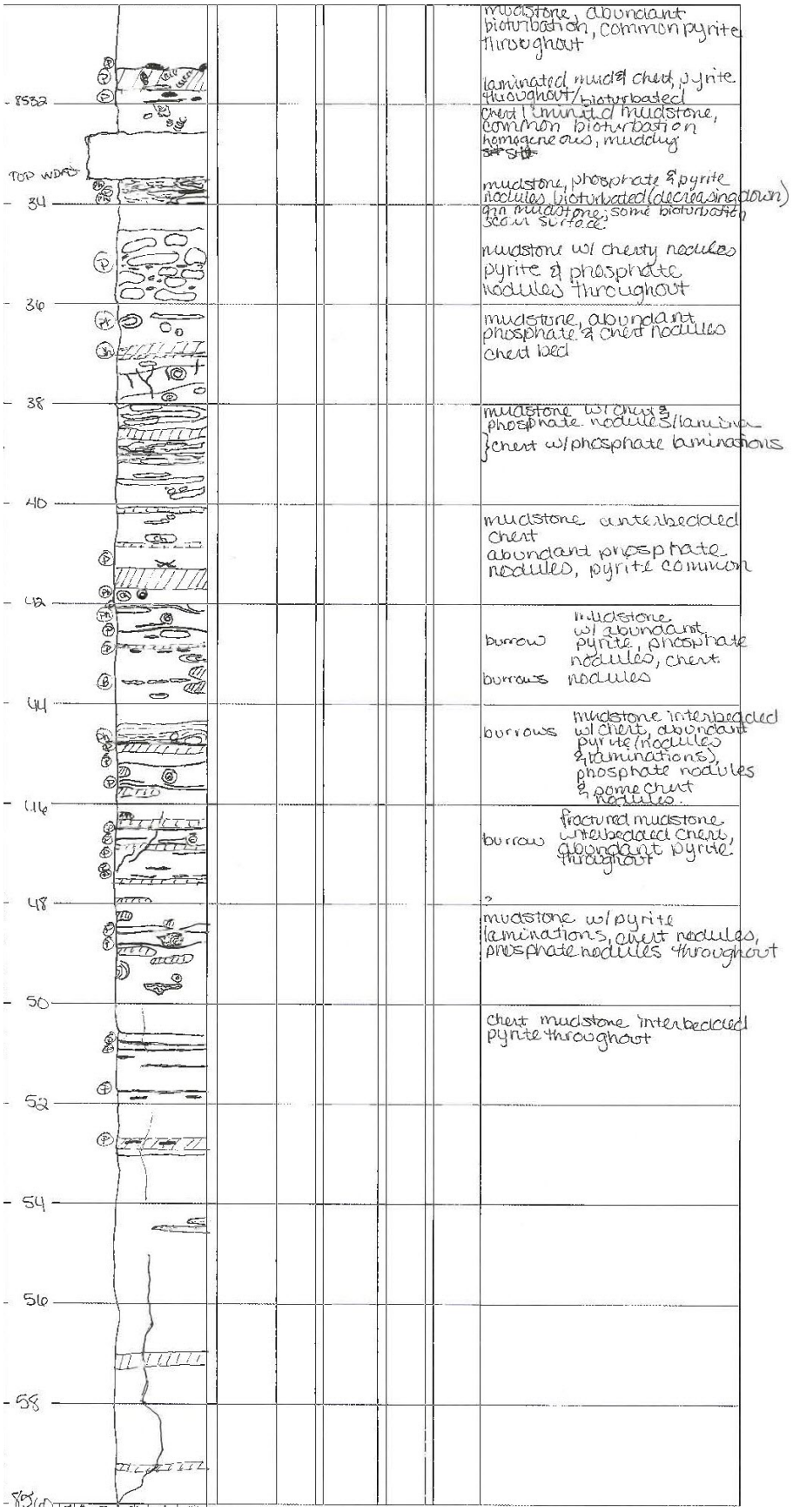
8532
TOP WDFD
34
36
38
40
42
44
46
48
50
52
54
56
58
mudstone, abundant bioturbation, common pyrite throughout
laminated mud & chert, pyrite throughout/bioturbated
chert / laminated mudstone, common bioturbation homogeneous, muddy
mudstone, phosphate & pyrite nodules bioturbated (decreasing down) on mudstone; some bioturbation seen surface
mudstone w/ cherty nodules pyrite & phosphate nodules throughout
mudstone, abundant phosphate & chert nodules chert bed
mudstone w/ chert & phosphate nodules/laminae
chert w/ phosphate laminations
mudstone interbedded chert abundant phosphate nodules, pyrite common
burrow
mudstone w/ abundant pyrite, phosphate nodules, chert
burrows
nodules
burrows
mudstone interbedded w/ chert, abundant pyrite (nodules & laminations), phosphate nodules & some chert nodules.
burrow
fractured mudstone interbedded chert, abundant pyrite throughout
?
mudstone w/ pyrite laminations, chert nodules, phosphate nodules throughout
chert mudstone interbedded pyrite throughout

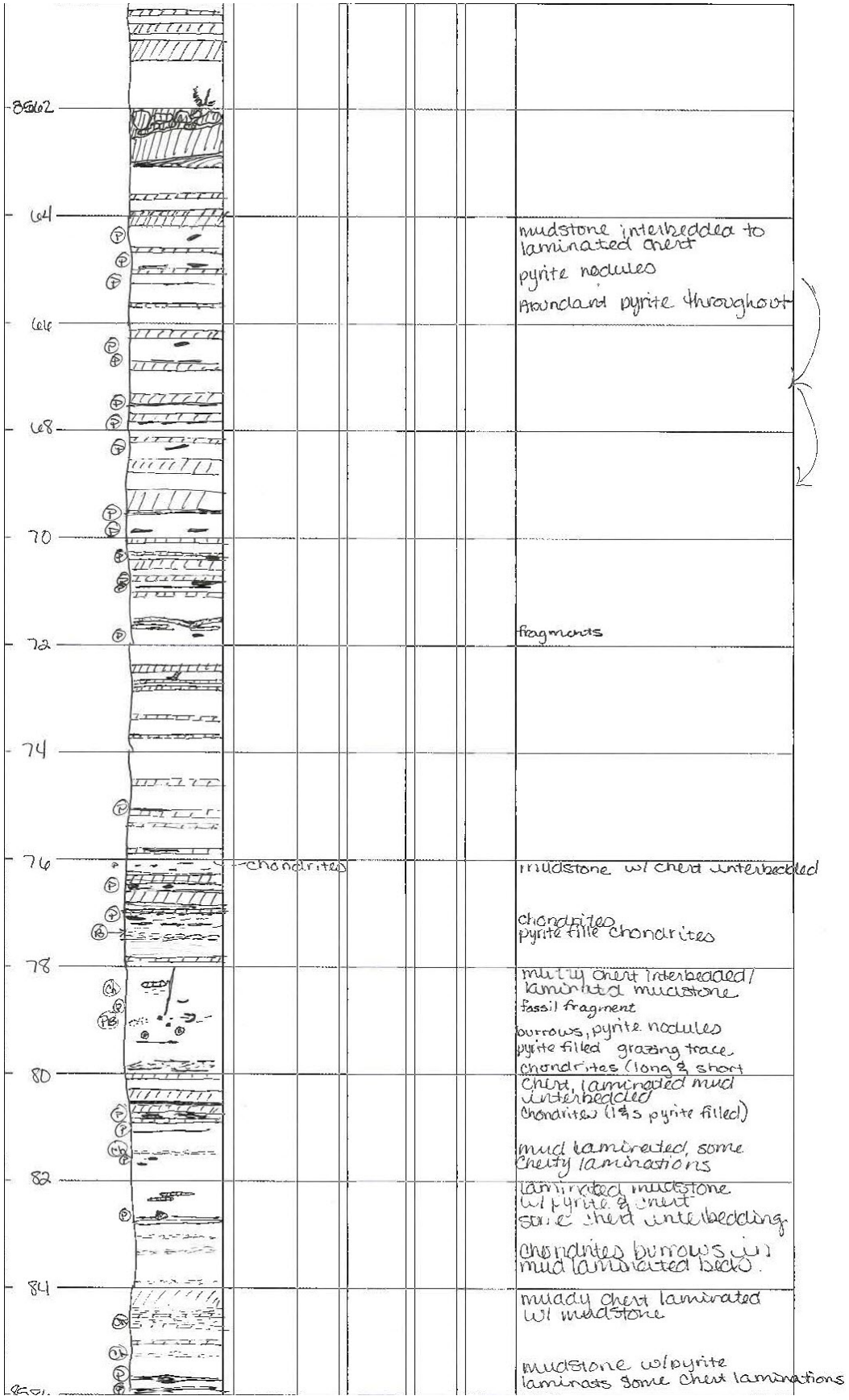
8562
64
66
68
70
72
74
76
78
80
82
84
chondrites
mudstone interbedded to laminated chert
pyrite nodules
Abundant pyrite throughout
fragments
mudstone w/ chert interbedded
chondrites
pyrite fille chondrites
muddy chert interbedded/ laminated mudstone
fossil fragment
burrows, pyrite nodules
pyrite filled grazing trace
chondrites (long & short
Chert, laminated mud interbedded
Chondrites (1's pyrite filled)
mud laminated, some cherty laminations
laminated mudstone w/ pyrite & chert
some chert interbedding
chondrites burrows in mud laminated beds
muddy chert laminated w/ mudstone
mudstone w/ pyrite laminats some chert laminations

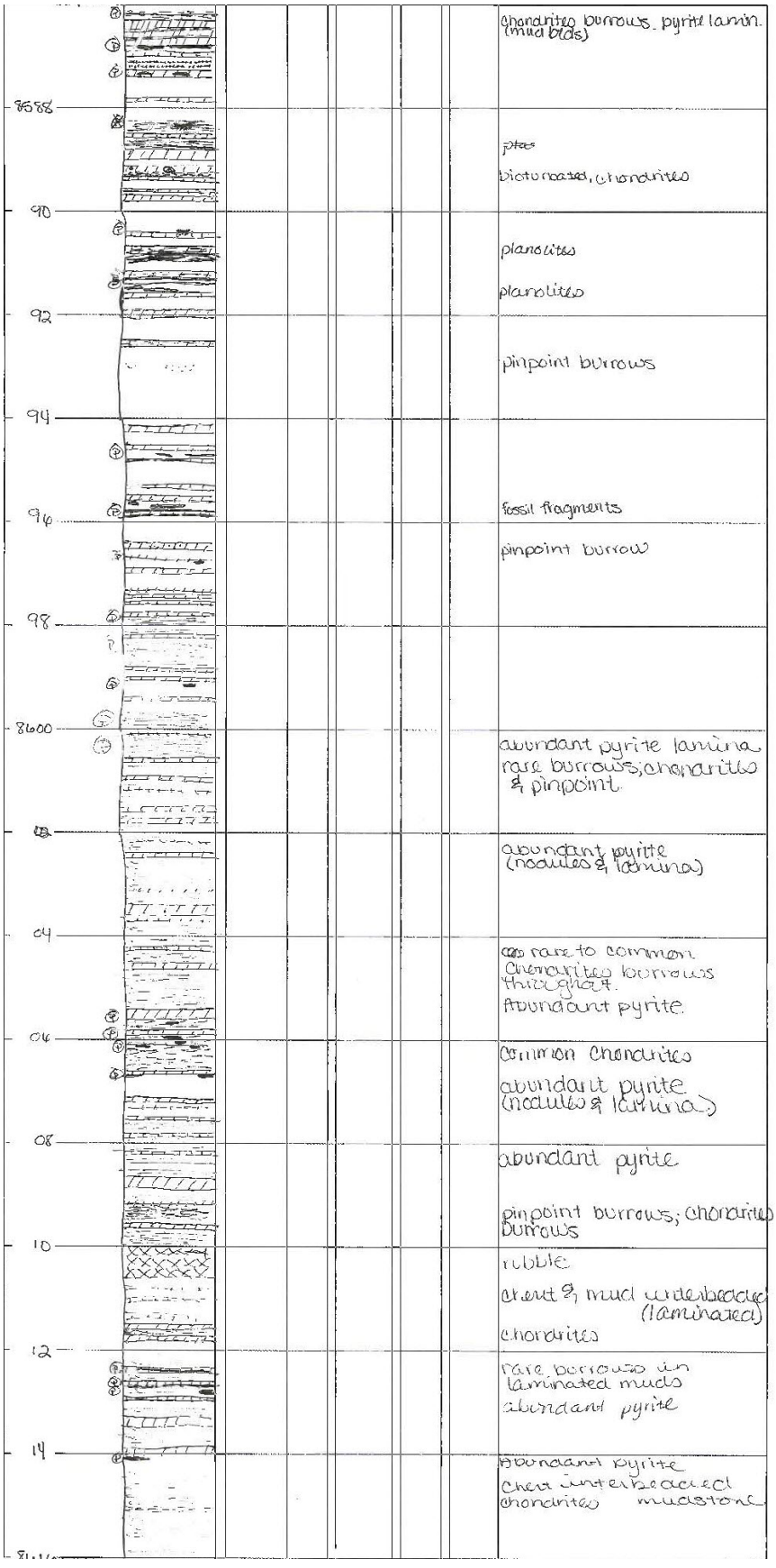
chondrites burrows. pyrite lamin. (mud blds)
8588
bioturbated, chondrites
90
planolites
planolites
92
pinpoint burrows
94
fossil fragments
96
pinpoint burrow
98
8600
abundant pyrite lamina
rare burrows; chondrites & pinpoint
abundant pyrite (nodules & lamina)
04
rare to common chondrites burrows throughout.
Abundant pyrite
06
common chondrites
abundant pyrite (nodules & lamina)
08
abundant pyrite
pinpoint burrows; chondrites burrows
10
rubble
chert & mud interbedded (laminated)
chondrites
12
rare burrows in laminated muds
abundant pyrite
14
Abundant pyrite
chert interbedded
chondrites mudstone

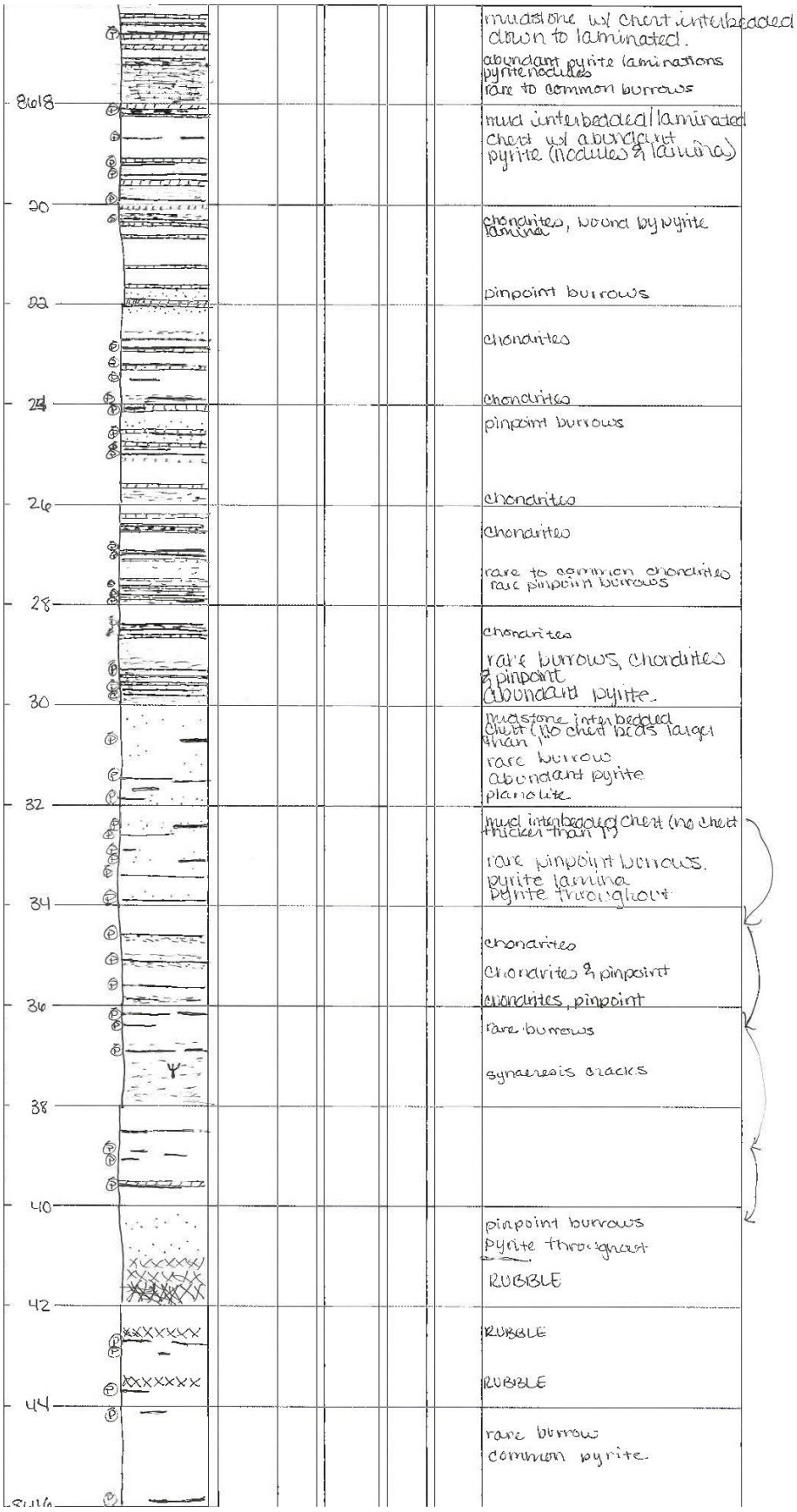
mudstone w/ chert interbedded
drawn to laminated.
abundant pyrite laminations
pyrite nodules
rare to common burrows
8618
mud interbedded/laminated
chert w/ abundant
pyrite (nodules & laminae)
20
chondrites, bound by pyrite
laminae
pinpoint burrows
22
chondrites
chondrites
24
pinpoint burrows
chondrites
26
chondrites
rare to common chondrites
rare pinpoint burrows
28
chondrites
rare burrows, chondrites
& pinpoint
abundant pyrite.
30
mudstone interbedded
chert (no chert beds larger
than 1")
rare burrows
abundant pyrite
planolite.
32
mud interbedded chert (no chert
thicker than 1")
rare pinpoint burrows.
pyrite lamina
pyrite throughout
34
chondrites
chondrites & pinpoint
chondrites, pinpoint
36
rare burrows
synaeresis cracks
38
40
pinpoint burrows
pyrite throughout
RUBBLE
42
RUBBLE
RUBBLE
44
rare burrow
common pyrite.

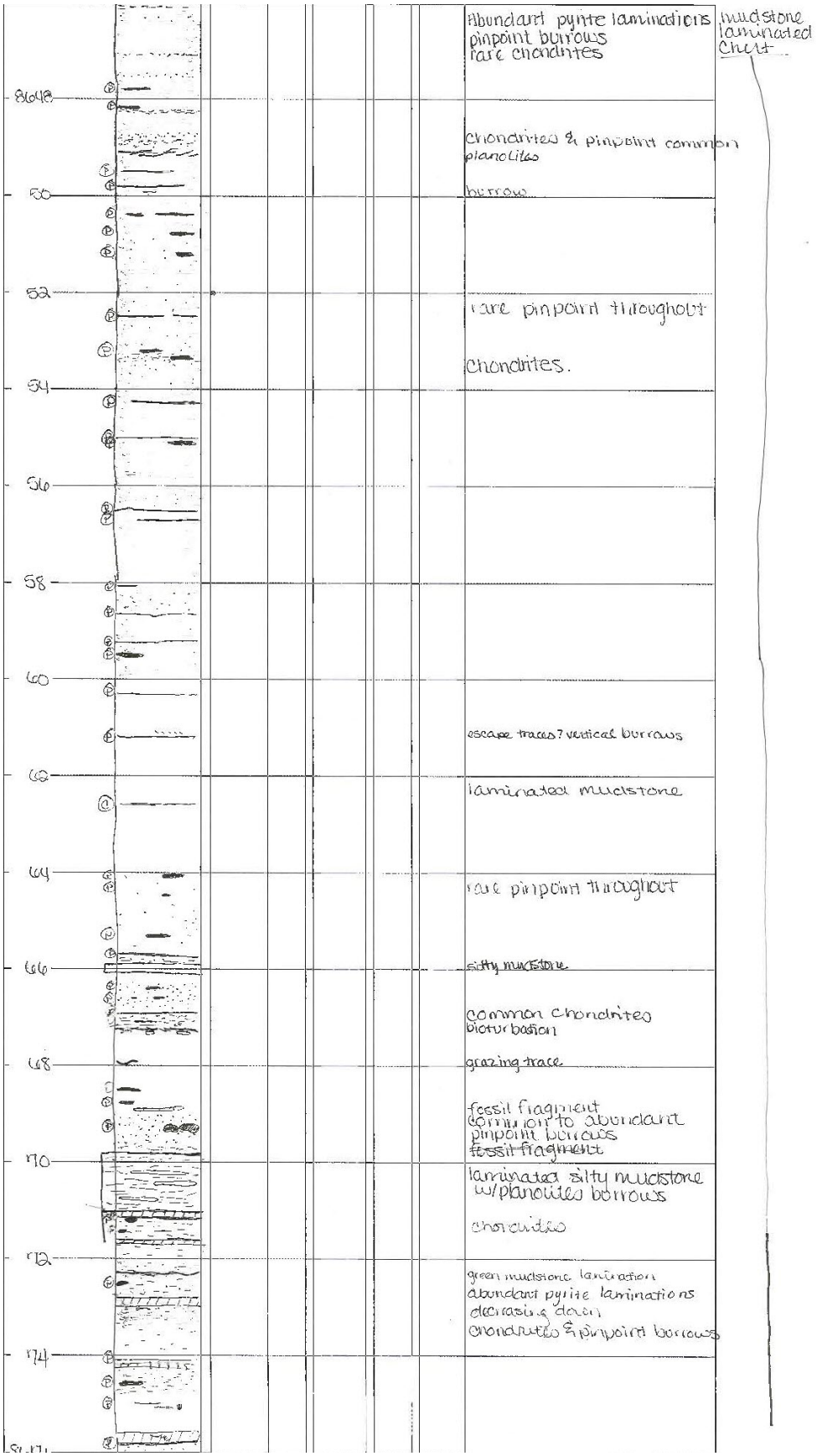
Abundant pyrite laminations
pinpoint burrows
rare chondrites
mudstone laminated Chert
8648
chondrites & pinpoint common planolites
burrows
50
52
rare pinpoint throughout
chondrites.
54
56
58
60
escape traces? vertical burrows
62
laminated mudstone
64
rare pinpoint throughout
66
silty mudstone
common chondrites bioturbation
68
grazing trace
fossil fragment common to abundant pinpoint burrows
fossil fragment
70
laminated silty mudstone w/planolites burrows
chondrites
72
green mudstone lamination
abundant pyrite laminations decreasing down
chondrites & pinpoint burrows
74

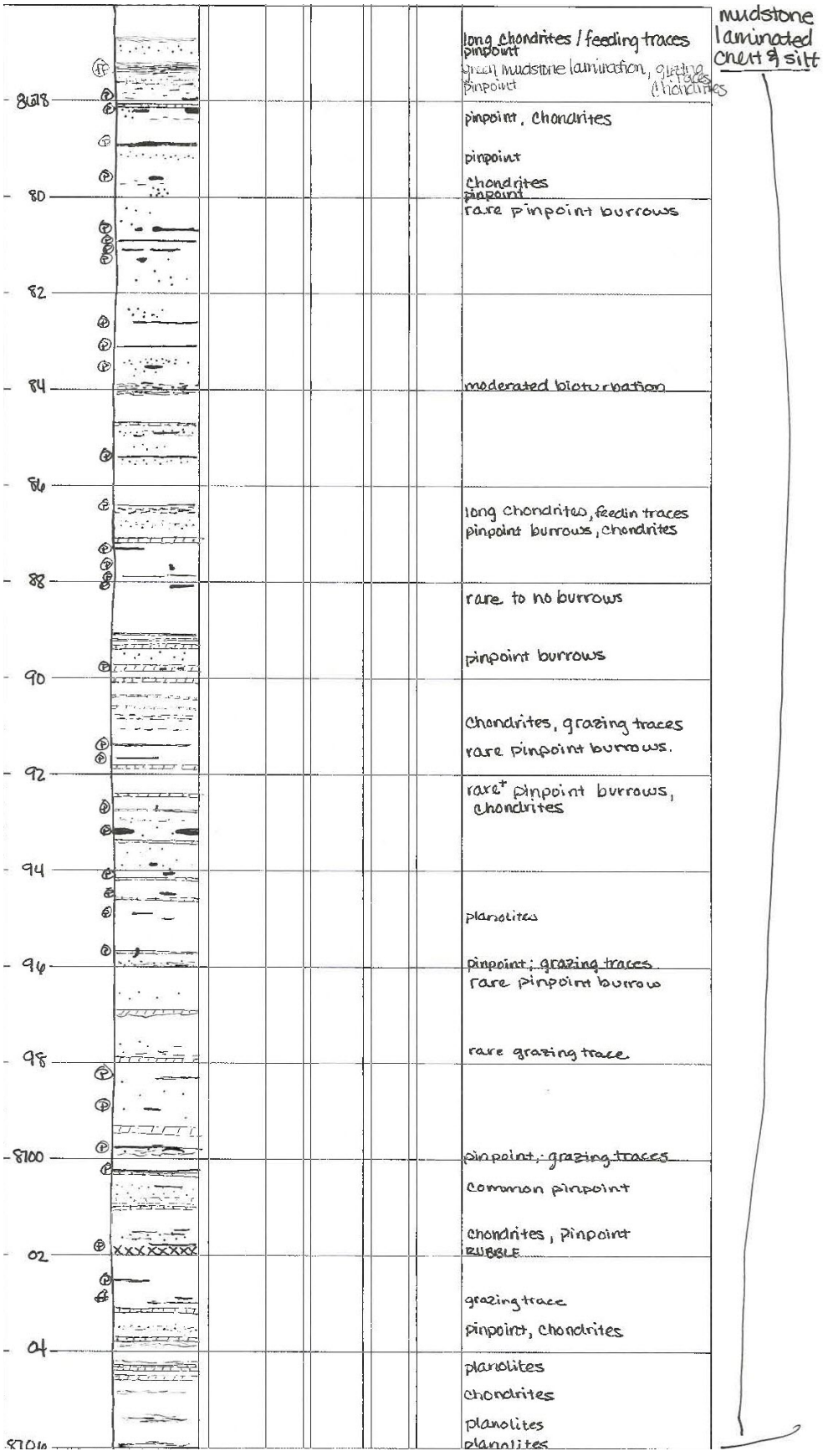
mudstone laminated chert & silt
long chondrites / feeding traces pinpoint
green mudstone lamination, grazing traces (chondrites)
pinpoint
8078
pinpoint, chondrites
pinpoint
chondrites
pinpoint
80
rare pinpoint burrows
82
84
moderated bioturbation
86
long chondrites, feedin traces
pinpoint burrows, chondrites
88
rare to no burrows
pinpoint burrows
90
chondrites, grazing traces
rare pinpoint burrows.
92
rare+ pinpoint burrows,
chondrites
94
planolites
pinpoint; grazing traces.
96
rare pinpoint burrow
rare grazing trace
98
8100
pinpoint; grazing traces
common pinpoint
chondrites, pinpoint
02
BUBBLE
grazing trace
pinpoint, chondrites
04
planolites
chondrites
planolites
planolites

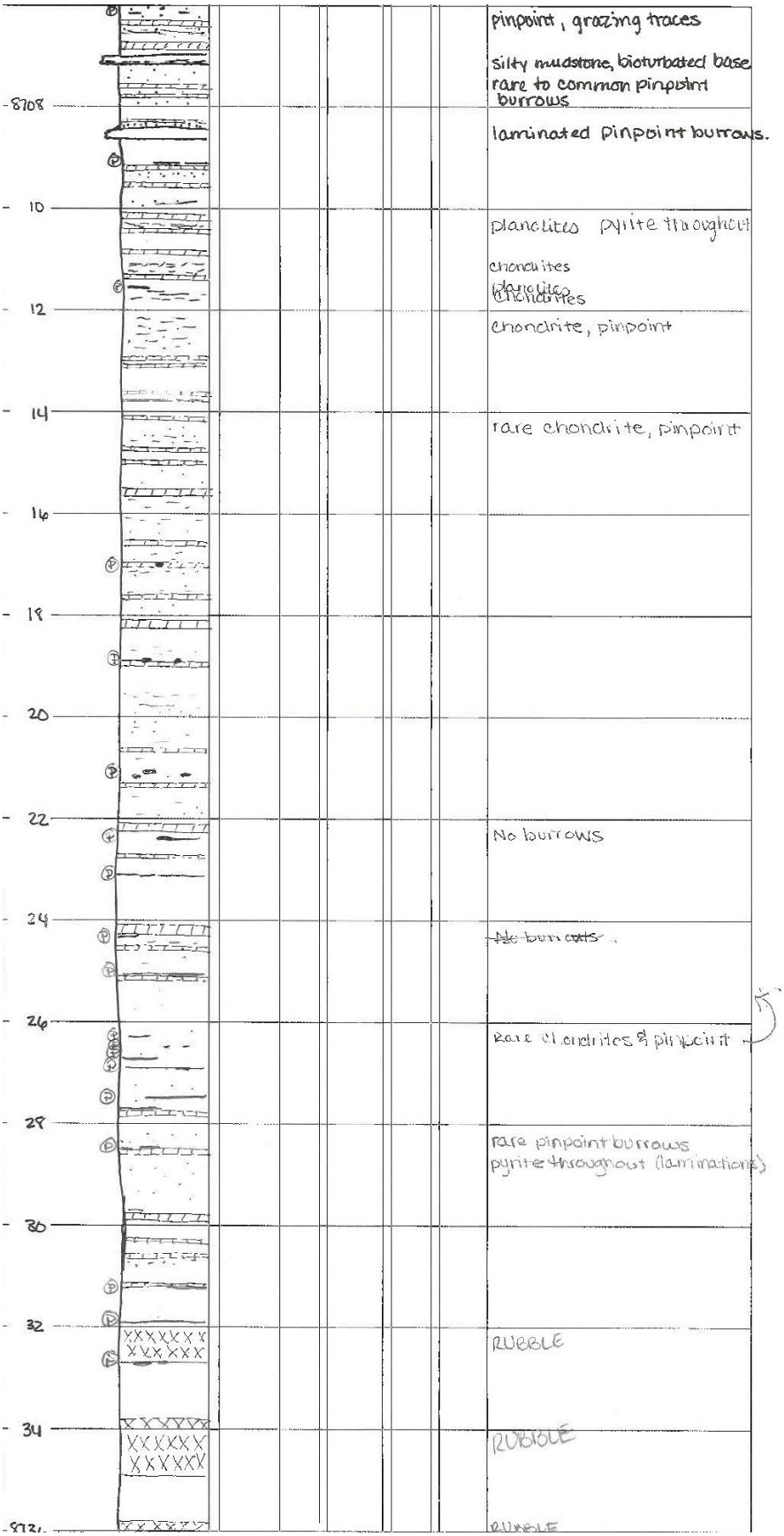
pinpoint, grazing traces
silty mudstone, bioturbated base
rare to common pinpoint burrows
-8708
laminated pinpoint burrows.
10
planolites pyrite throughout
chondrites
planolites
chondrites
12
chondrite, pinpoint
14
rare chondrite, pinpoint
16
18
20
22
No burrows
24
~~No burrows~~
26
Rare chondrites & pinpoint
28
rare pinpoint burrows
pyrite throughout (laminations)
30
32
RUBBLE
34
RUBBLE
RUBBLE

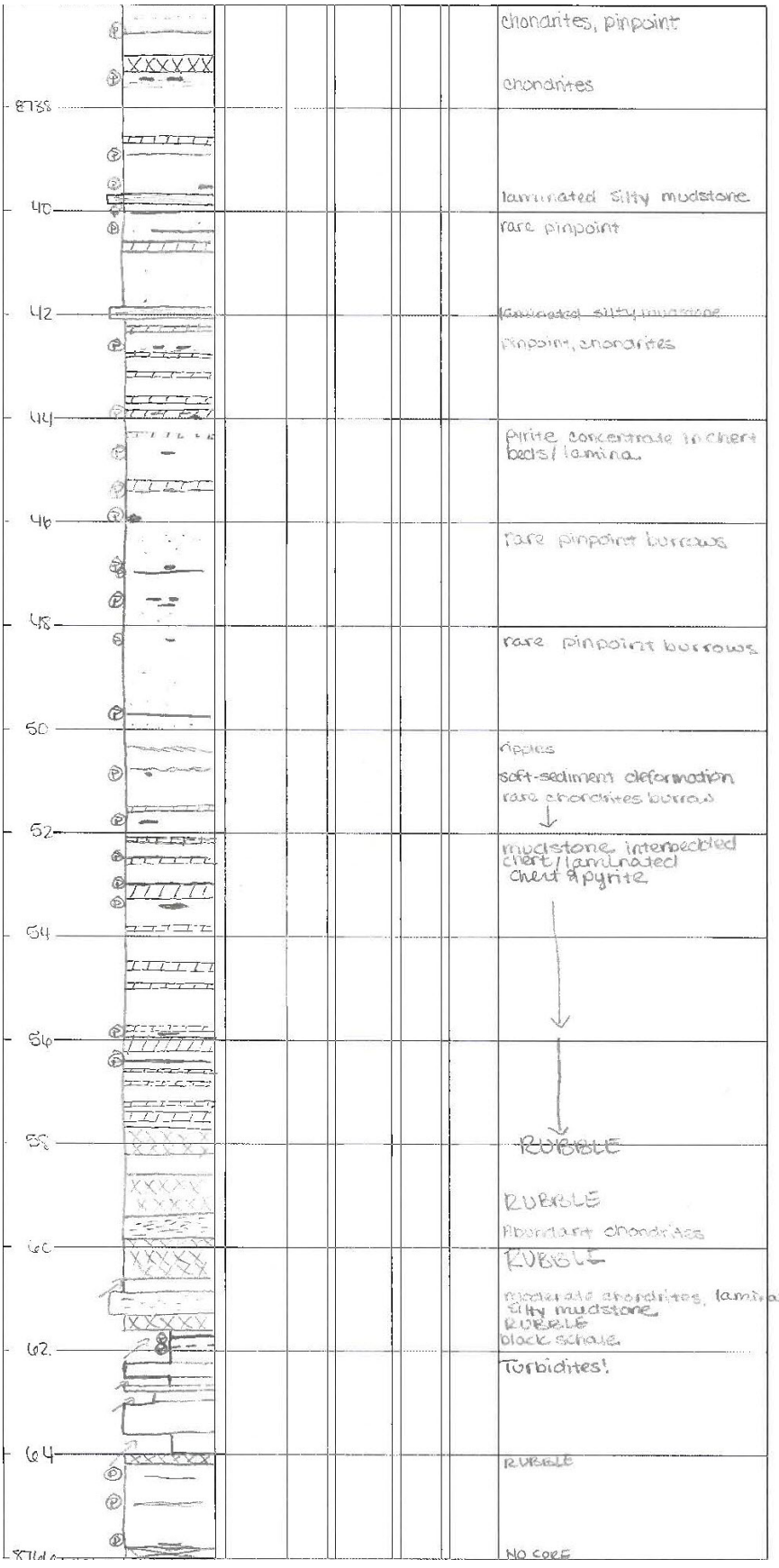
chonarites, pinpoint
chondrites
8738
laminated silty mudstone
40
rare pinpoint
42
pinpoint, chondrites
44
pirite concentrate in chert beds/lamina.
46
rare pinpoint burrows
48
rare pinpoint burrows
50
ripples
soft-sediment deformation
rare chondrites burrows
52
mudstone interbedded chert/laminated chert & pyrite
54
56
58
RUBBLE
RUBBLE
Abundant chondrites
60
RUBBLE
moderate chondrites, laminated silty mudstone
RUBBLE
block schale.
62
Turbidites!
64
RUBBLE
NO CORE

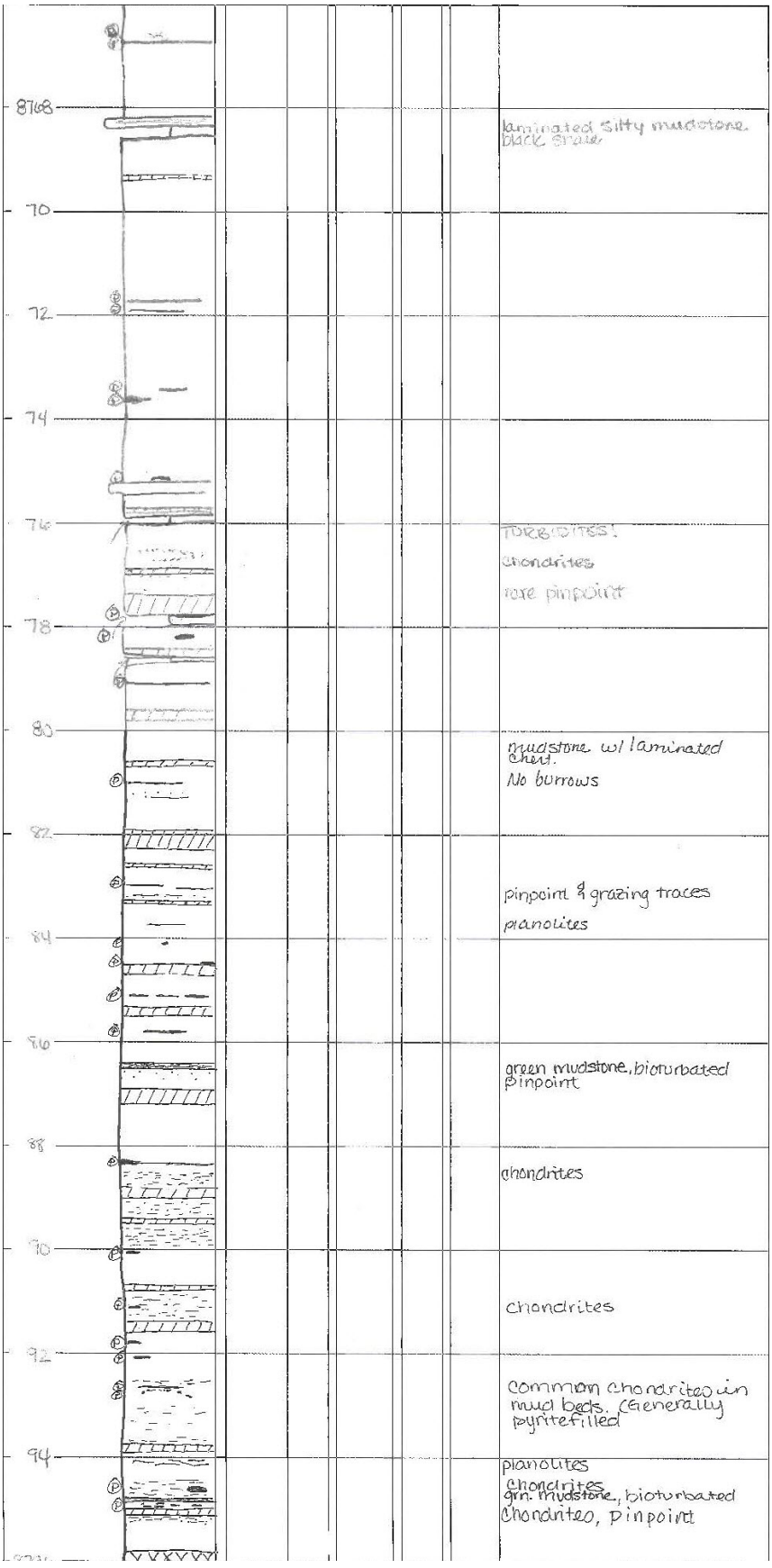
8768
70
72
74
76
78
80
82
84
86
88
90
92
94
laminated silty mudstone. black shale
TURBIDITES!
chondrites
rare pinpoint
mudstone w/ laminated chert.
No burrows
pinpoint & grazing traces
planolites
green mudstone, bioturbated
pinpoint
chondrites
chondrites
common chondrites in mud beds. Generally pyrite filled
planolites
chondrites
grn. mudstone, bioturbated
Chondrites, pinpoint

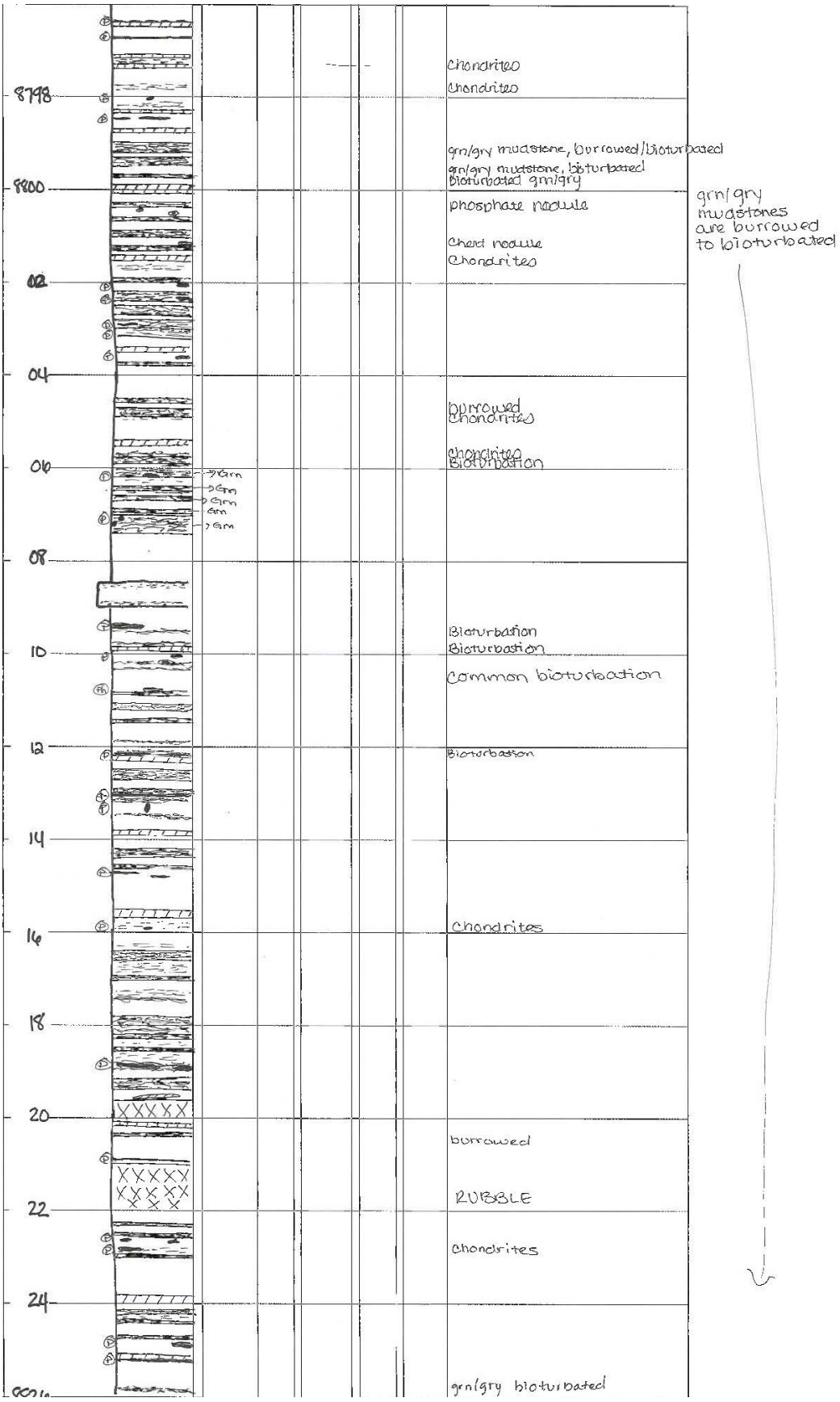
8798
8800
02
04
06
08
10
12
14
16
18
20
22
24
Chondrites
Chondrites
grn/gry mudstone, burrowed/bioturbated
grn/gry mudstone, bioturbated
Bioturbated grn/gry
phosphate nodule
Chert nodule
Chondrites
burrowed
Chondrites
Chondrites
Bioturbation
Grn
Grn
Grn
Grn
Grn
Bioturbation
Bioturbation
common bioturbation
Bioturbation
Chondrites
burrowed
RUBBLE
Chondrites
grn/gry bioturbated
grn/gry mudstones are burrowed to bioturbated

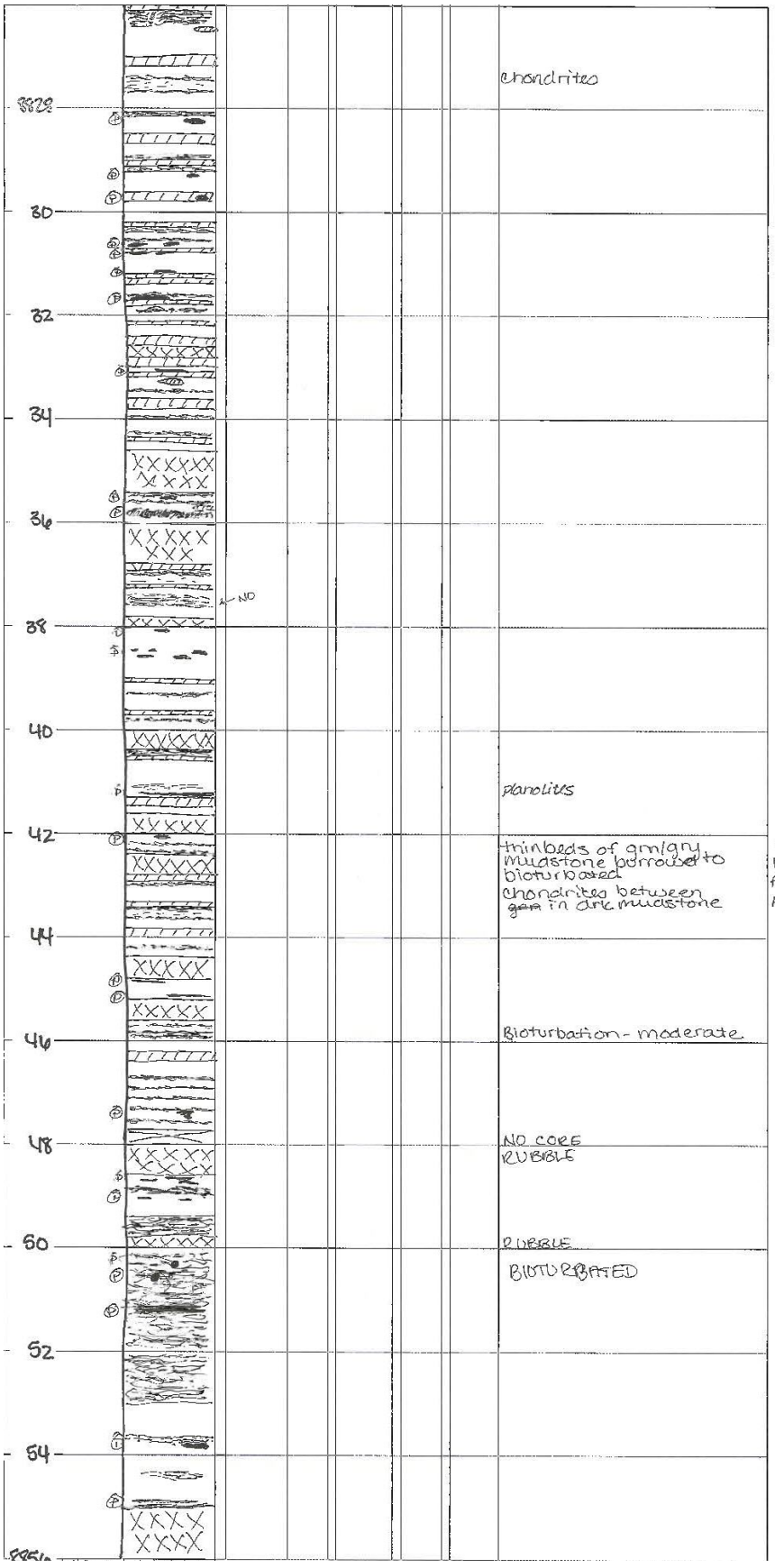
chondrites
30
32
34
36
38
40
42
44
46
48
50
52
54
ND
planolites
thinbeds of grn/gry mudstone burrowed to bioturbated chondrites between in drk mudstone
Bioturbation - moderate
NO CORE
RUBBLE
RUBBLE
BIOTURBATED
VERY HIGHLY FRACTURED ALONG BEDDING PLANES

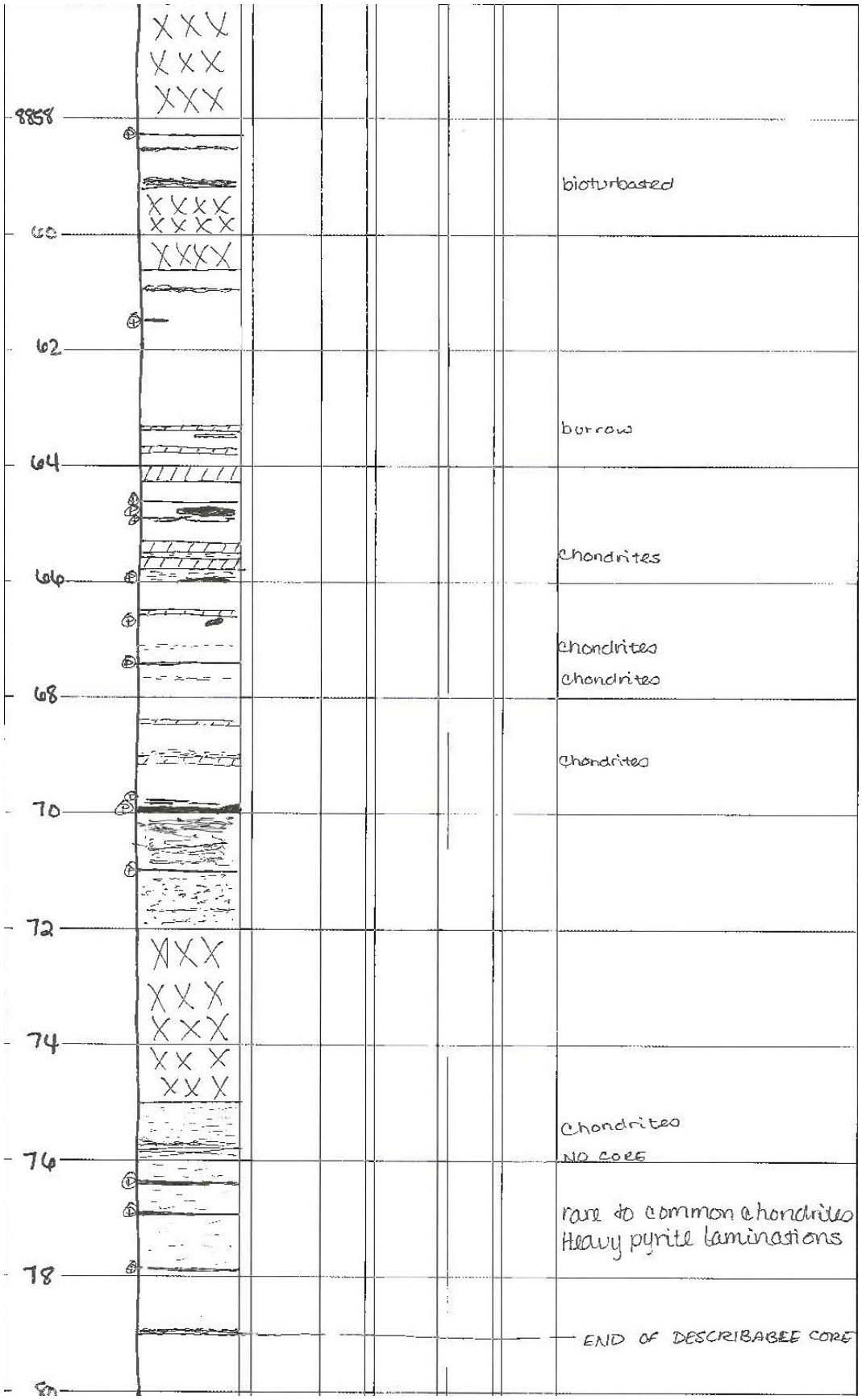
8858
60
62
64
66
68
70
72
74
76
78
bioturbated
burrow
chondrites
chondrites
chondrites
chondrites
NO CORE
rare to common chondrites
Heavy pyrite laminations
END OF DESCRIBABLE CORE

APPENDIX B: CORE B CORE DESCRIPTION

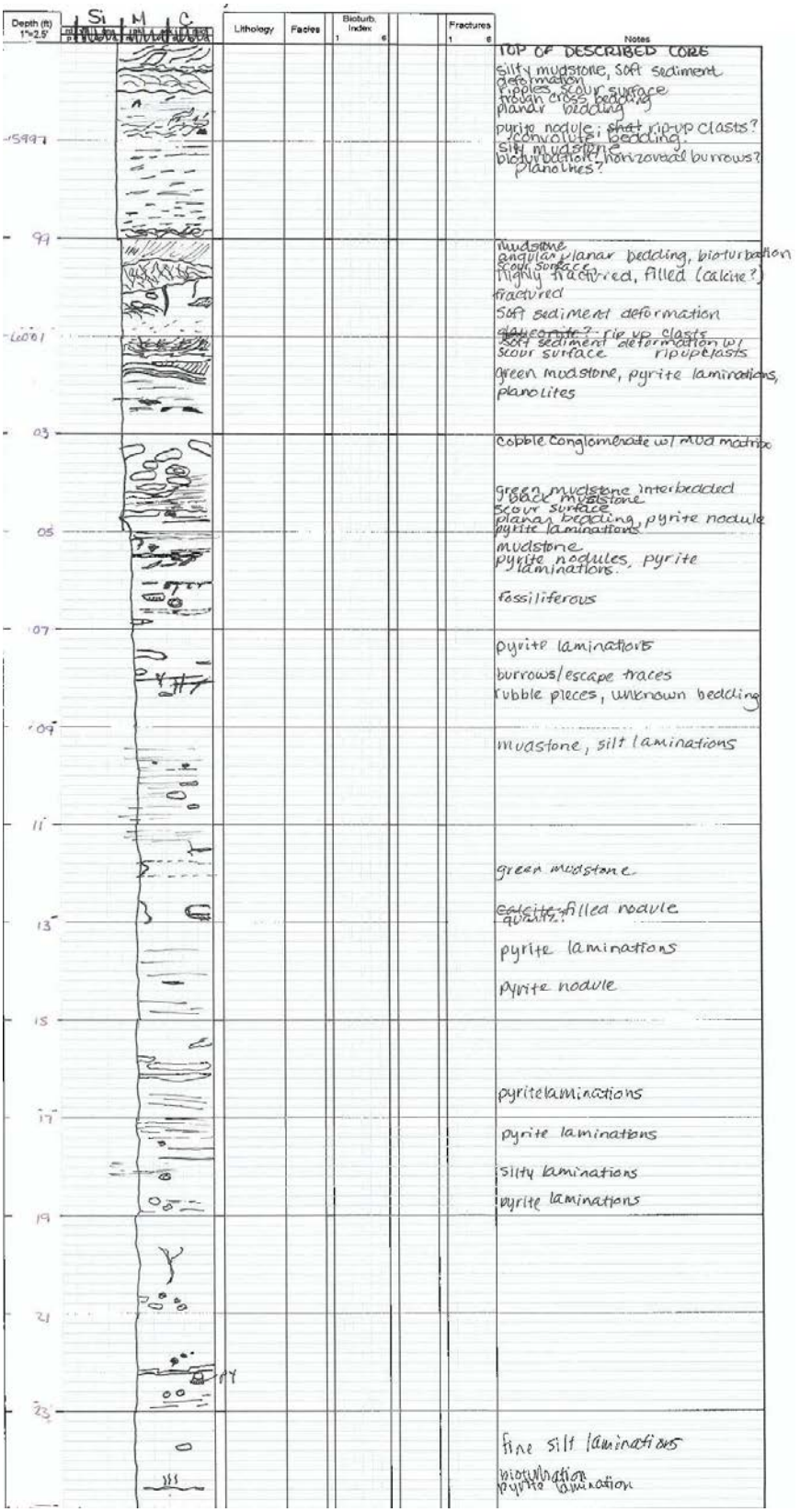

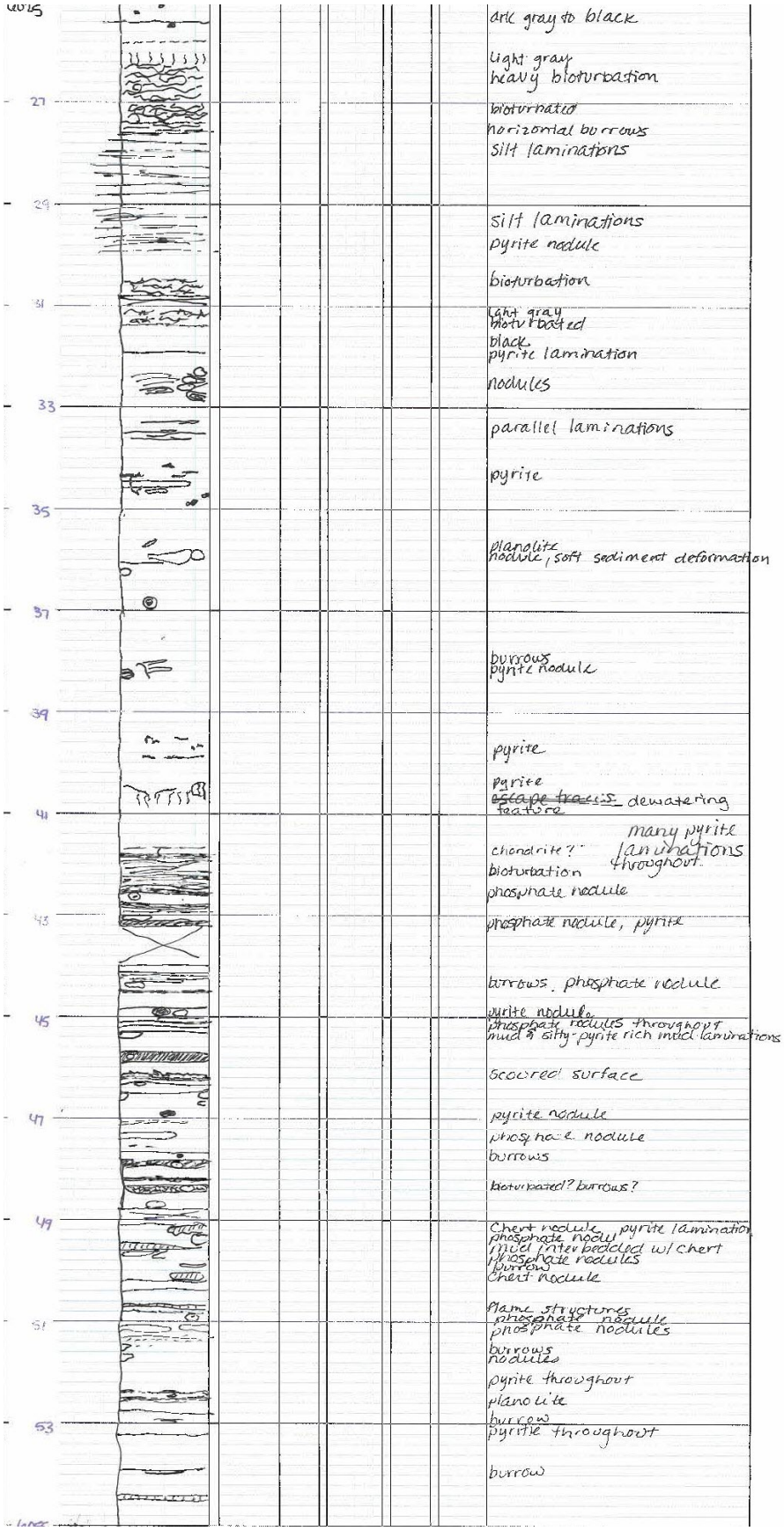
dark gray to black
light gray
heavy bioturbation
bioturbated
horizontal burrows
silt laminations
silt laminations
pyrite nodule
bioturbation
light gray
bioturbated
black
pyrite lamination
nodules
parallel laminations
pyrite
planolite
nodule, soft sediment deformation
burrows
pyrite nodule
pyrite
pyrite
escape traces dewatering feature
many pyrite laminations throughout
chondrite?
bioturbation
phosphate nodule
phosphate nodule, pyrite
burrows. phosphate nodule
pyrite nodule.
phosphate nodules throughout
mud & silty-pyrite rich mud laminations
scoured surface
pyrite nodule
phosphate nodule
burrows
bioturbated? burrows?
Chert nodule pyrite lamination
phosphate nodu
mud interbedded w/ chert
phosphate nodules
burrow
Chert nodule
flame structures
phosphate nodule
phosphate nodules
burrows
nodules
pyrite throughout
planolite
burrow
pyrite throughout
burrow

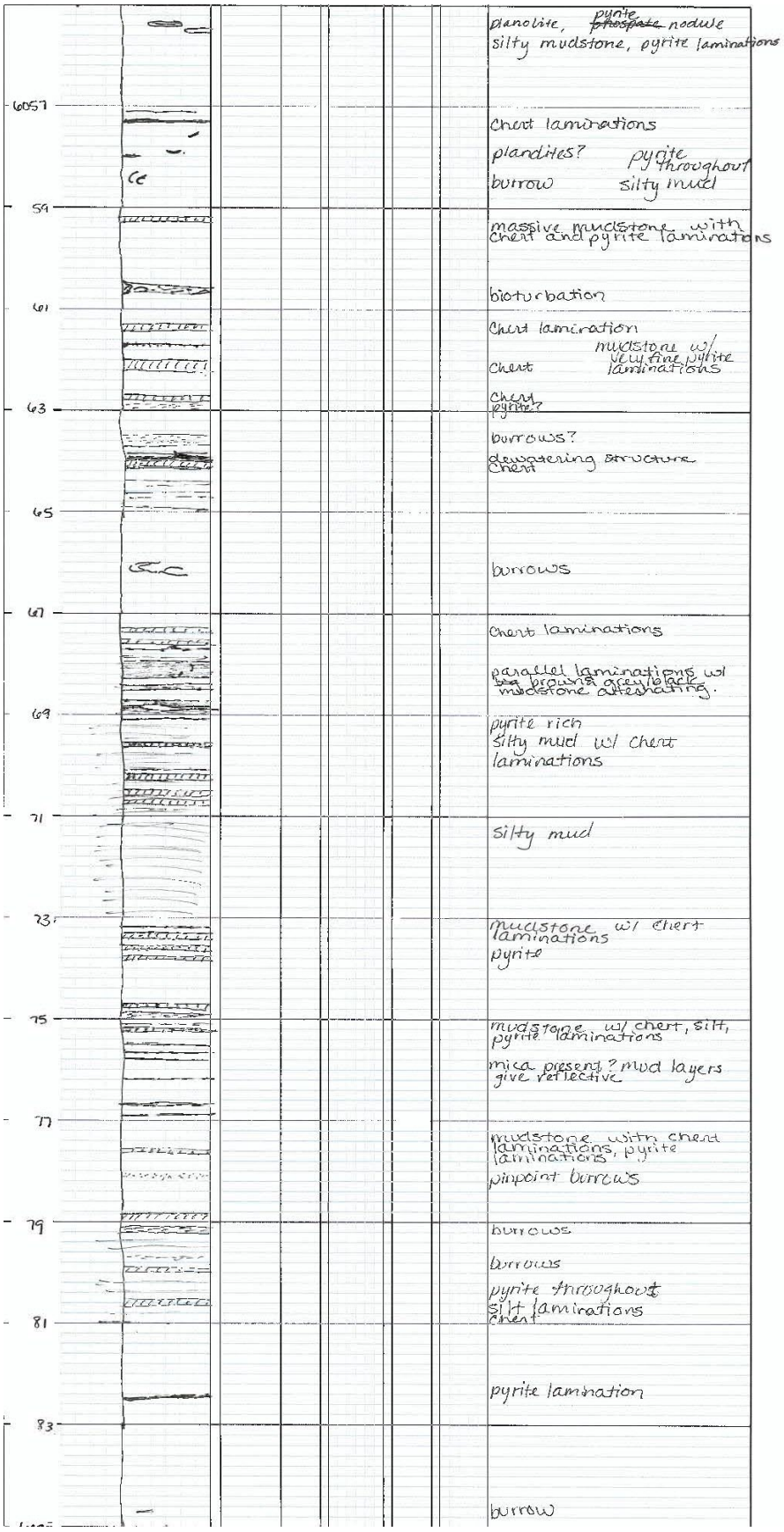
planolite, pyrite phosphate nodule
silty mudstone, pyrite laminations
6057
chert laminations
planolites?
pyrite throughout
burrow
silty mudst
59
massive mudstone with chert and pyrite laminations
bioturbation
61
Chert lamination
mudstone w/ very fine pyrite laminations
Chert
Chert pyrite?
63
burrows?
dewatering structure
Chert
65
burrows
67
Chert laminations
parallel laminations w/ beg brown grey/black mudstone alternating.
69
pyrite rich
silty mud w/ chert laminations
71
silty mud
73
mudstone w/ chert laminations
pyrite
75
mudstone w/ chert, silt, pyrite laminations
mica present? mud layers give reflective
77
mudstone with chert laminations, pyrite laminations
pinpoint burrows
79
burrows
burrows
pyrite throughout
silt laminations
chert
81
pyrite lamination
83
burrow

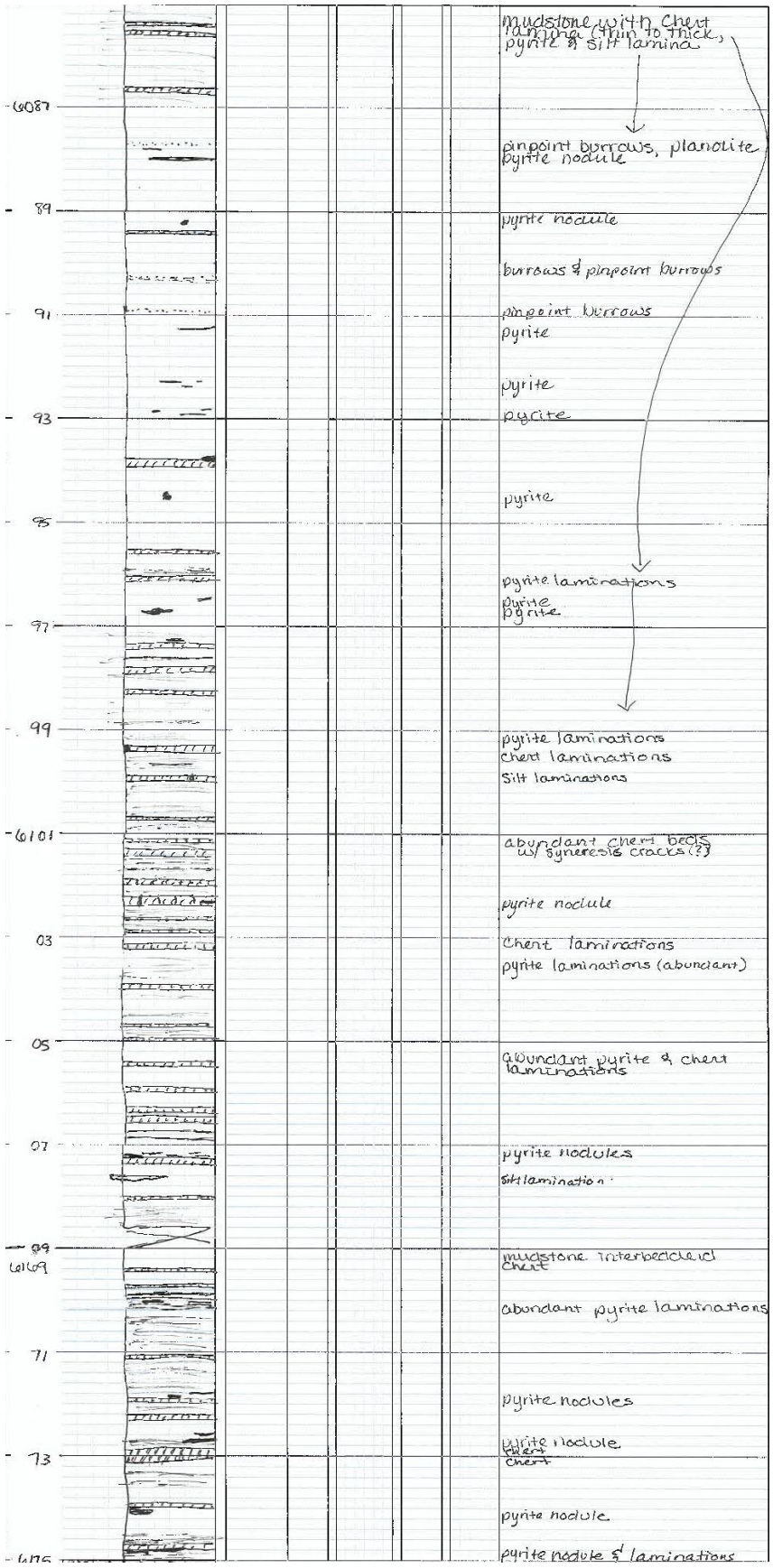
mudstone with chert lamina (thin to thick), pyrite & silt lamina
6087
pinpoint burrows, planolite pyrite nodule
89
pyrite nodule
burrows & pinpoint burrows
91
pinpoint burrows
pyrite
pyrite
93
pyrite
pyrite
95
pyrite laminations
pyrite
pyrite
97
99
pyrite laminations
chert laminations
silt laminations
6101
abundant chert beds w/ syneresis cracks (?)
pyrite nodule
03
chert laminations
pyrite laminations (abundant)
05
abundant pyrite & chert laminations
07
pyrite nodules
silt lamination
09
6109
mudstone interbedded chert
abundant pyrite laminations
71
pyrite nodules
pyrite nodule
73
chert
chert
pyrite nodule
pyrite nodule & laminations

pyrite
burrow
pyrite
mud interbedded chert w/ synaeresis cracks
chert
pyrite
pyrite
bioturbated
bioturbated
pyrite nodules
chert
pyrite
chert
pyrite
pyrite burrows?
nodule
pyrite nodules
chert
pyrite
chert w/ pyrite
bioturbation
pyrite
interbedded chert & mudstone
pyrite laminations & nodules
interbedded chert & mudstone w/ silt & pyrite laminations
burrows
pyrite nodule
interbedded to laminated chert & mudstone
abundant pyrite (nodules & laminations)
bioturbated post depositional faulting (fractures)
bioturbated
bioturbated
6177
79
81
83
85
87
89
91
93
95
97
99
6201
03

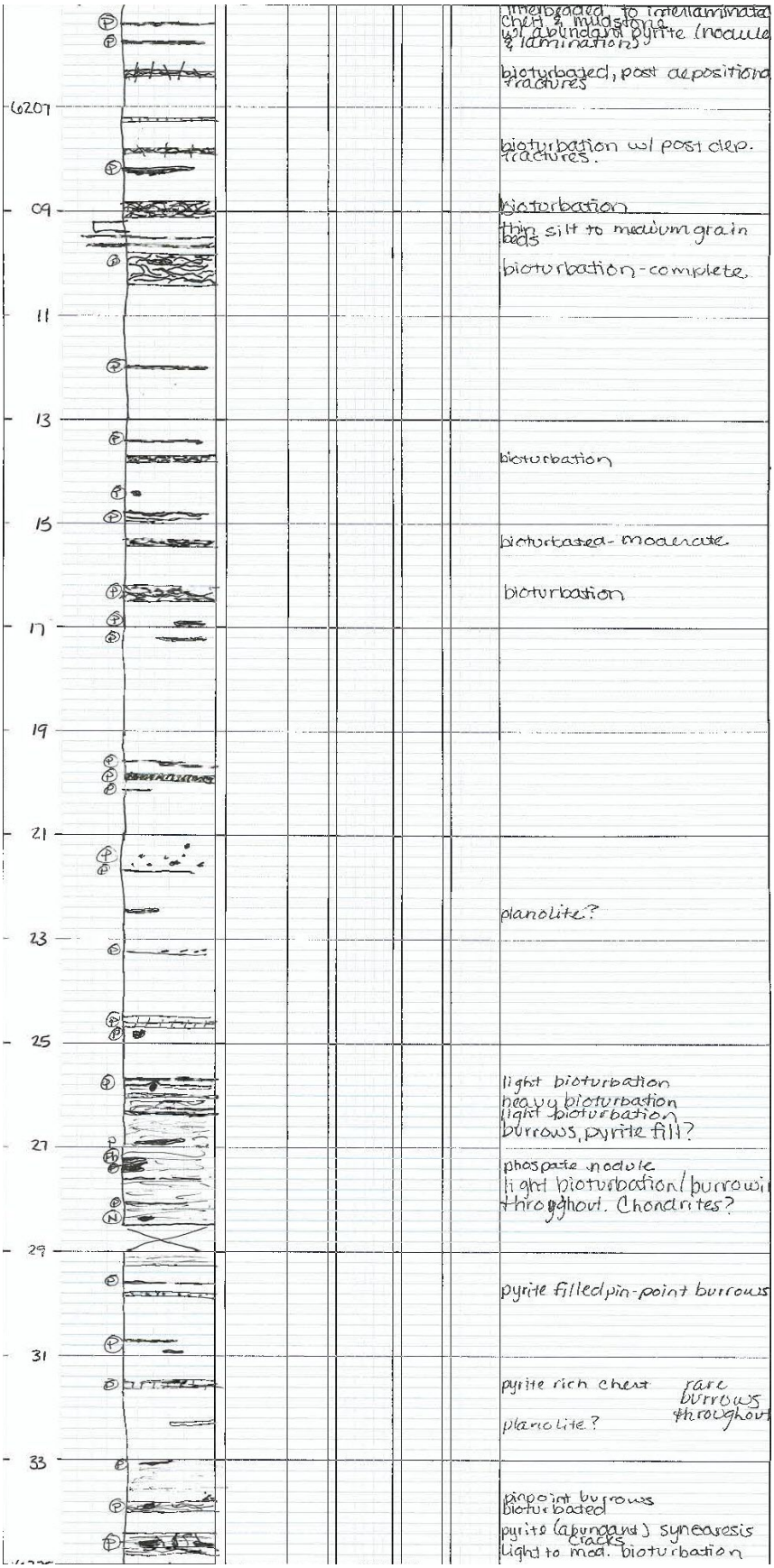
interbedded to laterlaminated chert & mudstone w/ abundant pyrite (nodule & lamination)
bioturbated, post depositional fractures
6207
bioturbation w/ post dep. fractures.
09
bioturbation
thin beds silt to medium grain
bioturbation - complete.
11
13
bioturbation
15
bioturbated - moderate.
bioturbation
17
19
21
planolite?
23
25
light bioturbation
heavy bioturbation
light bioturbation
burrows, pyrite fill?
27
phospate nodule
light bioturbation / burrowi throughout. Chondrites?
29
pyrite filled pin-point burrows
31
pyrite rich chert
rare burrows throughout
planolite?
33
pinpoint burrows bioturbated
pyrite (abundant) syneresis cracks
light to mod. bioturbation

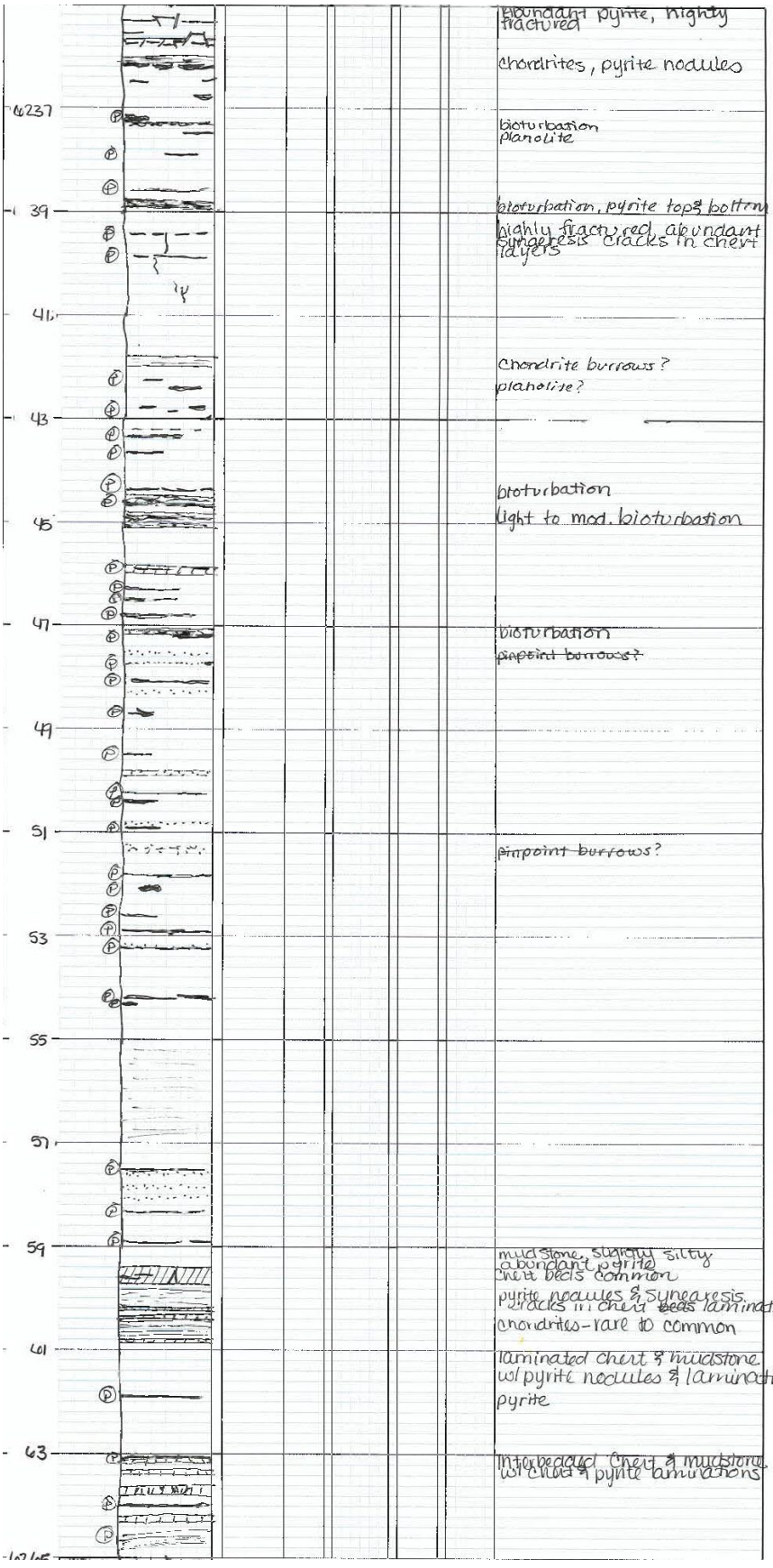
abundant pyrite, highly fractured
chondrites, pyrite nodules
6237
bioturbation
planolite
39
bioturbation, pyrite top & bottom
highly fractured, abundant synaeresis cracks in chert layers
41
chondrite burrows?
planolite?
43
bioturbation
light to mod. bioturbation
45
bioturbation
~~pinpoint burrows?~~
47
~~pinpoint burrows?~~
49
51
53
55
57
59
mudstone, slightly silty
abundant pyrite
chert beds common
pyrite nodules & synaeresis cracks in chert beds laminations
chondrites - rare to common
61
laminated chert & mudstone
w/ pyrite nodules & laminations
pyrite
63
interbedded chert & mudstone
w/ chert & pyrite laminations

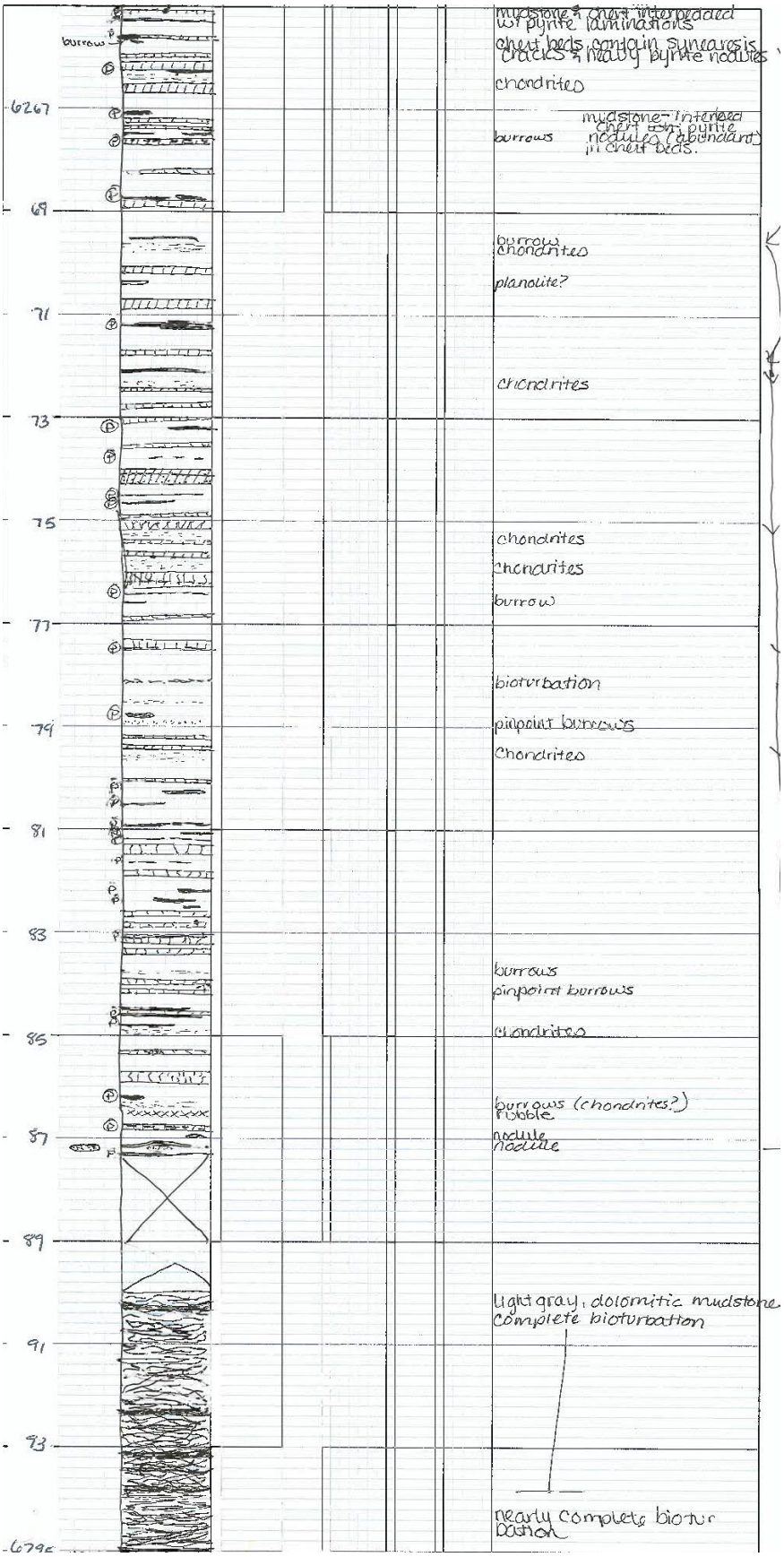
burrows
6267
69
71
73
75
77
79
81
83
85
87
89
91
93
6295
mudstone- chert interbedded w/ pyrite laminations
chert beds contain syneresis cracks + heavy pyrite nodules
chondrites
mudstone- interbed chert w/ pyrite nodules (abundant) in chert beds.
burrows
burrows
chondrites
planolite?
chondrites
chondrites
chondrites
burrow
bioturbation
pinpoint burrows
chondrites
burrows
pinpoint burrows
chondrites
burrows (chondrites?)
nodule
nodule
light gray, dolomitic mudstone
complete bioturbation
nearly complete bioturbation

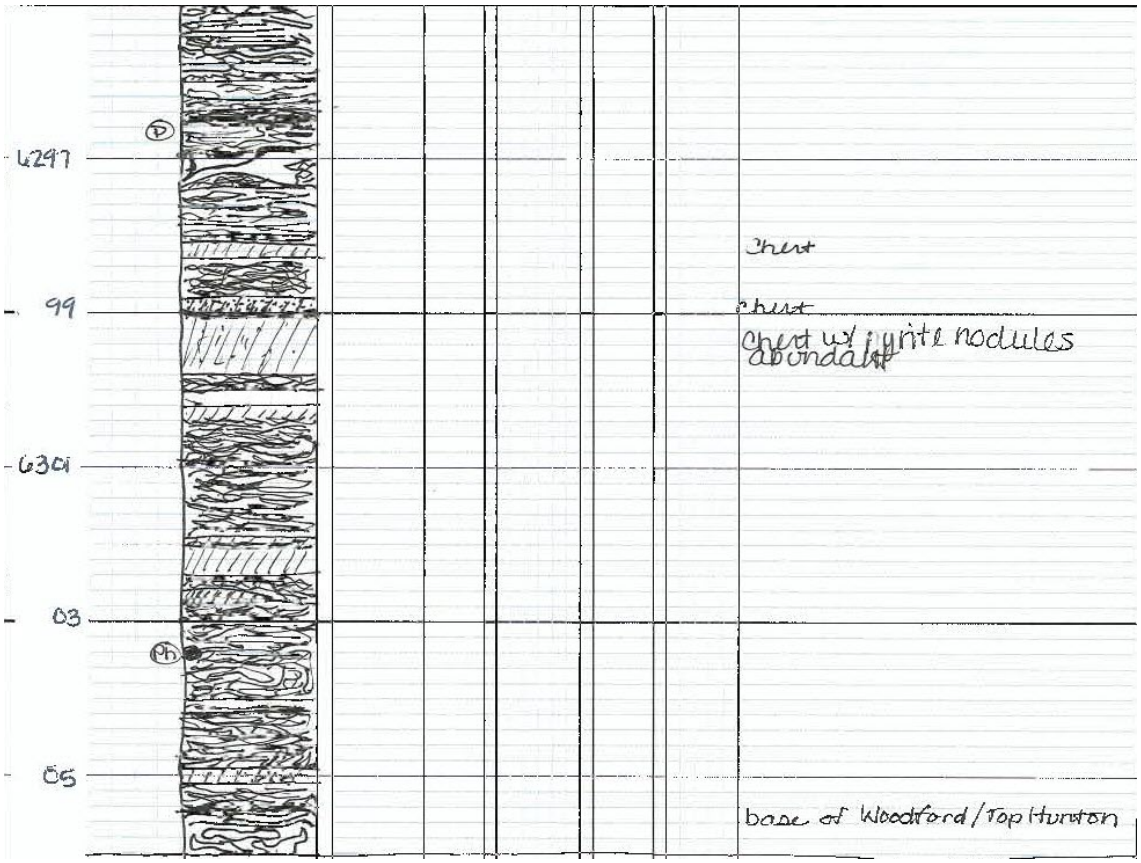
6297
99
6301
03
05
chert
chert
chert w/ pyrite nodules abundant
base of Woodford / Top Hunton

APPENDIX C: CORE C CORE DESCRIPTION

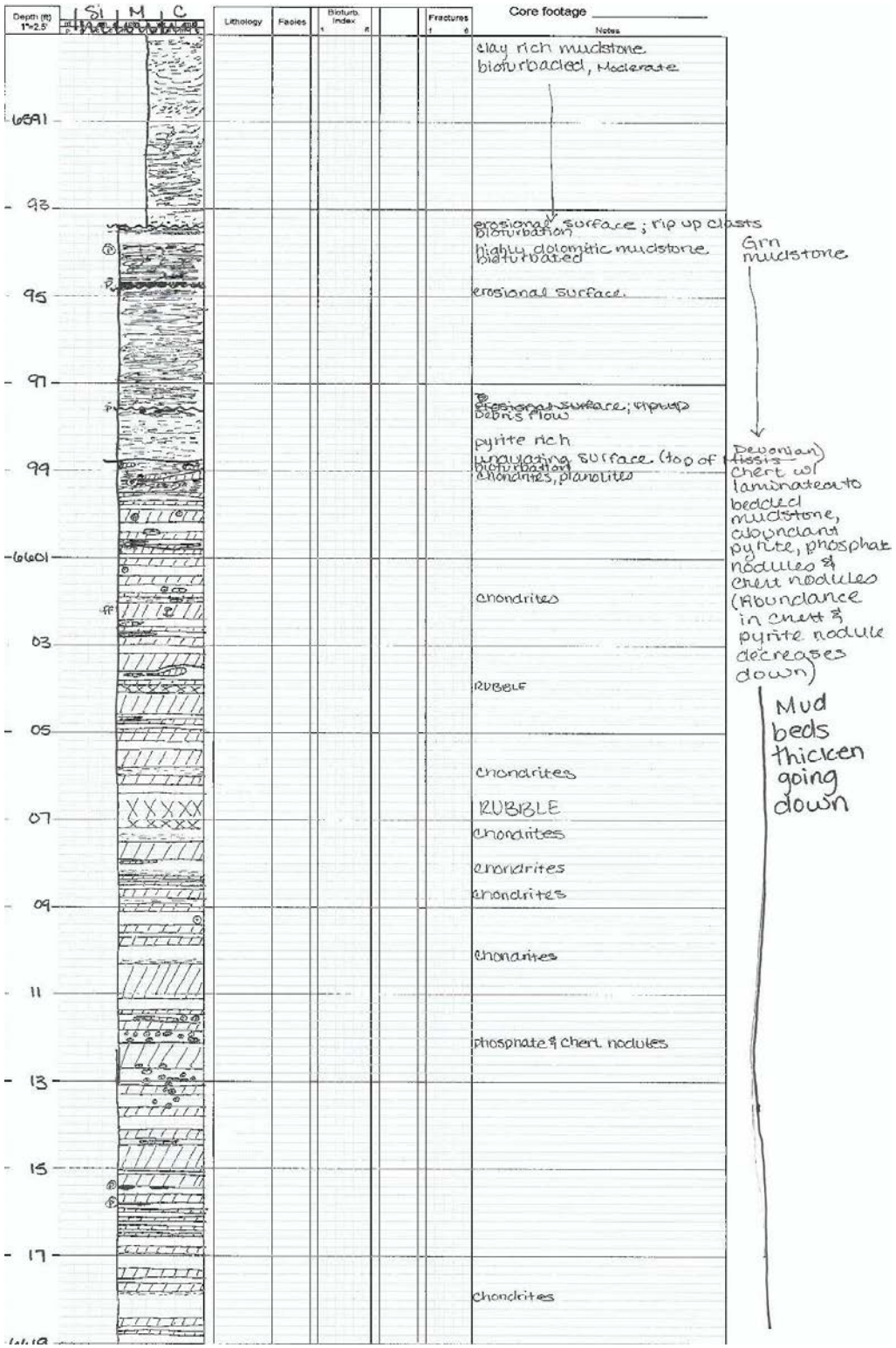

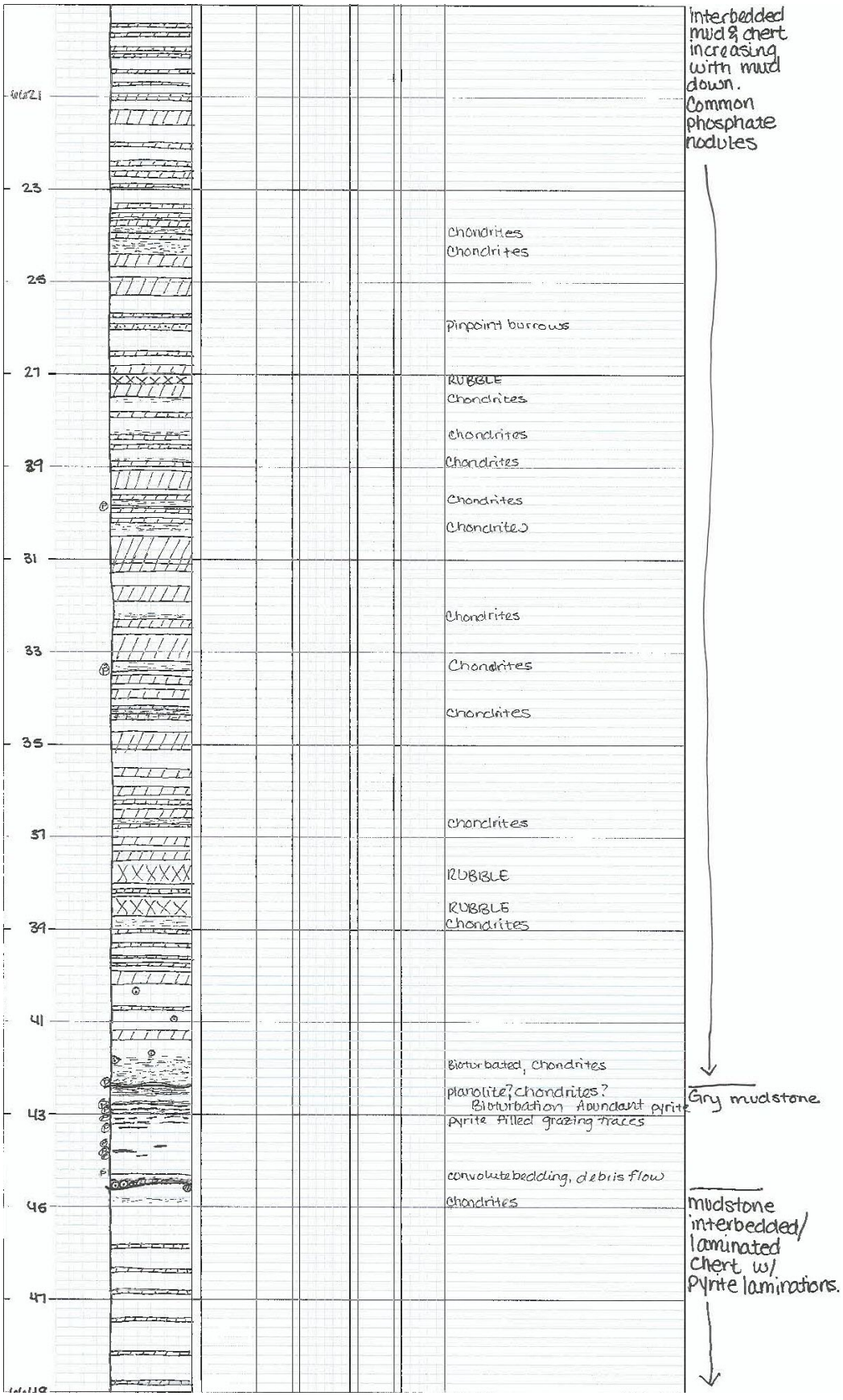
interbedded mud & chert increasing with mud down. Common phosphate nodules
23
26
27
29
31
33
35
37
39
41
43
46
47
Chondrites
Chondrites
Pinpoint burrows
RUBBLE
Chondrites
Chondrites
Chondrites
Chondrites
Chondrites
Chondrites
Chondrites
RUBBLE
RUBBLE
Chondrites
Bioturbated, Chondrites
planolite? chondrites?
Bioturbation Abundant pyrite
Pyrite filled grazing traces
convolute bedding, debris flow
Chondrites
Gry mudstone
mudstone interbedded/ laminated chert w/ pyrite laminations.

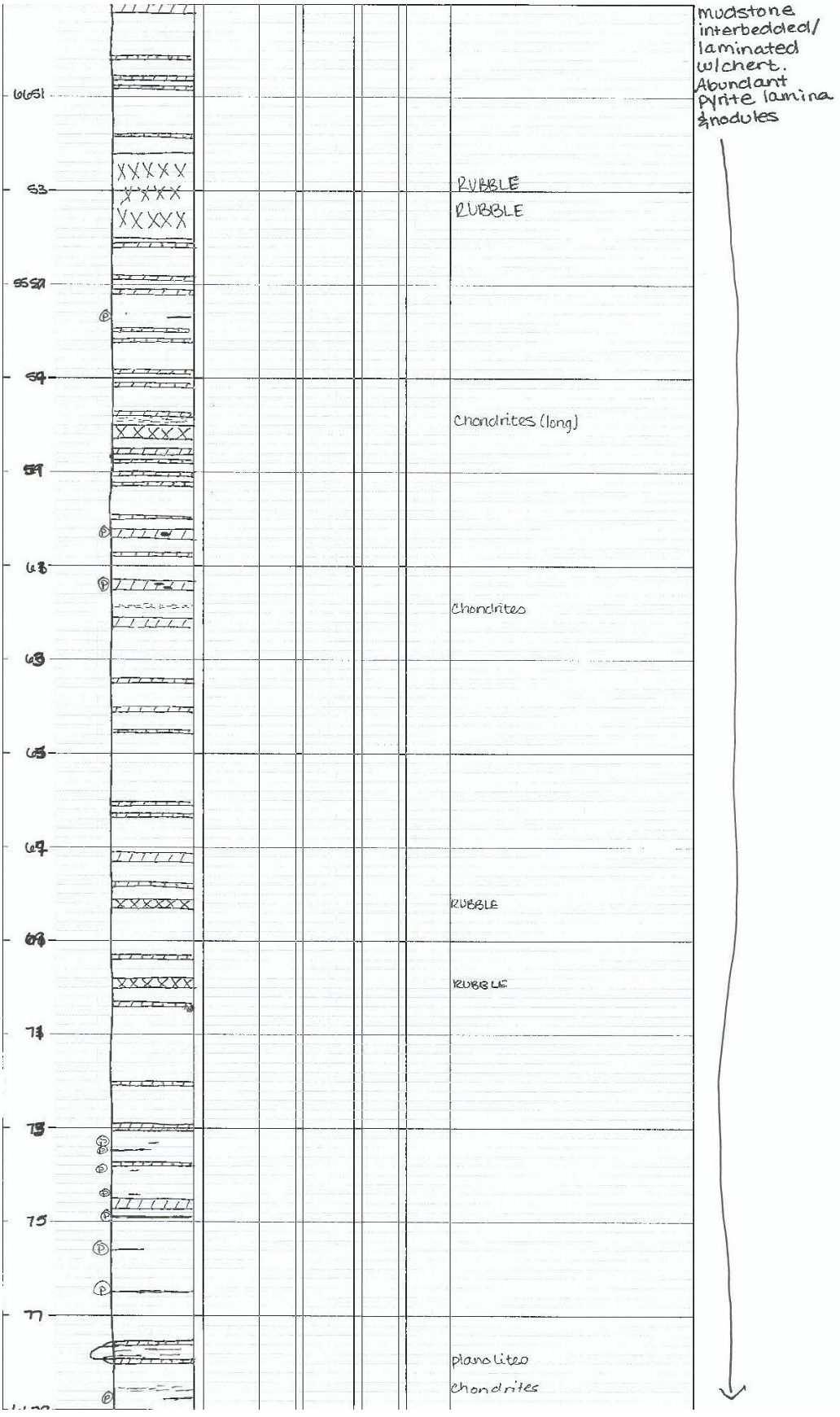
mudstone interbedded/ laminated w/chert. Abundant pyrite lamina & nodules
RUBBLE
RUBBLE
Chondrites (long)
Chondrites
RUBBLE
RUBBLE
planolites
Chondrites

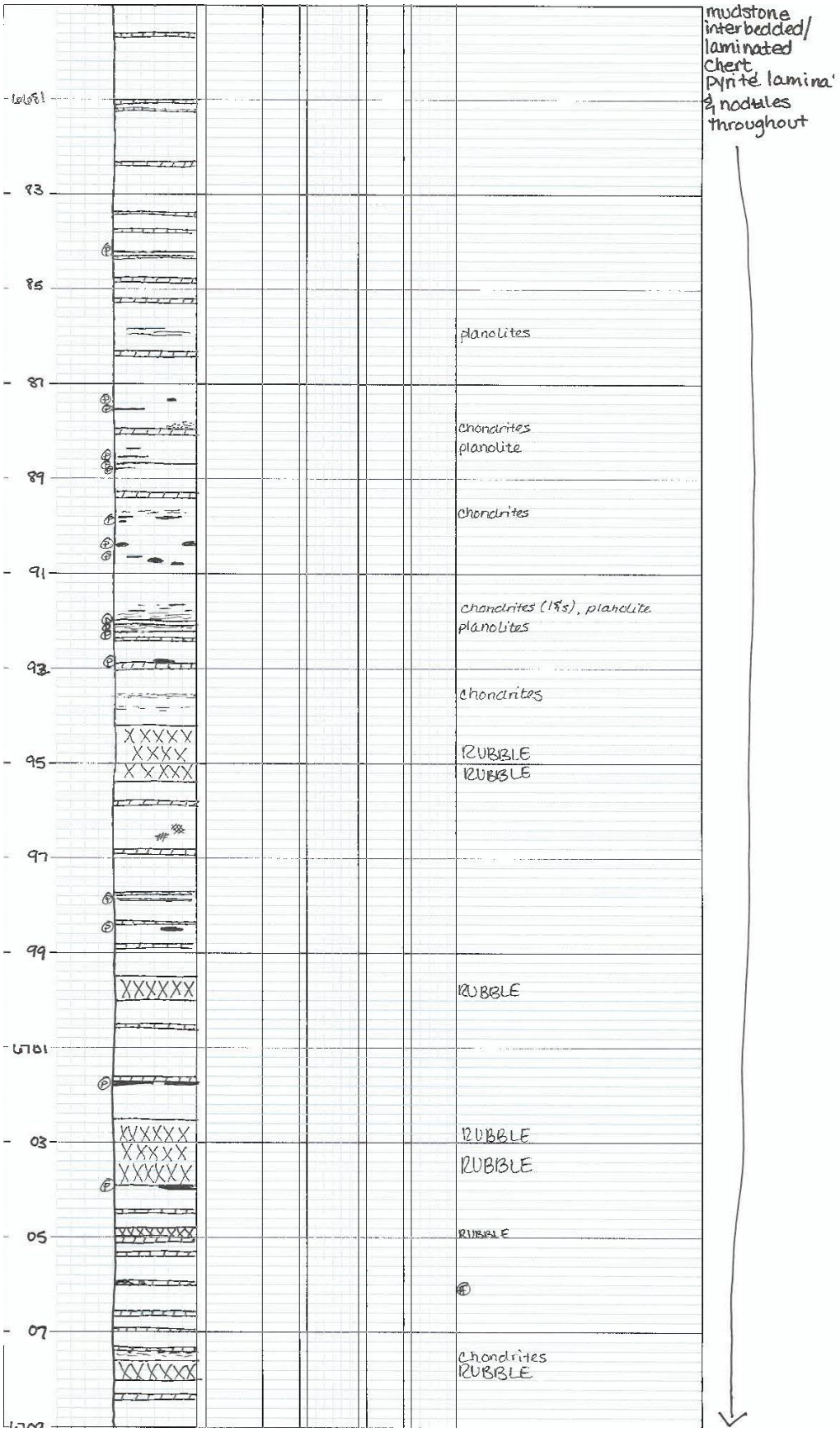
mudstone interbedded/ laminated chert pyrite lamina & nodules throughout
83
85
87
89
91
93
95
97
99
03
05
07
planolites
chondrites planolite
chondrites
chondrites (lgs), planolite planolites
chondrites
RUBBLE
RUBBLE
RUBBLE
RUBBLE
RUBBLE
RUBBLE
chondrites RUBBLE

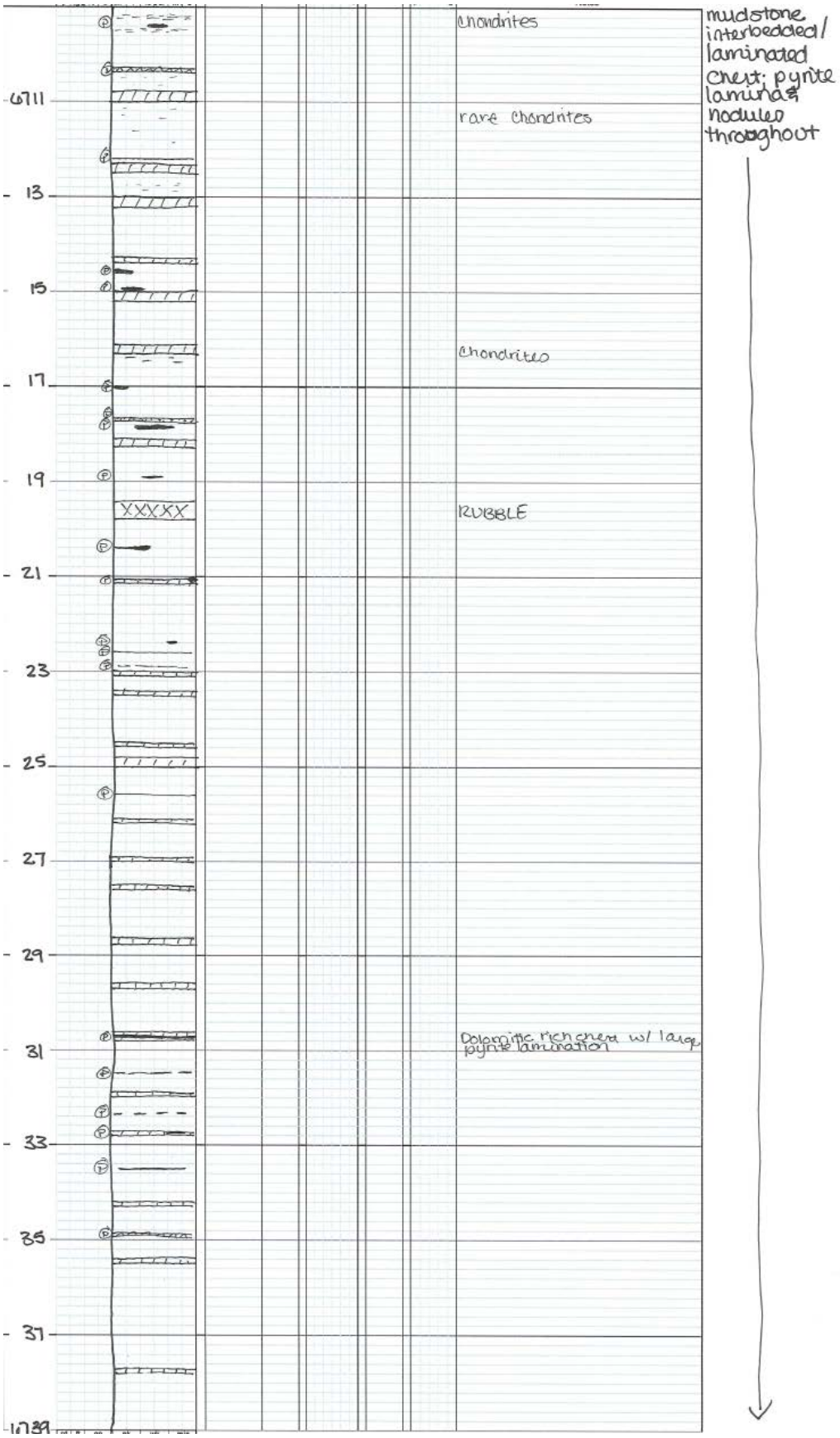
6711
13
15
17
19
21
23
25
27
29
31
33
35
37
1039
chondrites
rare chondrites
chondrites
RUBBLE
Dolomitic rich chert w/ large pyrite lamination
mudstone interbedded/ laminated chert; pyrite laminae & nodules throughout

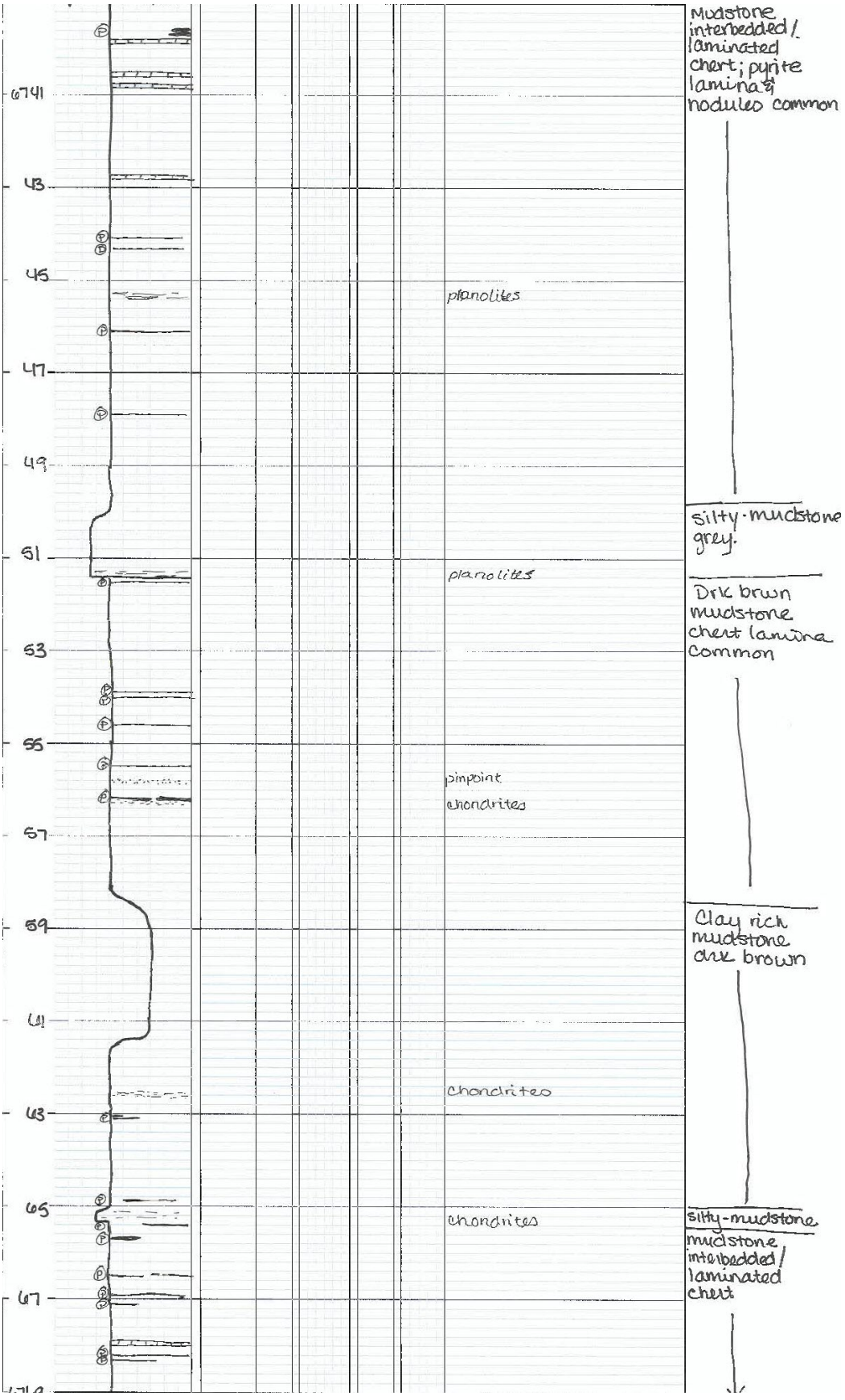
6741
43
45
47
49
51
53
55
57
59
61
63
65
67
planolites
planolites
pinpoint chondrites
chondrites
chondrites
Mudstone interbedded / laminated chert; pyrite lamina & nodules common
silty-mudstone grey.
Drk brown mudstone chert lamina common
Clay rich mudstone drk brown
silty-mudstone
mudstone interbedded / laminated chert

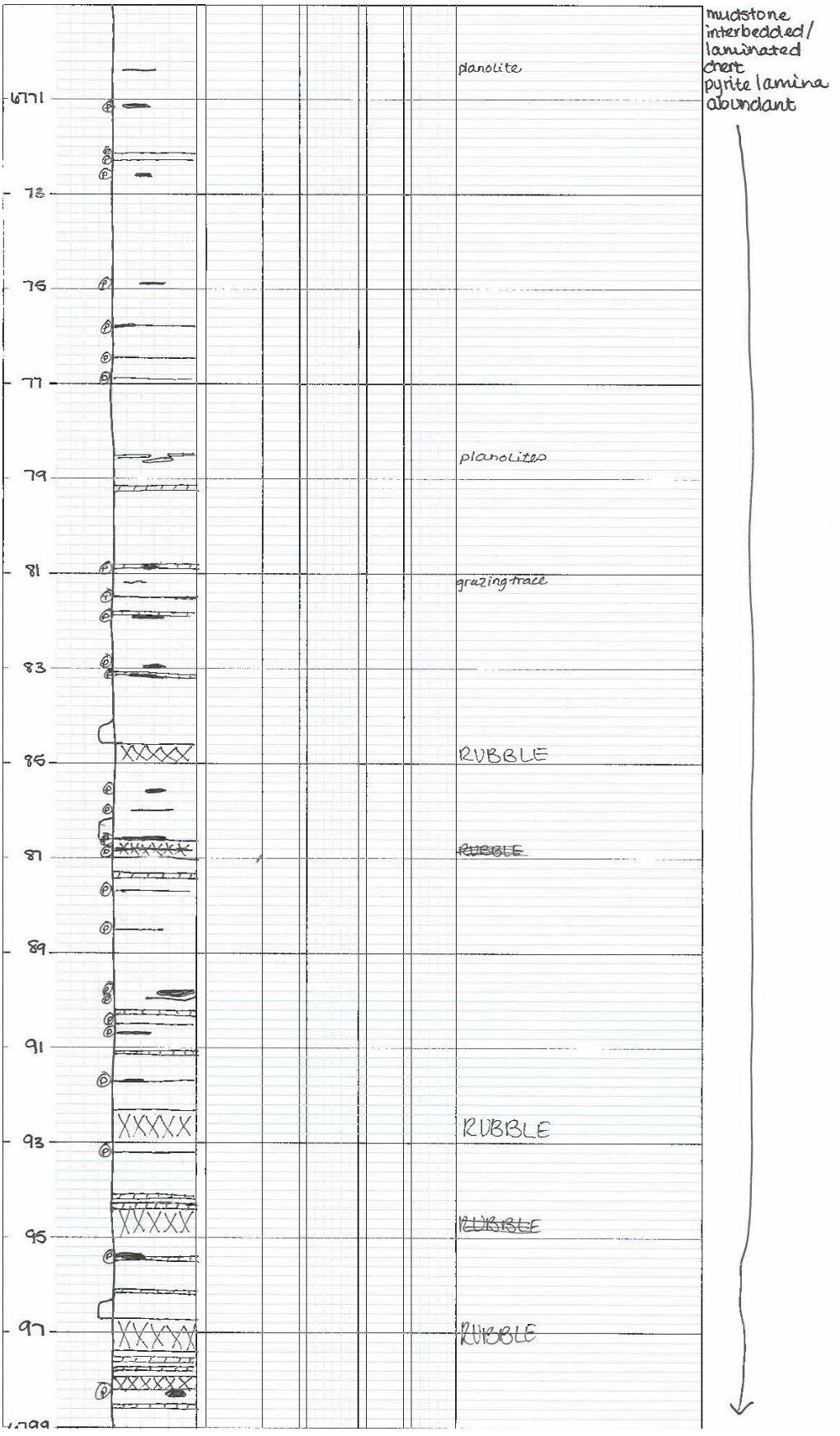
mudstone interbedded / laminated chert pyrite lamina abundant
6771
73
75
77
79
81
83
85
87
89
91
93
95
97
planolite
planolites
grazing trace
RUBBLE
RUBBLE
RUBBLE
RUBBLE
RUBBLE

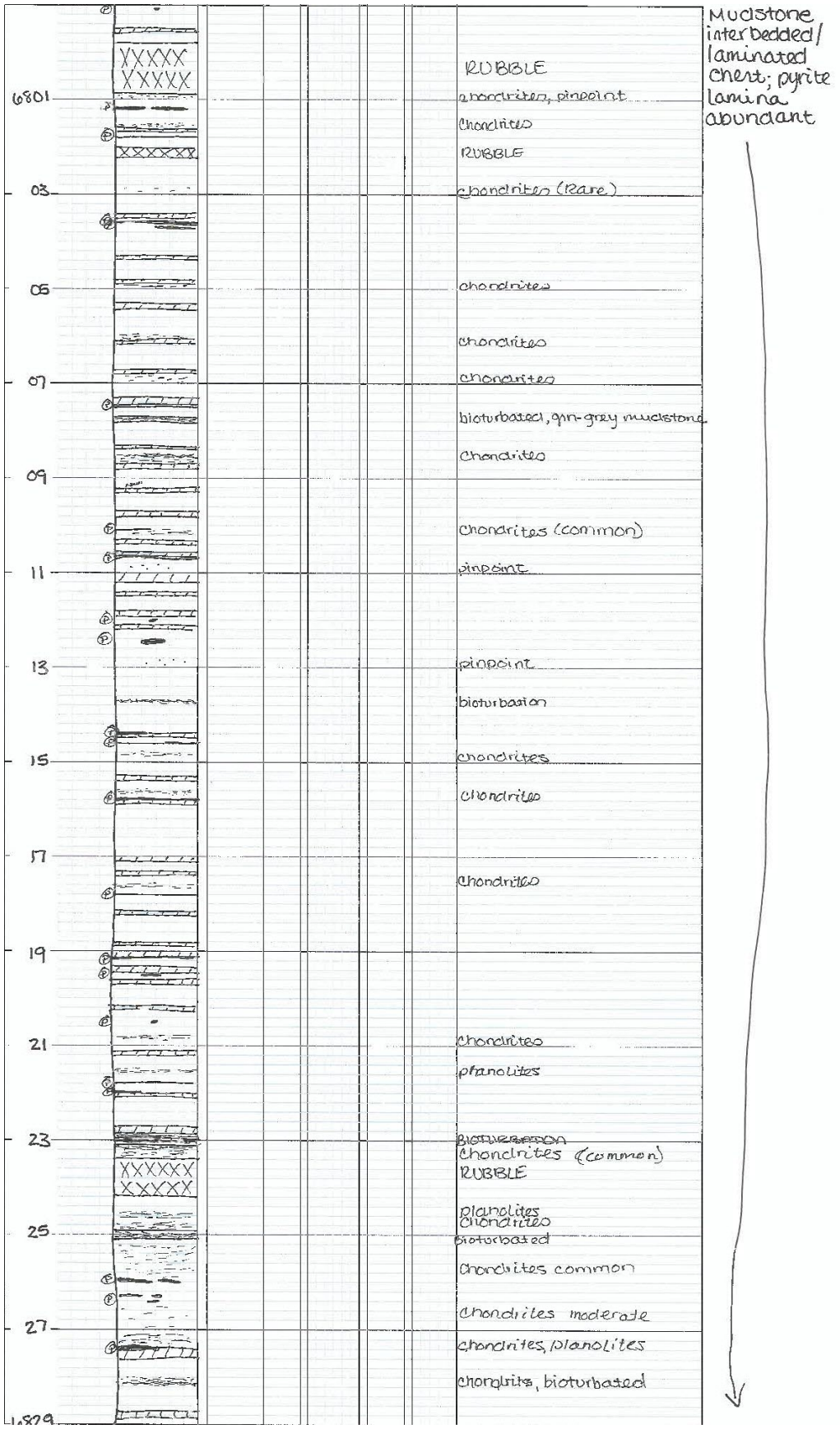
Mudstone interbedded/ laminated chert; pyrite lamina abundant
RUBBLE
chondrites, pinpoint
Chondrites
RUBBLE
chondrites (Rare)
chondrites
chondrites
chondrites
bioturbated, gry-grey mudstone
Chondrites
Chondrites (common)
pinpoint
pinpoint
bioturbation
chondrites
Chondrites
Chondrites
Chondrites
planolites
BIOTURBATION
Chondrites (common)
RUBBLE
planolites
Chondrites
Bioturbated
Chondrites common
Chondrites moderate
Chondrites, planolites
Chondrits, bioturbated
6801
03
05
07
09
11
13
15
17
19
21
23
25
27
6829

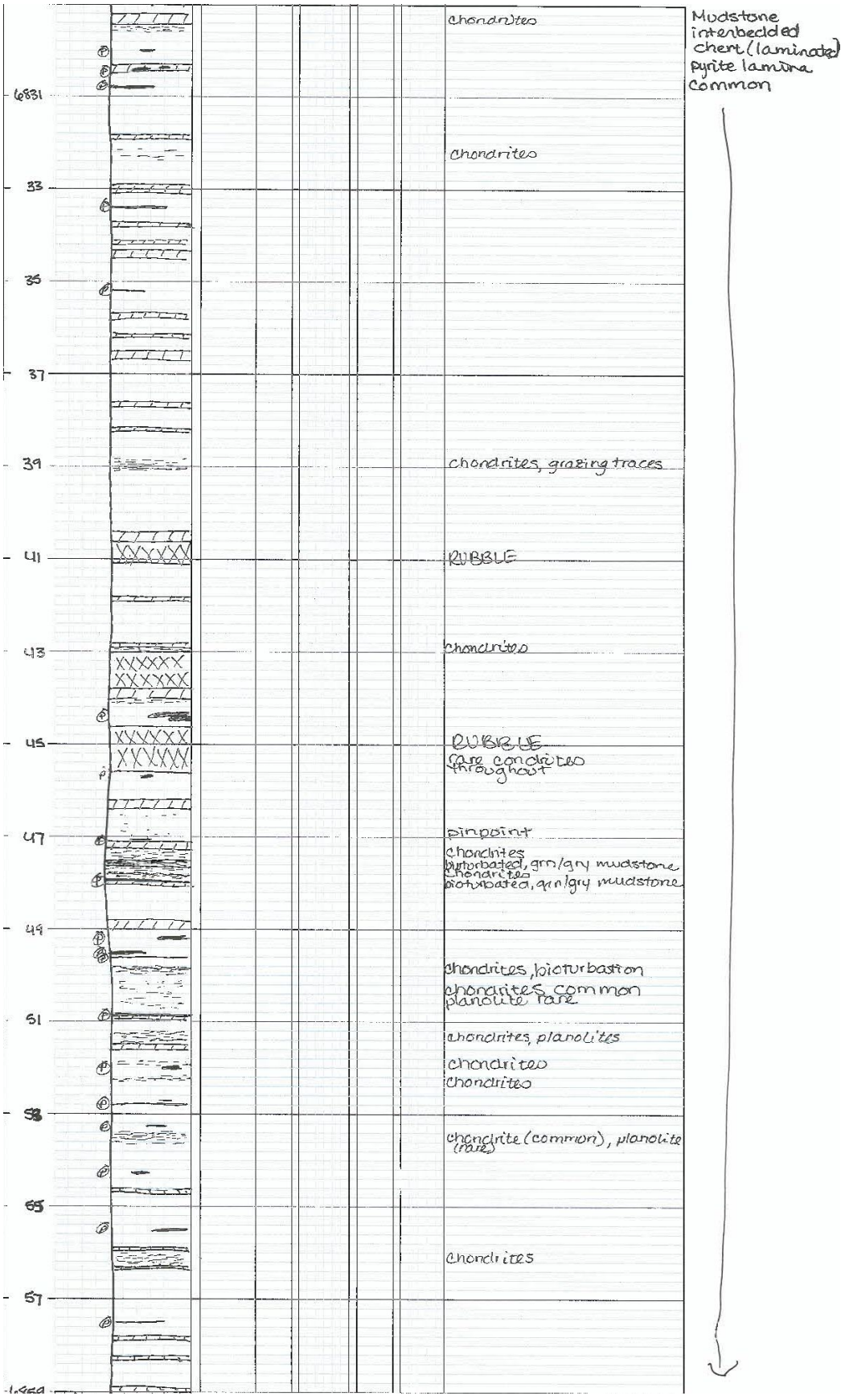
chondrites
Mudstone interbedded chert (laminated) pyrite lamina common
6831
chondrites
33
35
37
39
chondrites, grazing traces
41
RUBBLE
43
chondrites
45
RUBBLE
rare condrites throughout
47
pinpoint
chondrites
bioturbated, grn/gry mudstone
chondrites
bioturbated, grn/gry mudstone
49
chondrites, bioturbation
chondrites common
planolite rare
51
chondrites, planolites
chondrites
chondrites
53
chondrite (common), planolite (rare)
55
chondrites
57

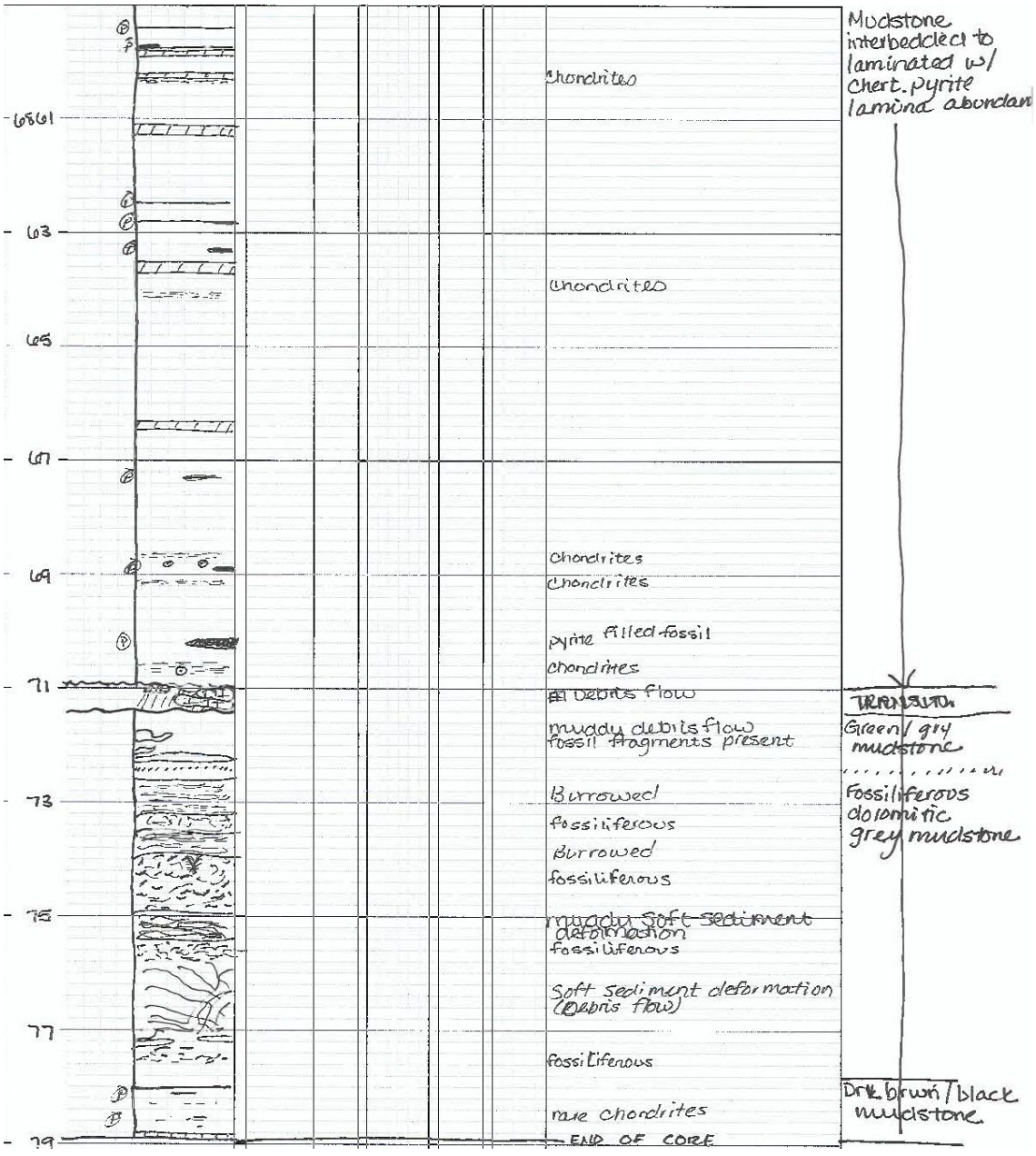
Mudstone interbedded to laminated w/ chert. pyrite lamina abundant
6861
63
65
67
69
71
73
75
77
79
Chondrites
Chondrites
Chondrites
Pyrite filled fossil
Chondrites
Debris flow
muddy debris flow
fossil fragments present
Burrowed
fossiliferous
Burrowed
fossiliferous
muddy soft sediment deformation
fossiliferous
Soft sediment deformation (debris flow)
fossiliferous
rare chondrites
END OF CORE
TRANSITION
Green/grey mudstone
Fossiliferous dolomitic grey mudstone
Drk. brown/black mudstone

APPENDIX D: CORE D CORE DESCRIPTION

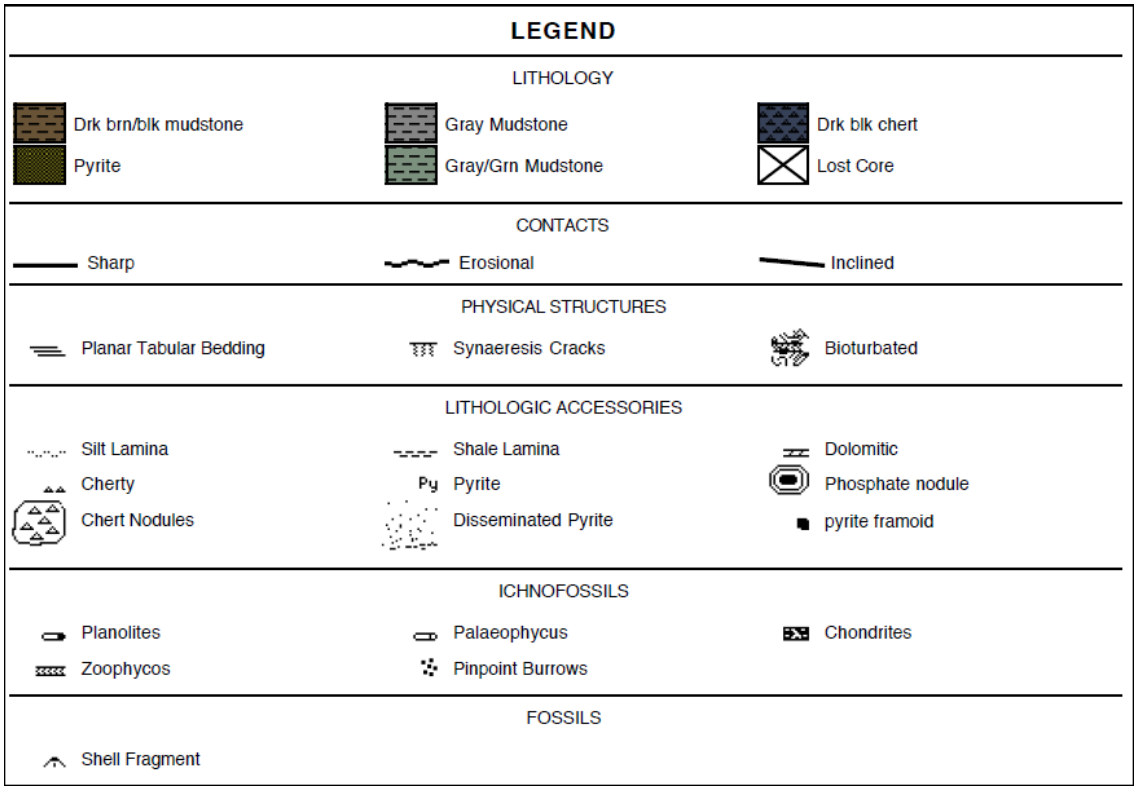

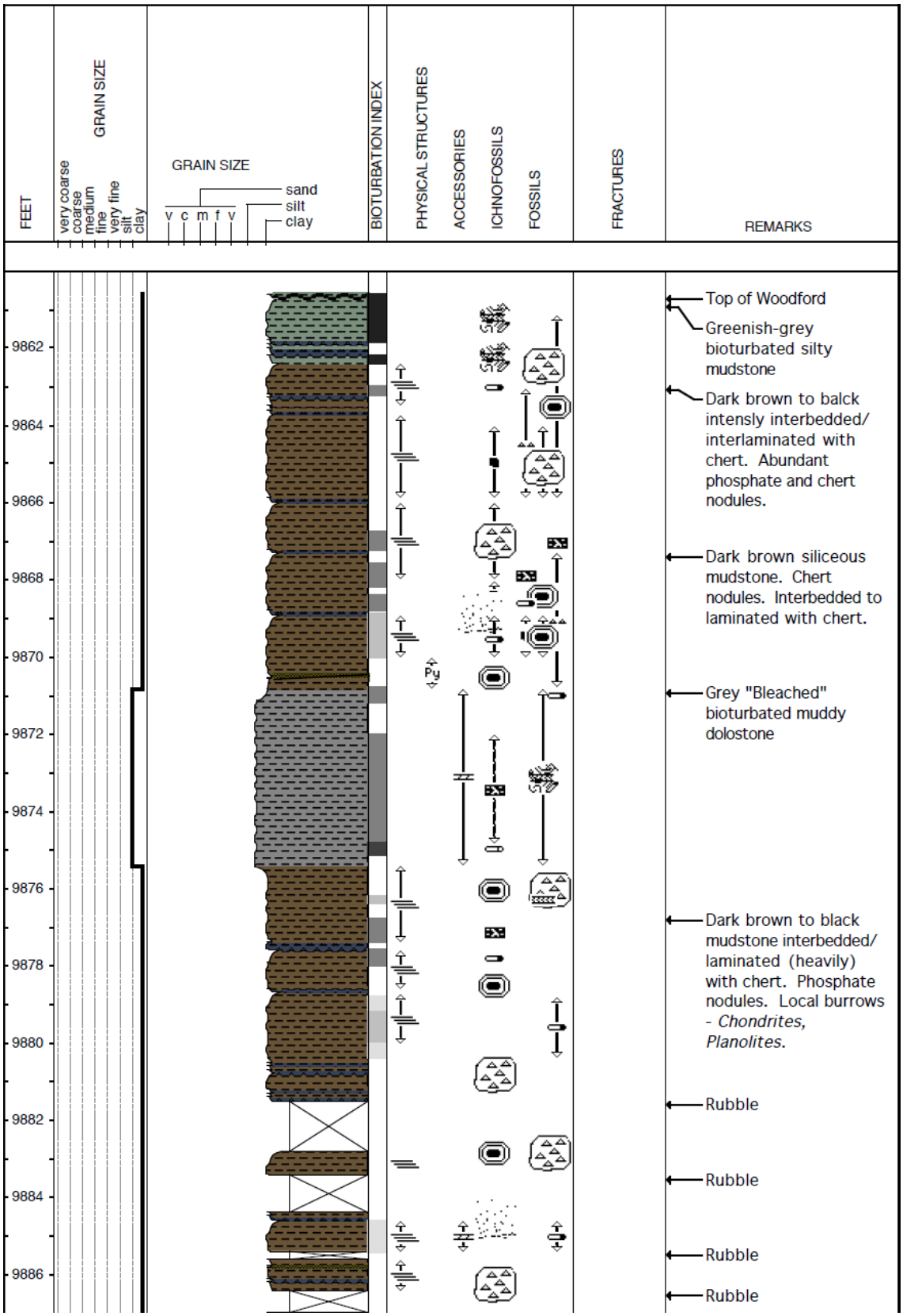
FEET
GRAIN SIZE
very coarse
coarse
medium
fine
very fine
silt
clay
GRAIN SIZE
v c m f v
sand
silt
clay
BIOTURBATION INDEX
PHYSICAL STRUCTURES
ACCESSORIES
ICHNOFOSSILS
FOSSILS
FRACTURES
REMARKS
9862
9864
9866
9868
9870
9872
9874
9876
9878
9880
9882
9884
9886
Py
Top of Woodford
Greenish-grey bioturbated silty mudstone
Dark brown to balck intensly interbedded/ interlaminated with chert. Abundant phosphate and chert nodules.
Dark brown siliceous mudstone. Chert nodules. Interbedded to laminated with chert.
Grey "Bleached" bioturbated muddy dolostone
Dark brown to black mudstone interbedded/ laminated (heavily) with chert. Phosphate nodules. Local burrows - Chondrites, Planolites.
Rubble
Rubble
Rubble
Rubble

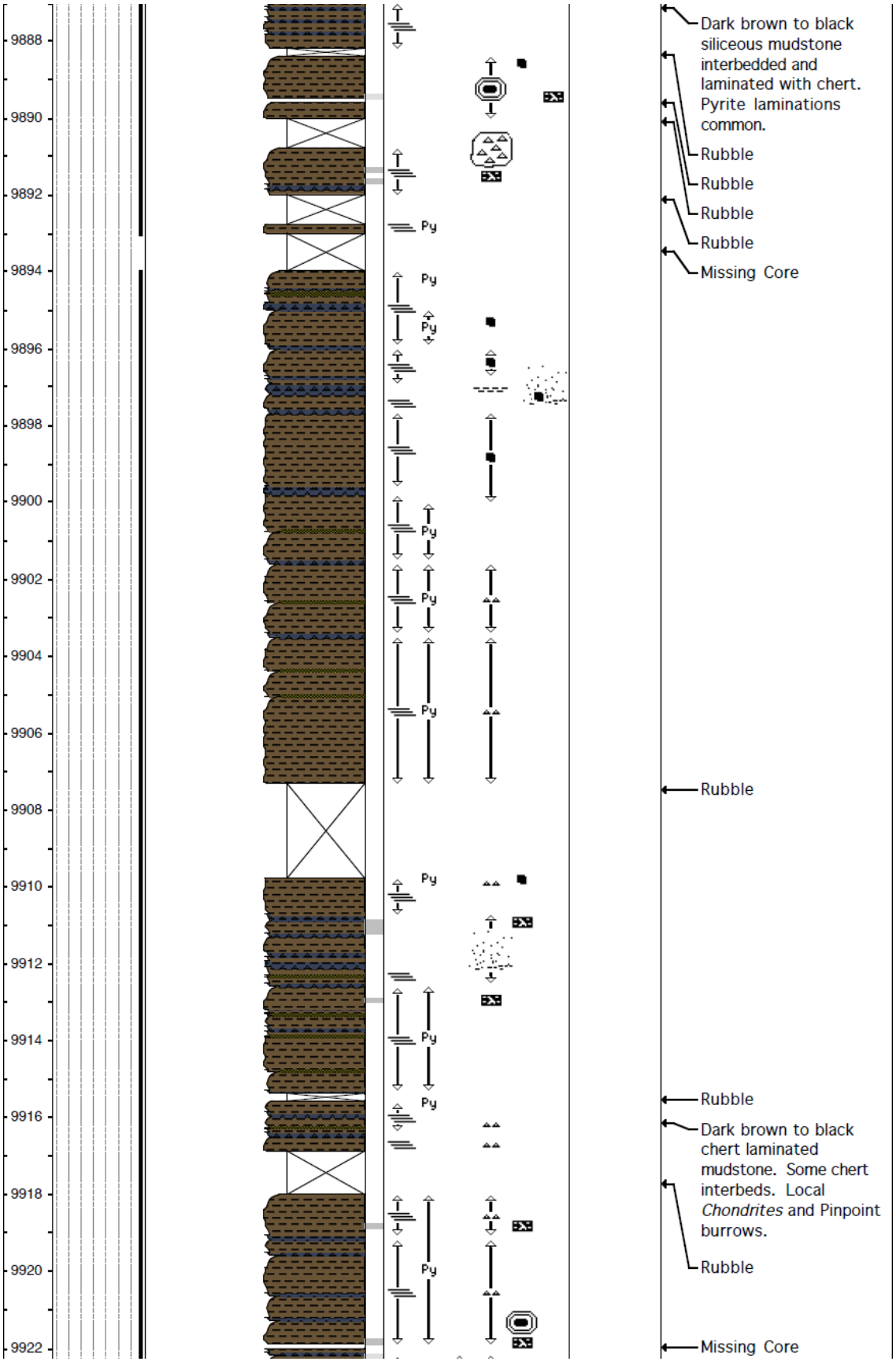
9888
9890
9892
9894
9896
9898
9900
9902
9904
9906
9908
9910
9912
9914
9916
9918
9920
9922
Py
Dark brown to black siliceous mudstone interbedded and laminated with chert. Pyrite laminations common.
Rubble
Rubble
Rubble
Rubble
Missing Core
Rubble
Rubble
Dark brown to black chert laminated mudstone. Some chert interbeds. Local *Chondrites* and Pinpoint burrows.
Rubble
Missing Core

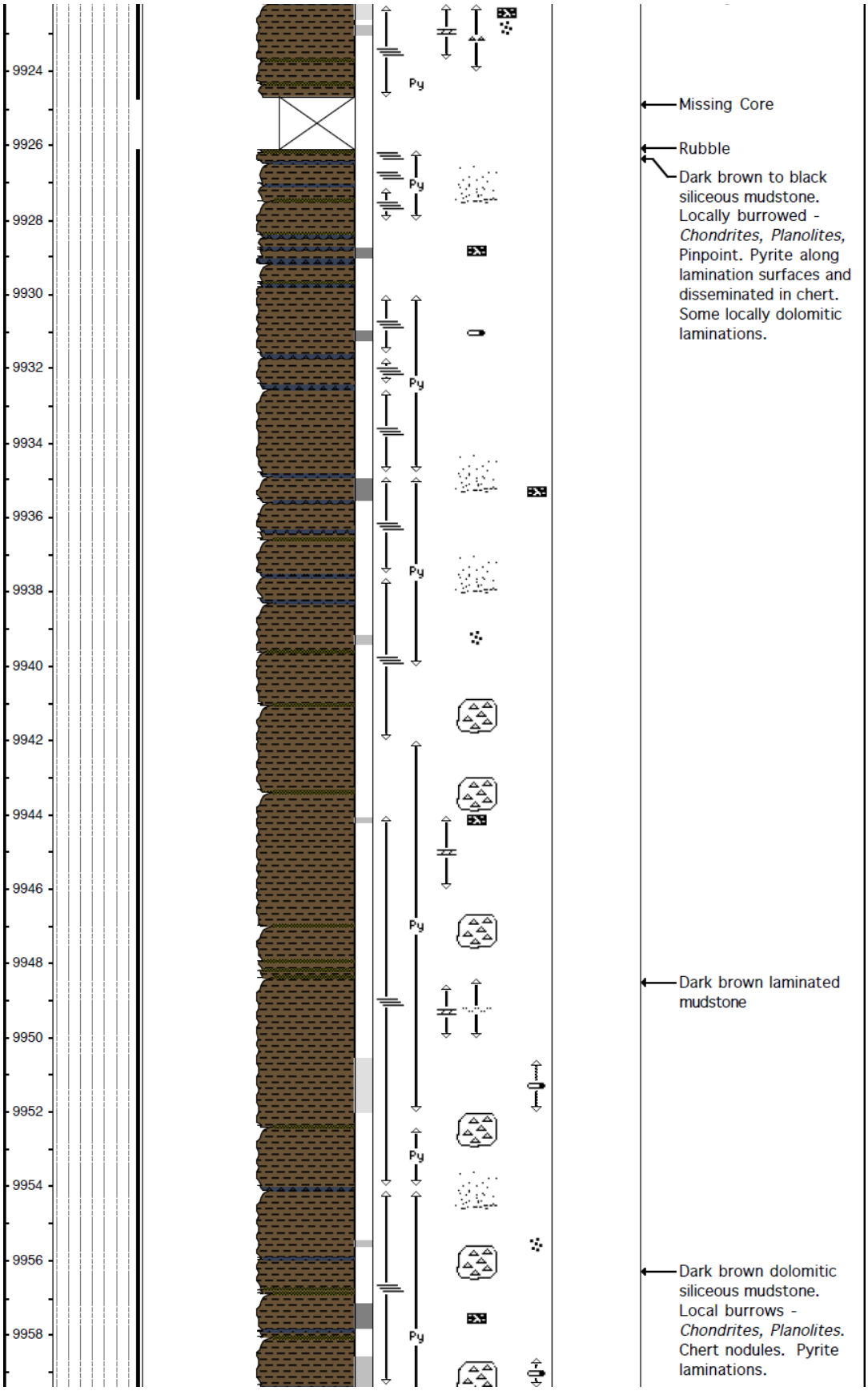
9924
9926
9928
9930
9932
9934
9936
9938
9940
9942
9944
9946
9948
9950
9952
9954
9956
9958
Py
Missing Core
Rubble
Dark brown to black siliceous mudstone. Locally burrowed - *Chondrites, Planolites,* Pinpoint. Pyrite along lamination surfaces and disseminated in chert. Some locally dolomitic laminations.
Dark brown laminated mudstone
Dark brown dolomitic siliceous mudstone. Local burrows - *Chondrites, Planolites.* Chert nodules. Pyrite laminations.

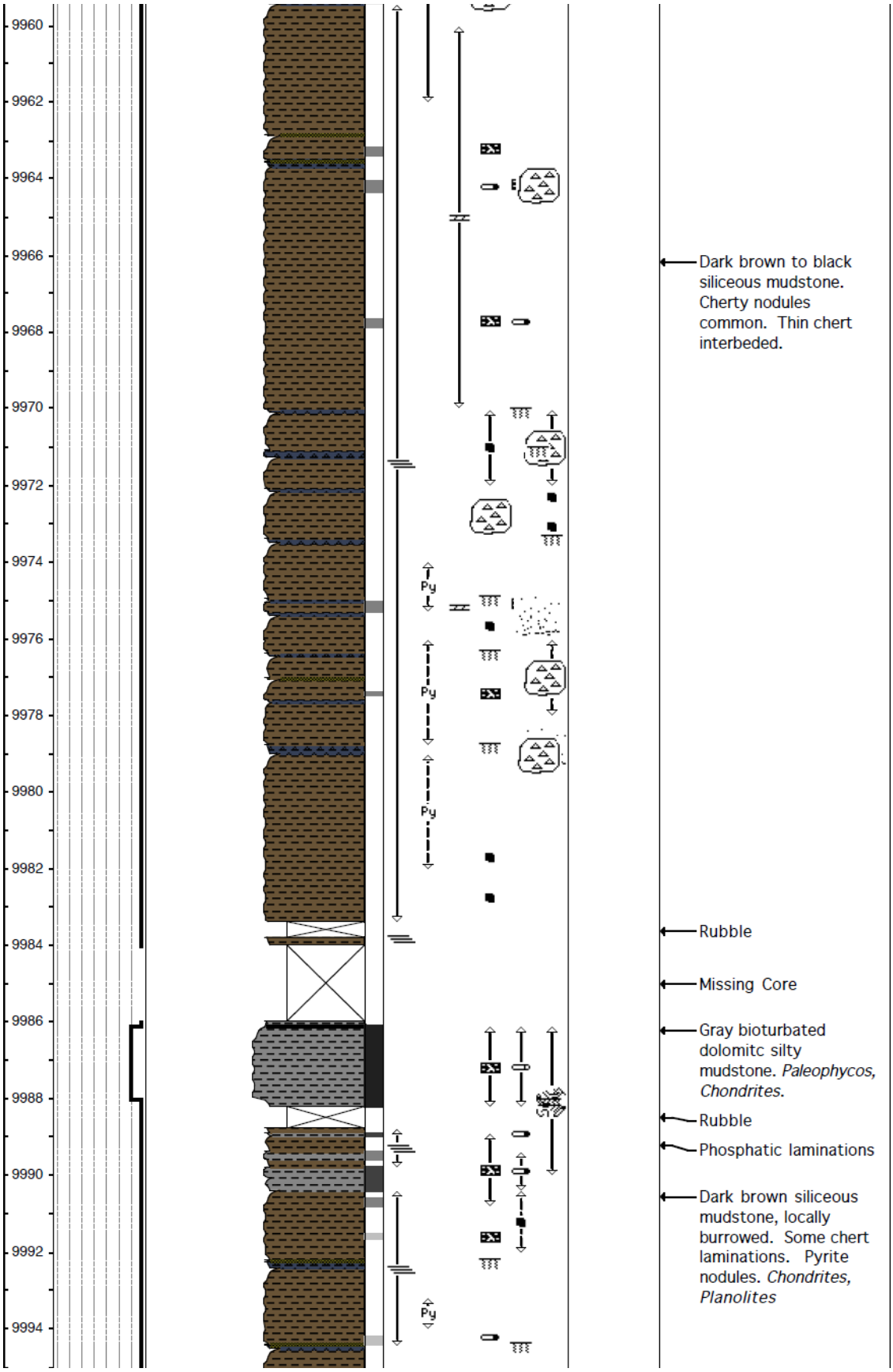
9960
9962
9964
9966
9968
9970
9972
9974
9976
9978
9980
9982
9984
9986
9988
9990
9992
9994
Py
Py
Py
Py
Dark brown to black siliceous mudstone. Cherty nodules common. Thin chert interbeded.
Rubble
Missing Core
Gray bioturbated dolomitc silty mudstone. Paleophycos, Chondrites.
Rubble
Phosphatic laminations
Dark brown siliceous mudstone, locally burrowed. Some chert laminations. Pyrite nodules. Chondrites, Planolites

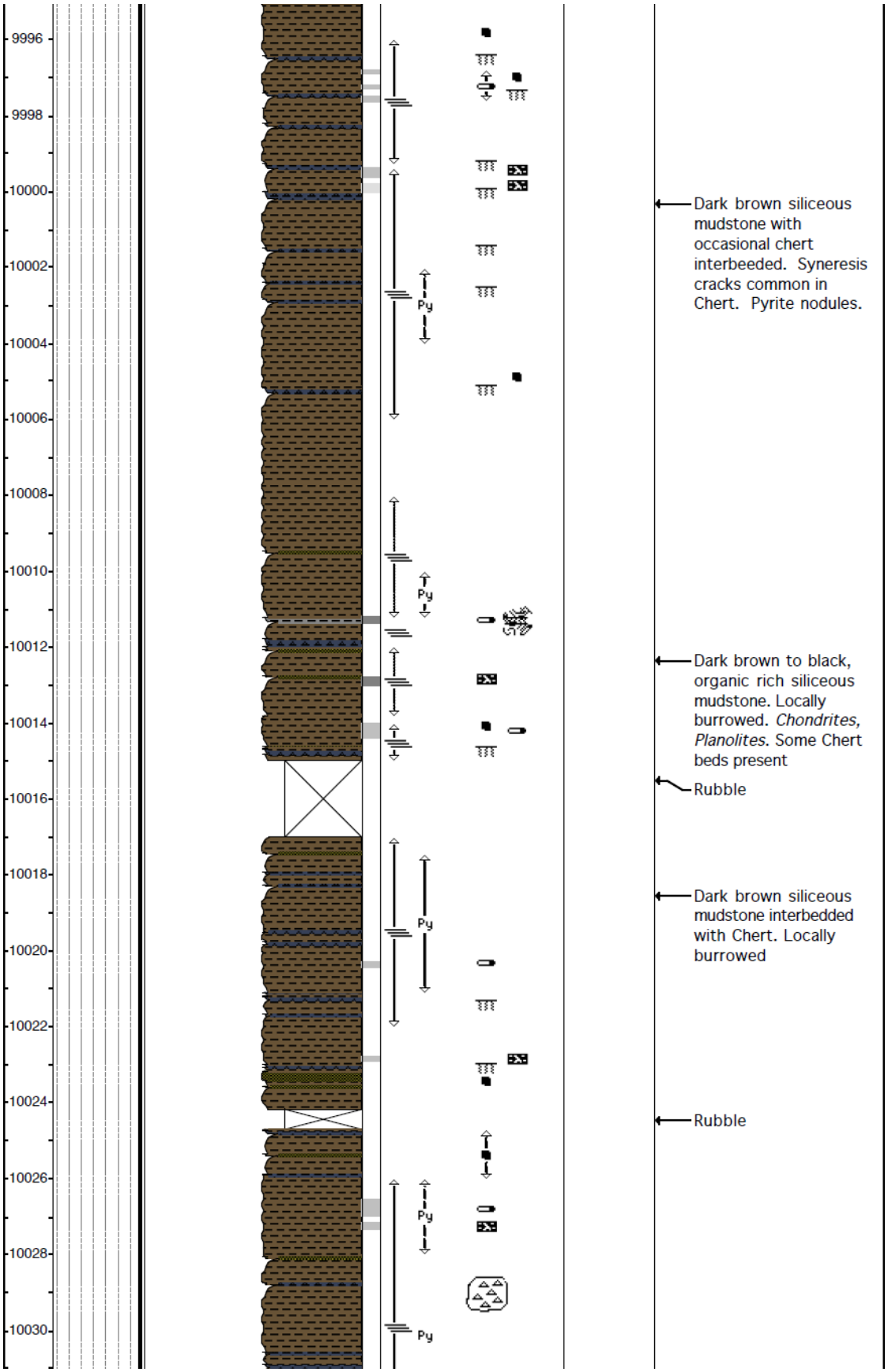
9996
9998
10000
10002
10004
10006
10008
10010
10012
10014
10016
10018
10020
10022
10024
10026
10028
10030
Py
Py
Py
Py
Py
Dark brown siliceous mudstone with occasional chert interbeeded. Syneresis cracks common in Chert. Pyrite nodules.
Dark brown to black, organic rich siliceous mudstone. Locally burrowed. Chondrites, Planolites. Some Chert beds present
Rubble
Dark brown siliceous mudstone interbedded with Chert. Locally burrowed
Rubble

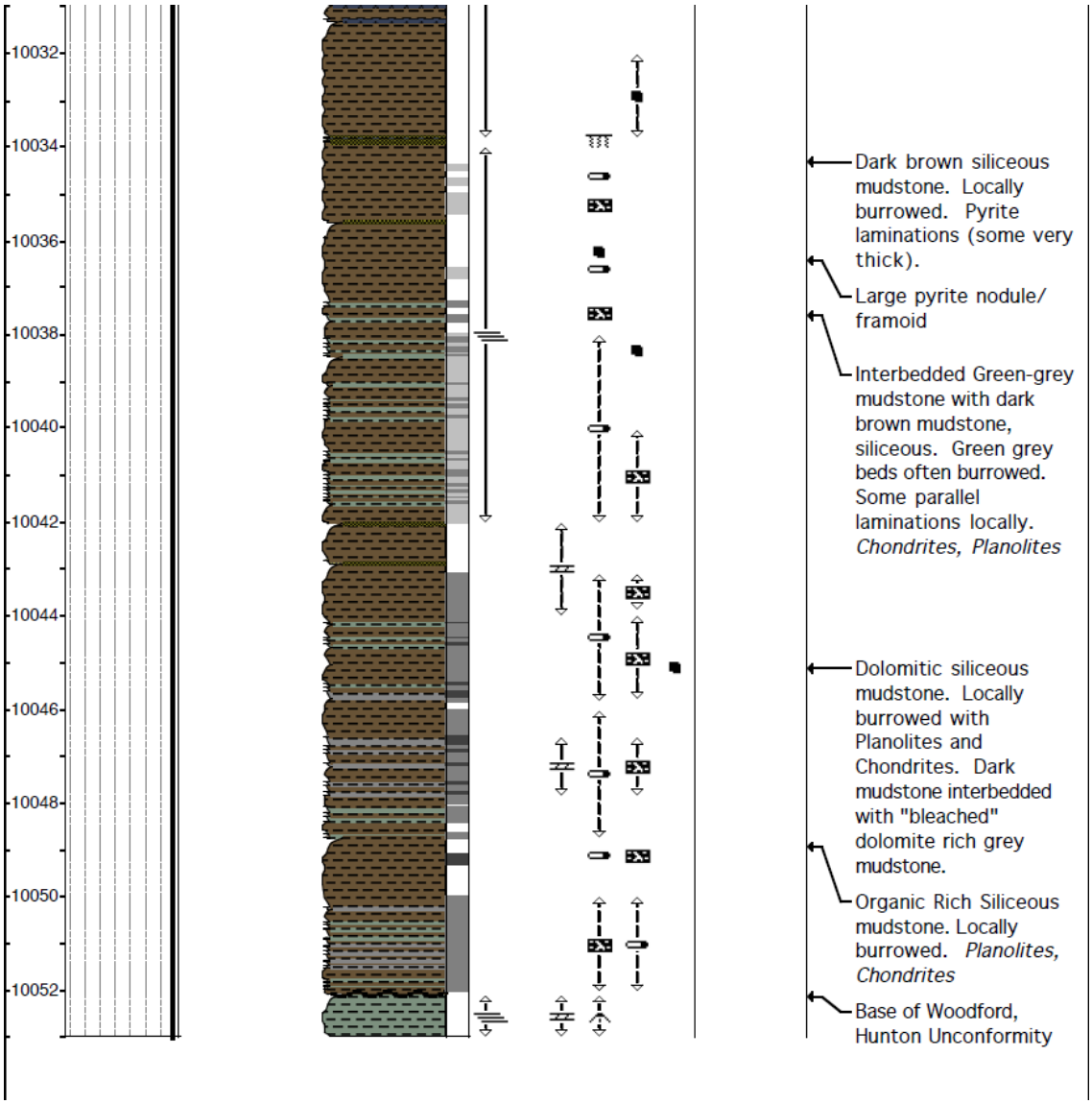
10032
10034
10036
10038
10040
10042
10044
10046
10048
10050
10052
Dark brown siliceous mudstone. Locally burrowed. Pyrite laminations (some very thick).
Large pyrite nodule/ framoid
Interbedded Green-grey mudstone with dark brown mudstone, siliceous. Green grey beds often burrowed. Some parallel laminations locally. Chondrites, Planolites
Dolomitic siliceous mudstone. Locally burrowed with Planolites and Chondrites. Dark mudstone interbedded with "bleached" dolomite rich grey mudstone.
Organic Rich Siliceous mudstone. Locally burrowed. Planolites, Chondrites
Base of Woodford, Hunton Unconformity

APPENDIX E: CORE D XRF CHART

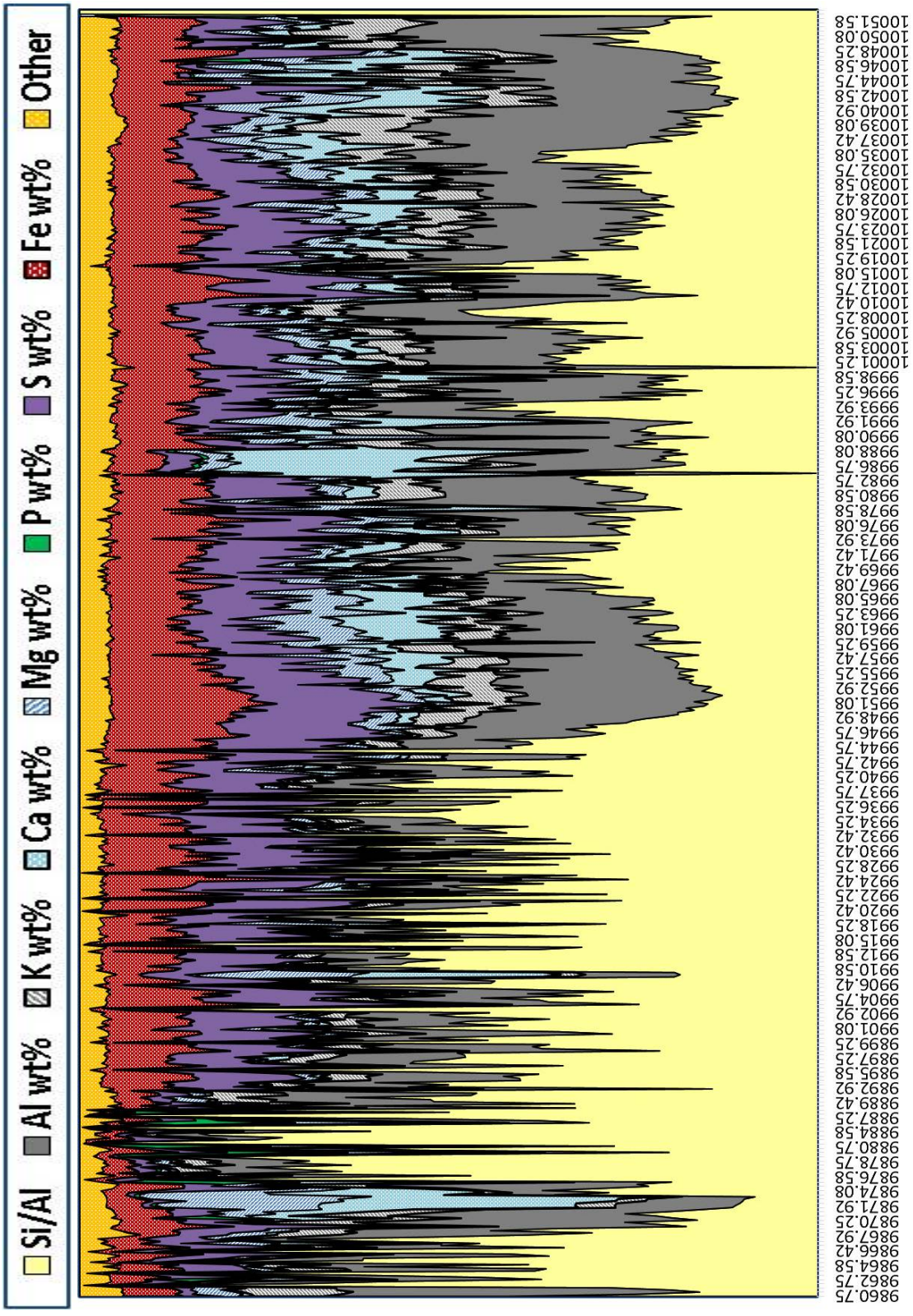

APPENDIX F: CORE E CORE DESCRIPTION

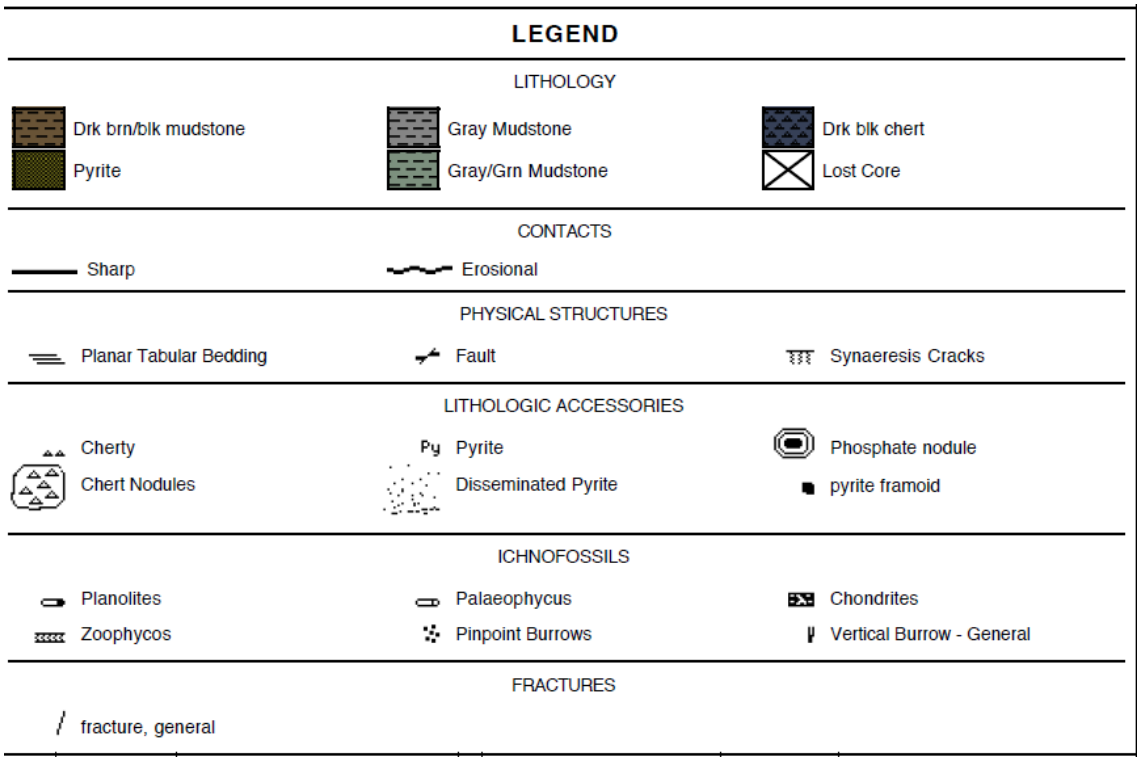

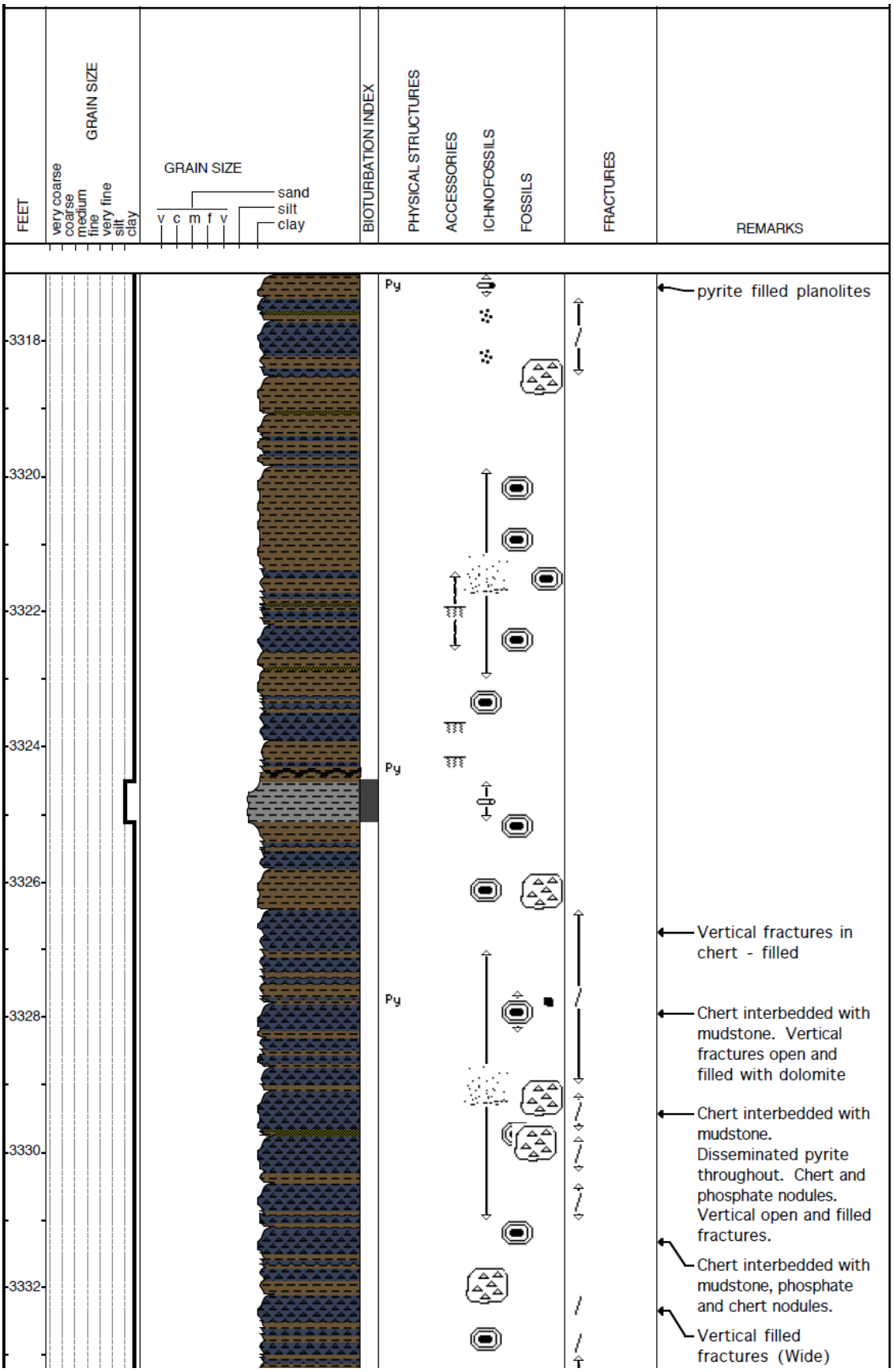
FEET
GRAIN SIZE
very coarse
coarse
medium
fine
very fine
silt
clay
GRAIN SIZE
v c m f v
sand
silt
clay
BIOTURBATION INDEX
PHYSICAL STRUCTURES
ACCESSORIES
ICHNOFOSSILS
FOSSILS
FRACTURES
REMARKS
3318
3320
3322
3324
3326
3328
3330
3332
Py
Py
Py
pyrite filled planolites
Vertical fractures in chert - filled
Chert interbedded with mudstone. Vertical fractures open and filled with dolomite
Chert interbedded with mudstone. Disseminated pyrite throughout. Chert and phosphate nodules. Vertical open and filled fractures.
Chert interbedded with mudstone, phosphate and chert nodules.
Vertical filled fractures (Wide)

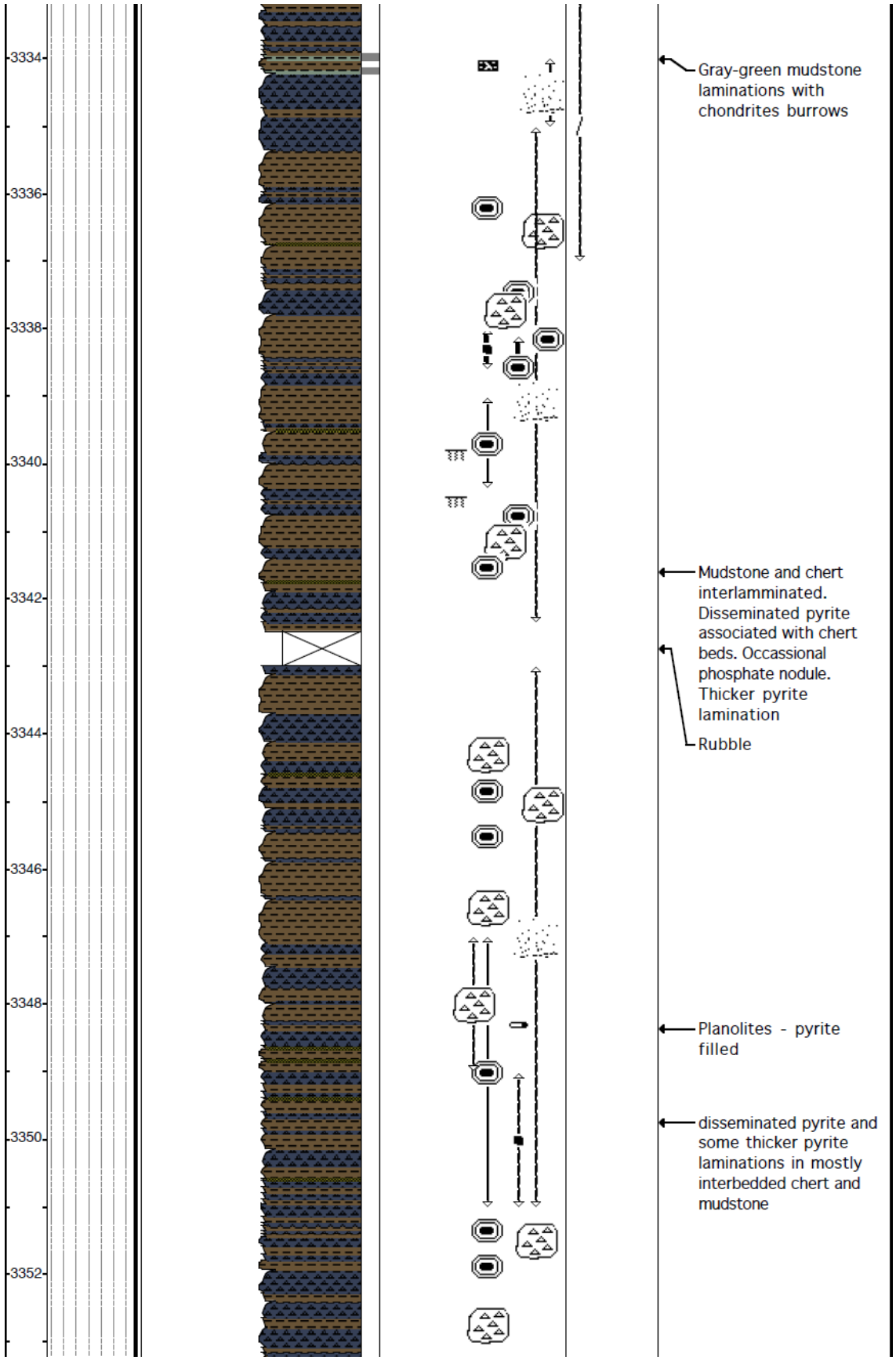
3334
3336
3338
3340
3342
3344
3346
3348
3350
3352
Gray-green mudstone laminations with chondrites burrows
Mudstone and chert interlamminated. Disseminated pyrite associated with chert beds. Occassional phosphate nodule. Thicker pyrite lamination
Rubble
Planolites - pyrite filled
disseminated pyrite and some thicker pyrite laminations in mostly interbedded chert and mudstone

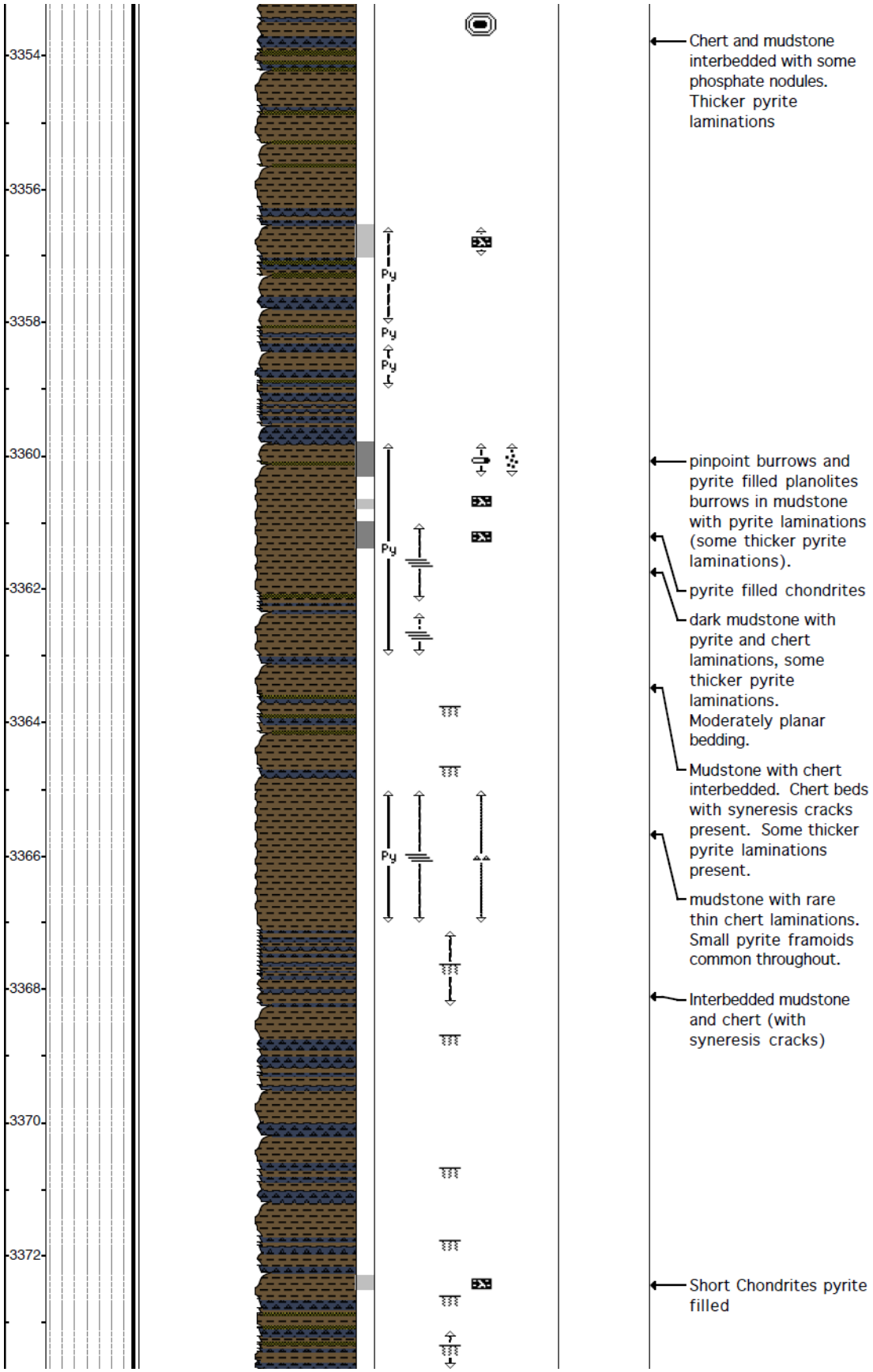
3354
3356
3358
3360
3362
3364
3366
3368
3370
3372
Py
Py
Py
Py
Py
Chert and mudstone interbedded with some phosphate nodules. Thicker pyrite laminations
pinpoint burrows and pyrite filled planolites burrows in mudstone with pyrite laminations (some thicker pyrite laminations).
pyrite filled chondrites
dark mudstone with pyrite and chert laminations, some thicker pyrite laminations. Moderately planar bedding.
Mudstone with chert interbedded. Chert beds with syneresis cracks present. Some thicker pyrite laminations present.
mudstone with rare thin chert laminations. Small pyrite framoids common throughout.
Interbedded mudstone and chert (with syneresis cracks)
Short Chondrites pyrite filled

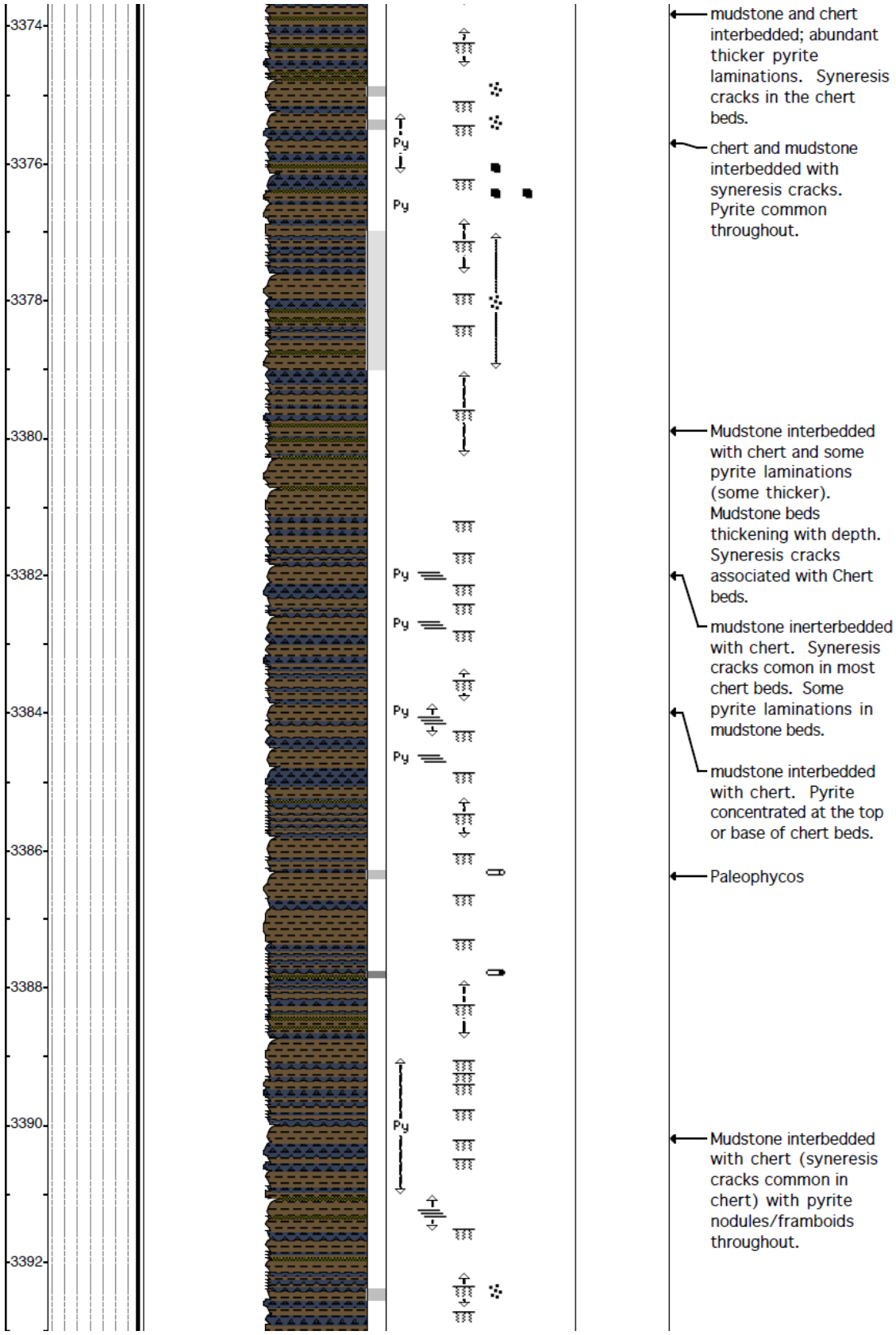
3374
3376
3378
3380
3382
3384
3386
3388
3390
3392
Py
Py
Py
Py
Py
Py
Py
mudstone and chert interbedded; abundant thicker pyrite laminations. Syneresis cracks in the chert beds.
chert and mudstone interbedded with syneresis cracks. Pyrite common throughout.
Mudstone interbedded with chert and some pyrite laminations (some thicker). Mudstone beds thickening with depth. Syneresis cracks associated with Chert beds.
mudstone inerterbedded with chert. Syneresis cracks comon in most chert beds. Some pyrite laminations in mudstone beds.
mudstone interbedded with chert. Pyrite concentrated at the top or base of chert beds.
Paleophycos
Mudstone interbedded with chert (syneresis cracks common in chert) with pyrite nodules/framboids throughout.

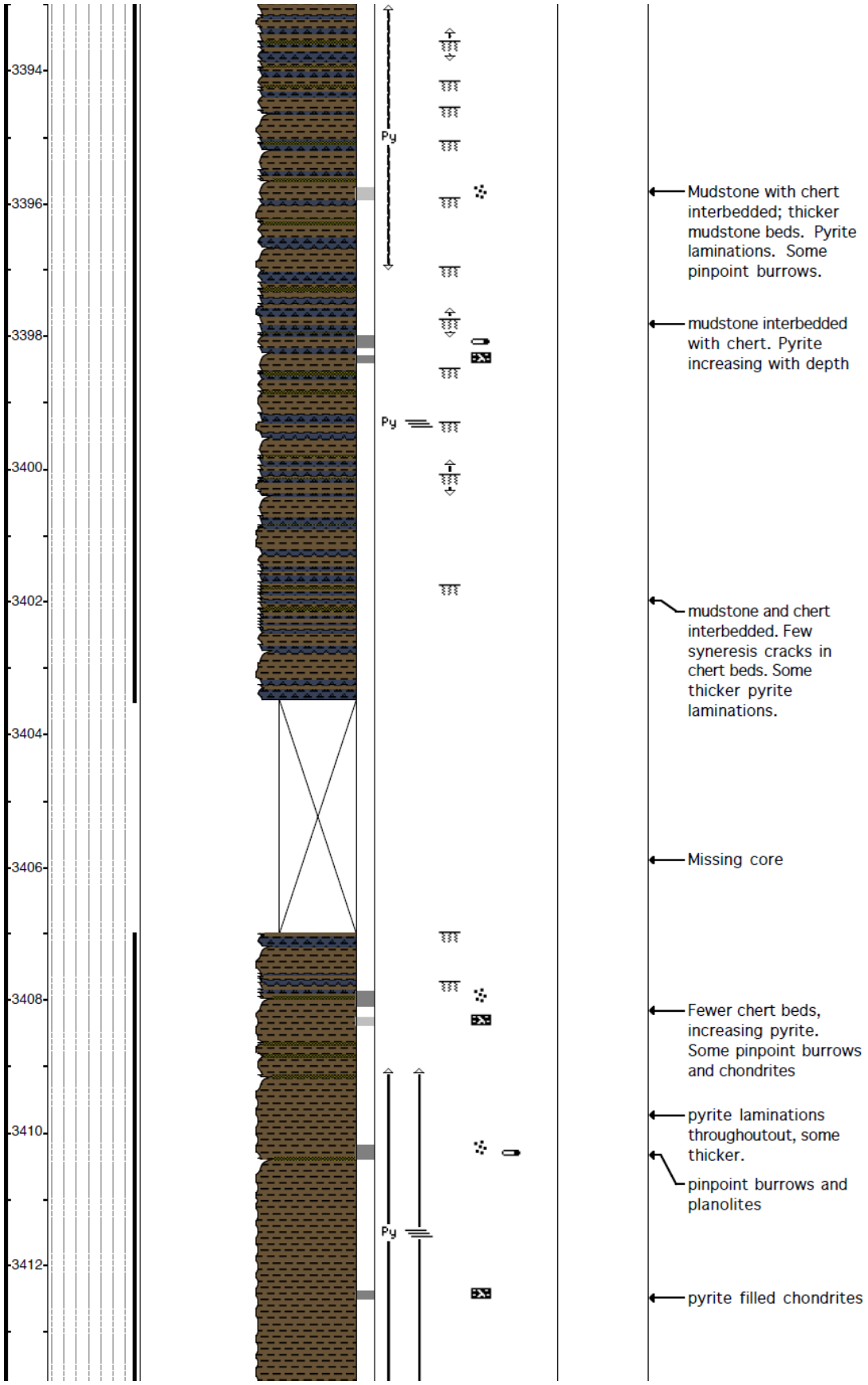
3394
3396
3398
3400
3402
3404
3406
3408
3410
3412
Py
Py
Py
Mudstone with chert interbedded; thicker mudstone beds. Pyrite laminations. Some pinpoint burrows.
mudstone interbedded with chert. Pyrite increasing with depth
mudstone and chert interbedded. Few syneresis cracks in chert beds. Some thicker pyrite laminations.
Missing core
Fewer chert beds, increasing pyrite. Some pinpoint burrows and chondrites
pyrite laminations throughoutout, some thicker.
pinpoint burrows and planolites
pyrite filled chondrites

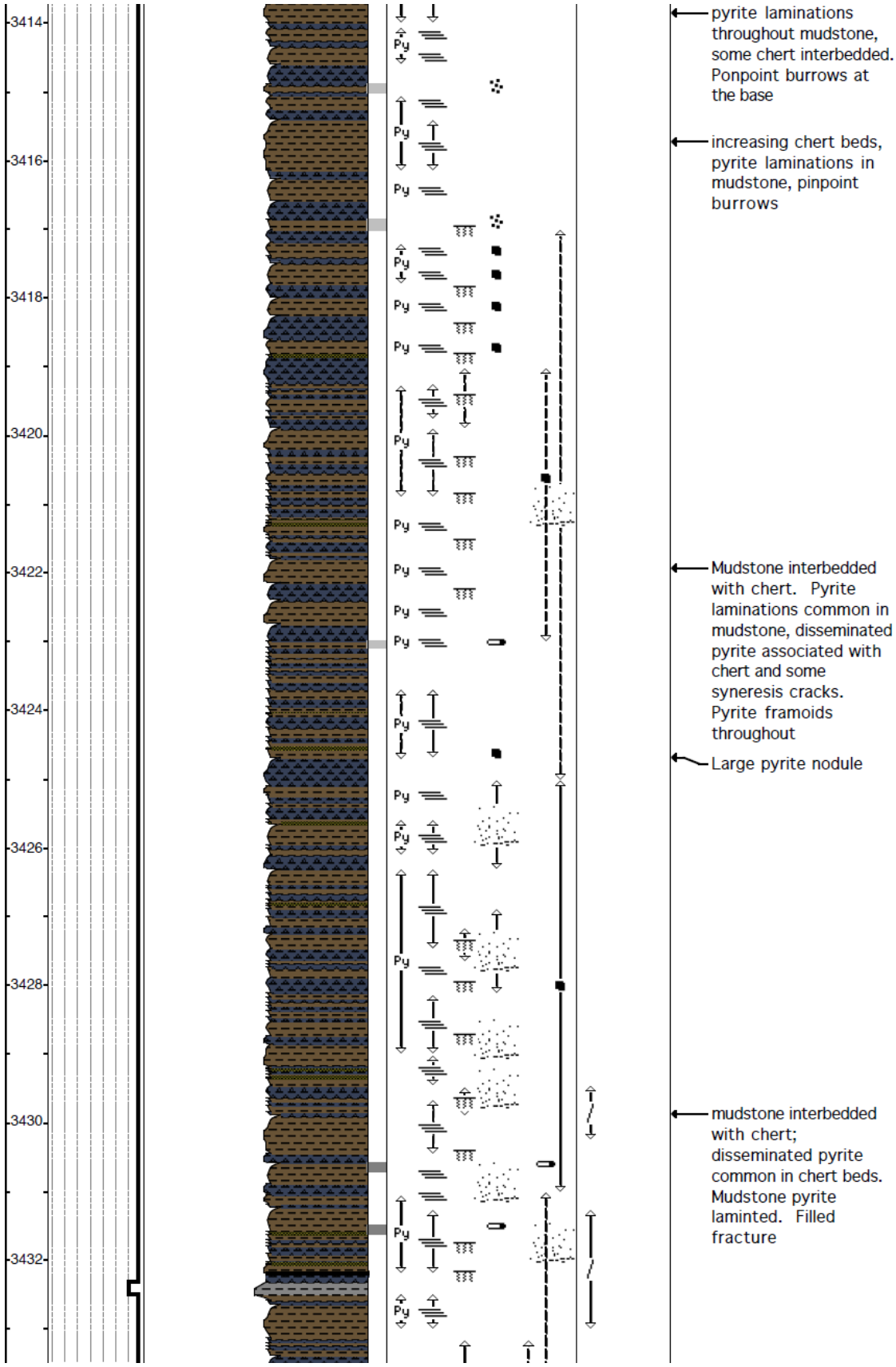
3414
3416
3418
3420
3422
3424
3426
3428
3430
3432
Py
pyrite laminations throughout mudstone, some chert interbedded. Ponpoint burrows at the base
increasing chert beds, pyrite laminations in mudstone, pinpoint burrows
Mudstone interbedded with chert. Pyrite laminations common in mudstone, disseminated pyrite associated with chert and some syneresis cracks. Pyrite framoids throughout
Large pyrite nodule
mudstone interbedded with chert; disseminated pyrite common in chert beds. Mudstone pyrite laminted. Filled fracture

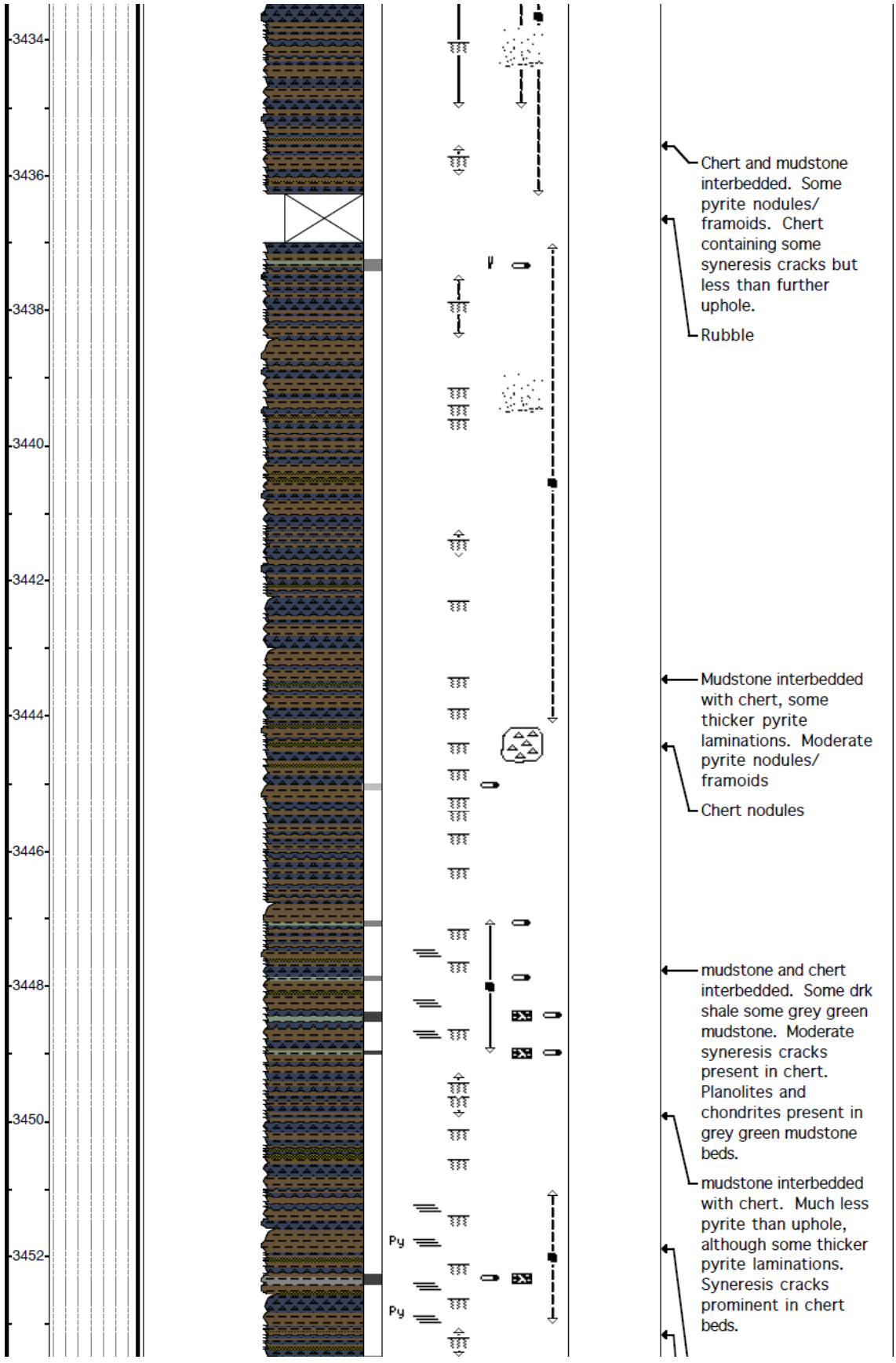
3434
3436
3438
3440
3442
3444
3446
3448
3450
3452
Py
Py
Chert and mudstone interbedded. Some pyrite nodules/ framoids. Chert containing some syneresis cracks but less than further uphole.
Rubble
Mudstone interbedded with chert, some thicker pyrite laminations. Moderate pyrite nodules/ framoids
Chert nodules
mudstone and chert interbedded. Some drk shale some grey green mudstone. Moderate syneresis cracks present in chert. Planolites and chondrites present in grey green mudstone beds.
mudstone interbedded with chert. Much less pyrite than uphole, although some thicker pyrite laminations. Syneresis cracks prominent in chert beds.

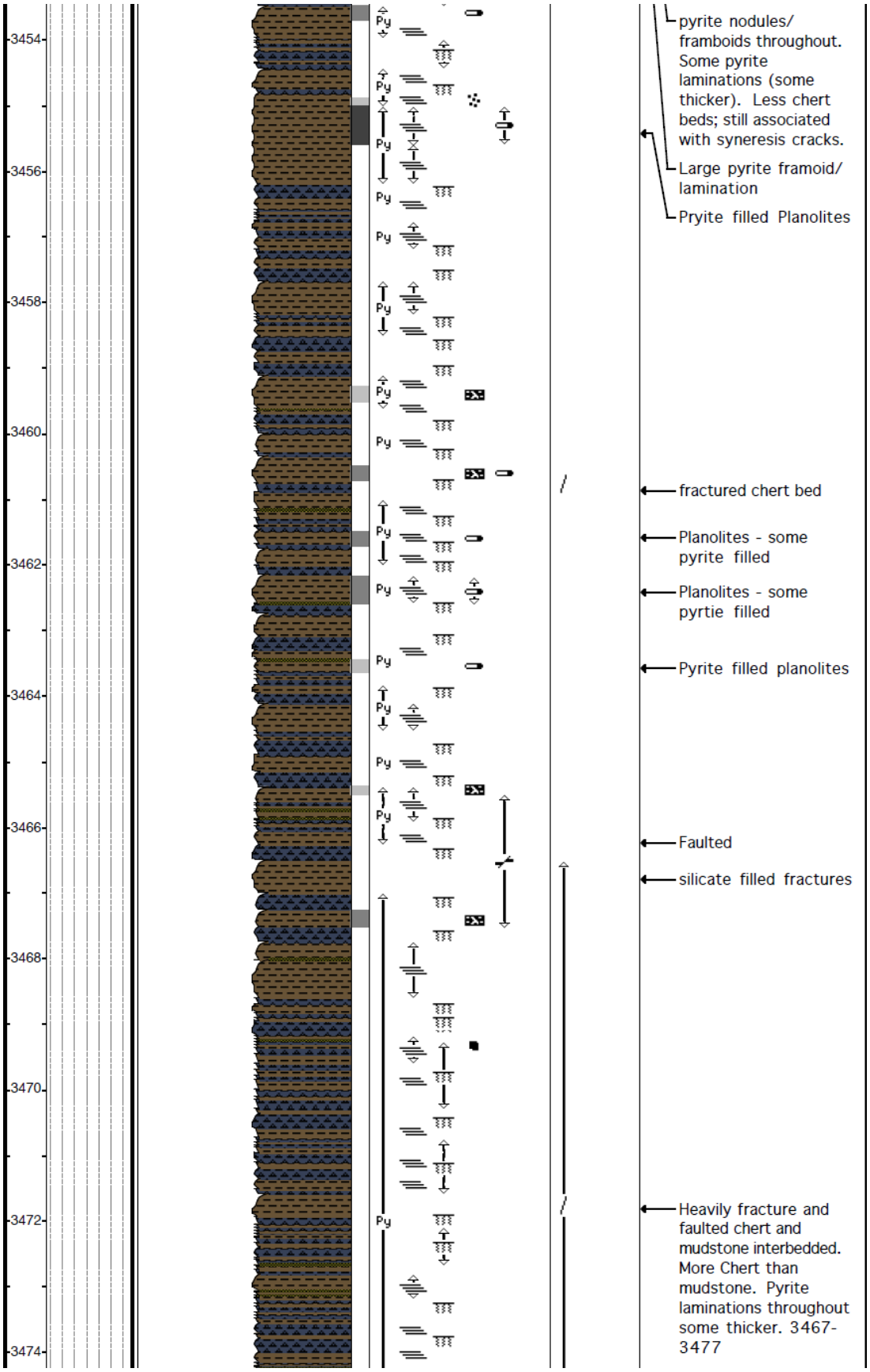
3454
3456
3458
3460
3462
3464
3466
3468
3470
3472
3474
Py
pyrite nodules/ framboids throughout. Some pyrite laminations (some thicker). Less chert beds; still associated with syneresis cracks.
Large pyrite framoid/ lamination
Pryite filled Planolites
fractured chert bed
Planolites - some pyrite filled
Planolites - some pyrtie filled
Pyrite filled planolites
Faulted
silicate filled fractures
Heavily fracture and faulted chert and mudstone interbedded. More Chert than mudstone. Pyrite laminations throughout some thicker. 3467-3477

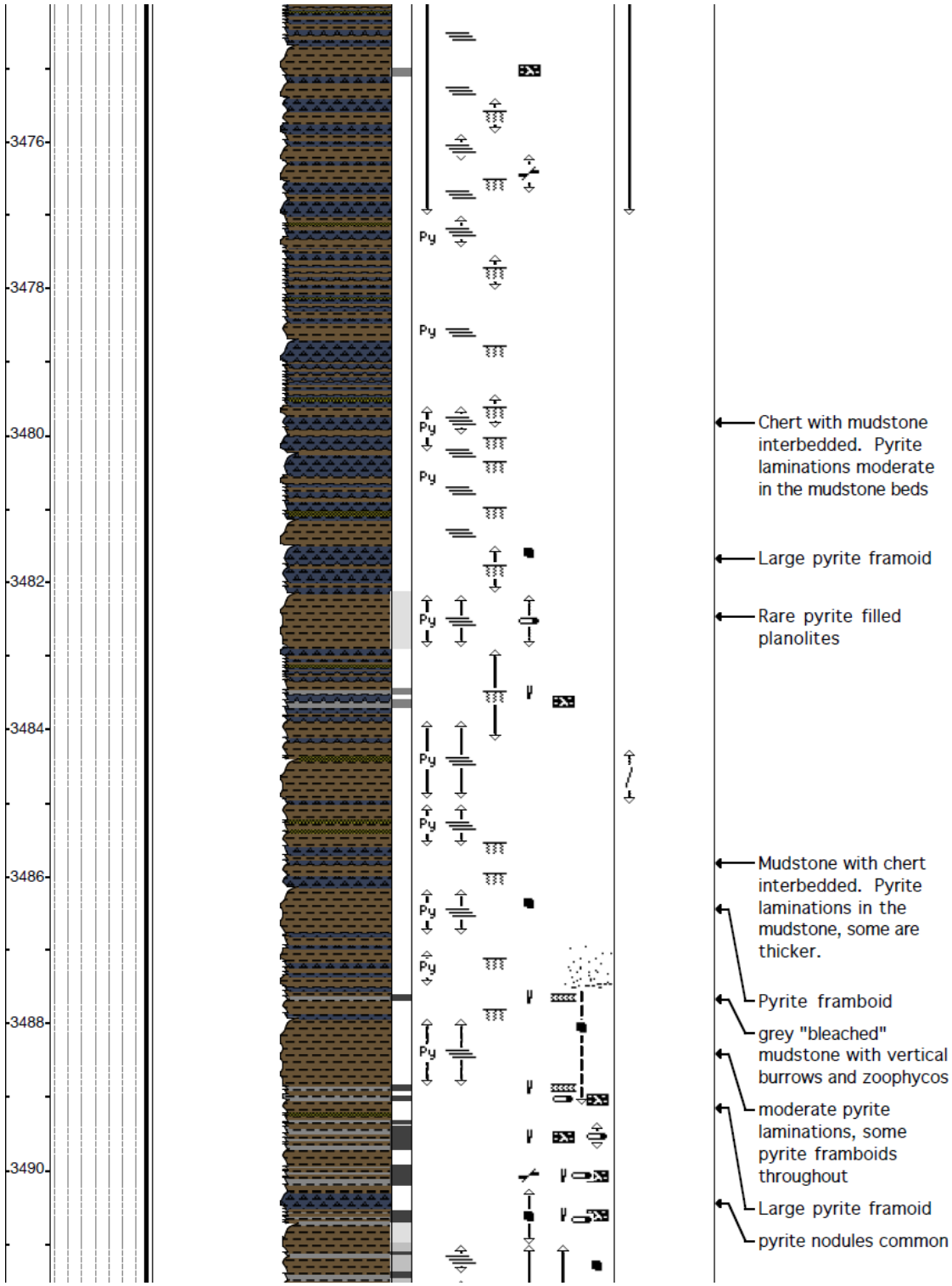
3476
3478
3480
3482
3484
3486
3488
3490
Py
Chert with mudstone interbedded. Pyrite laminations moderate in the mudstone beds
Large pyrite framoid
Rare pyrite filled planolites
Mudstone with chert interbedded. Pyrite laminations in the mudstone, some are thicker.
Pyrite framboid
grey "bleached" mudstone with vertical burrows and zoophycos
moderate pyrite laminations, some pyrite framboids throughout
Large pyrite framoid
pyrite nodules common

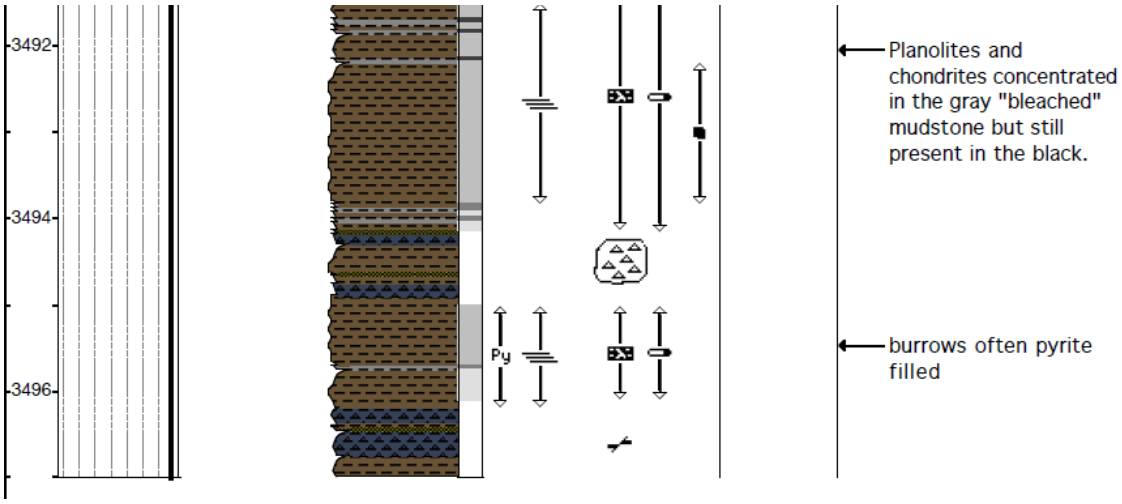
3492
3494
3496
Py
Planolites and chondrites concentrated in the gray "bleached" mudstone but still present in the black.
burrows often pyrite filled
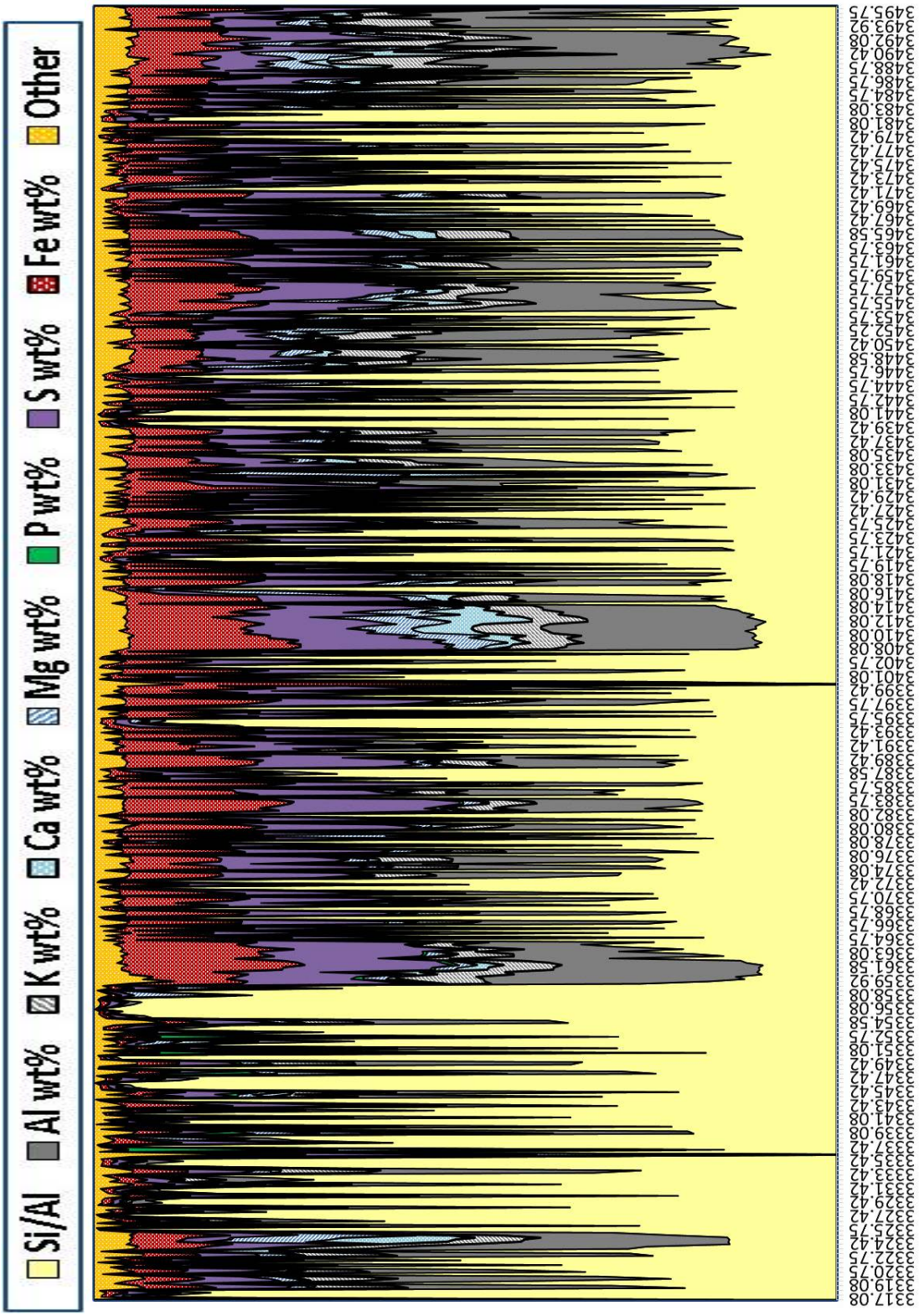
APPENDIX G: CORE E XRF CHART